Simulation of fracture slip and propagation in hydraulic stimulation of geothermal reservoirs

Hau Trung Dang

Thesis for the degree of Philosophiae Doctor (PhD)
University of Bergen, Norway
2023

UNIVERSITY OF BERGEN

Simulation of fracture slip and propagation in hydraulic stimulation of geothermal reservoirs

Hau Trung Dang

Thesis for the degree of Philosophiae Doctor (PhD)
at the University of Bergen

Date of defense: 01.09.2023

Year: 2023

Title: Simulation of fracture slip and propagation in hydraulic stimulation of geothermal reservoirs

Name: Hau Trung Dang

Print: Skipnes Kommunikasjon / University of Bergen

Preface

This thesis is submitted as a partial fulfilment of the requirements for the degree of Philosophiae Doctor (Ph.D.) at the University of Bergen. The advisory committee consists of Inga Berre (University of Bergen) and Eirik Keilegavlen (University of Bergen).

The Ph.D. project has mainly been financed by the University of Bergen as part of its own funding for the ERiS project, which was financially supported by the Research Council of Norway grant number 267908. In addition, this project has received funding from the European Research Council (ERC) under the European Union's Horizon 2020 research and innovation program (grant agreement No 101002507).

Acknowledgments

I am deeply grateful to all those who have supported me throughout my Ph.D. journey at the University of Bergen.

First and foremost, I would like to thank my supervisors, Inga Berre and Eirik Keilegavlen, for their support throughout my academic journey. They have always guided me conducting effective research. They also have always stood by me in overcoming research challenges and aided me in achieving my goals.

I am also grateful to the members of the porous media group at the University of Bergen for their friendship, camaraderie, and support throughout my research projects.

I would like to thank the financial support from the Research Council of Norway, the ERiS project – grant number 267908 and the MaPSI project – grant number 101002507.

Finally, I would like to thank my family, who have trusted and supported me during my time as a Ph.D. candidate.

Hau Trung Dang

Norway, April 2023

Abstract

The role of hydraulic stimulation in enhancing geothermal reservoir production and allowing for commercial exploitation of a larger range of geothermal resources has attracted attention from researchers in recent decades. During stimulation, preexisting fractures may slip, propagate, and connect to other fractures to enhance permeability. The processes are characterized by strong hydromechanical interactions, which have limited monitoring opportunities. Therefore, numerical simulations provide a powerful tool to help us better understand the mechanisms.

This thesis aims to develop a comprehensive mathematical model and a numerical approach to analyze fracture mechanisms, and to investigate the coupled hydromechanical processes occurring in fractured porous media. The proposed model will employ a mixed-dimensional conceptual model, incorporating the concepts of poroelasticity and fracture contact mechanics. The model will also allow for the growth and coalescence of preexisting fractures.

A novel discretization scheme for solving the proposed mathematical model is presented. The proposed scheme employs a two-level simulation approach, categorized into coarse and fine levels, to reduce the computational costs and ensure accuracy. A finite volume method is combined with an active set strategy to discretize poroelasticity and fracture contact mechanics on the coarse level. Fracture propagation is considered on a fine level, in which a finite element method is combined with collapsed quarter-point elements to capture the stress singularity at the fracture tips. Adaptive remeshing based on an error estimator and Laplacian smoothing is introduced on both levels to effectively capture fracture propagation and coalescence in the computational grid. The simulations conducted in this thesis improve our understanding of hydraulic stimulation and its effect on enhancing fracture permeability and connectivity in geothermal reservoirs.

Abstrakt

Rollen til hydraulisk stimulering i å øke produksjonen fra geotermiske reservoarer, og muliggjøre kommersiell utnyttelse av et større spekter av geotermiske ressurser, har fått økt oppmerksomhet de siste tiårene. Under stimulering kan eksisterende sprekker sideforskyves, forplante seg og koble seg til andre sprekker og der igjennom øke permeabiliteten i reservoaret. Prosessene er preget av sterke hydromekaniske interaksjoner, som vi har begrensede muligheter til å overvåke. Numeriske simuleringer er derfor et viktig verktøy for å hjelpe oss til å bedre forstå mekanismene som er i spill.

Avhandlingen tar sikte på å utvikle en omfattende matematisk modell og en numerisk tilnærming for å analysere bruddmekanismer og undersøke koblede hydromekaniske prosesser som forekommer i oppsprukne porøse medier. Den foreslåtte modellen benytter en blandet-dimensjonal konseptuell modell, som inkluderer porelastisitet i det porøse mediet og kontaktmekanikk for sprekkene. Modellen tillater også forplantning og koalescens av eksisterende sprekker.

Et nytt diskretiseringsskjema for å løse den foreslåtte matematiske modellen presenteres. Den foreslåtte metoden bruker en to-nivå simuleringstilnærming, kategorisert i grove og fine nivåer, for å redusere beregningskostnader og sikre nøyaktighet. En endelig volummetode kombineres med en aktiv-sett løsningsstrategi for å diskretisere porelastisitet og bruddkontaktmekanikk på det grove nivået. Sprekkeforplantning betraktes på et fint nivå, der en endelig elementmetode kombineres med kollapsede kvartpunktselementer for å approksimere singulariteten i spenningen ved enden av sprekkene. Adaptiv gitring basert på en feilestimator og Laplace-glatting av gitteret introduseres på begge nivåer for effektivt å håndtere sprekkepropagering og koalescens. Simuleringene utført i denne avhandlingen forbedrer vår forståelse av hydraulisk stimulering og dens effekt på forbedring av sprekkepermeabilitet og konnektivitet i geotermiske reservoarer.

List of Publications

A **Numerical investigation of wing crack initiation and propagation due to shear slip**

Hau Trung Dang, Eirik Keilegavlen, Inga Berre

In Proceedings of European Geothermal Congress, 11-14 June 2019, Den Haag, The Netherlands.

B **Numerical modeling of wing crack propagation accounting for fracture contact mechanics**

Hau Trung Dang, Eirik Keilegavlen, Inga Berre

International Journal of Solids and Structures. Vol. 204–205: 233-247. 2020

DOI: 10.1016/j.ijsolstr.2020.08.017

C **Two-level simulation of injection-induced fracture shear deformation and wing-crack propagation in poroelastic media**

Hau Trung Dang, Eirik Keilegavlen, Inga Berre

International Journal of Rock Mechanics and Mining Sciences. Vol. 160, 105248. 2022

DOI: 10.1016/j.ijrmms.2022.105248

D **Modeling of mixed-mechanism stimulation for the enhancement of geothermal reservoirs**

Hau Trung Dang, Eirik Keilegavlen, Inga Berre

Submitted manuscript. 2023

Contents

Preface i
Acknowledgments iii
Abstract v
Abstrakt vii
List of Publications ix
Part I: Background 1
Chapter 1: Introduction 3
1.1. Main contribution 9
1.2. Outline 10
Chapter 2: Conceptual model 11
2.1 Fractured porous media model 11
2.2 Mixed-dimensional DFM model 13
Chapter 3: Mathematical model 15
3.1 Linear elasticity 16
3.2 Fracture propagation criteria 17
3.3 Fracture contact mechanics 20
3.4 Deformation and fluid flow in fractured porous media 22
3.4.1 Matrix deformation and flow 22
3.4.2 Fluid flow in the fracture 23
3.4.3 Contact mechanics in a fractured porous medium 26
Chapter 4: Numerical methods 27
4.1 Time discretization 28
4.2 Spatial grids 29
4.3 Numerical approach 29
4.3.1 Finite volume methods 31
4.3.2 Finite element methods 33
4.3.3 Discretization for fracture contact mechanics 33
4.3.4 Fracture propagation, coalescence and grid update 34

Chapter 5: Summary and outlook 37
5.1 Summary of papers 37
Paper A 37
Paper B 37
Paper C 38
Paper D 39
5.2 Summary and outlook 40
Bibliography 43
Part II: Scientific results 53

Part I: Background

Chapter 1: Introduction

Globally, geothermal reservoirs provide a significant renewable energy resource (Secretariat-REN21, 2021). Several of the reservoirs that could be exploited are characterized by low permeability, the existence of fractures, and high temperatures. Fluid injection at elevated pressure can reduce the friction between the fracture surfaces, causing fracture slip and dilation, and triggering fractures to propagate, contributing to establishing additional fracture network connections. Both shear dilation of the preexisting fractures and hydraulic fracture propagation can contribute to providing sufficient reservoir permeability for commercial exploitation (Abe & Horne, 2023; McClure & Horne, 2014; Schoenball et al., 2020). However, our understanding of the mechanisms of fracture and fluid-fracture interactions at depth is limited. This thesis focuses on the development of a mathematical model and numerical approach to investigate the hydromechanical processes.

A mathematical model for fractured porous media must be based on simplifying the fracture geometry assumptions and representations of the porous structure. In reality, fractures typically have large aspect ratios, with lengths that can reach hundreds of meters, while the apertures are typically only up to a few millimeters in size (Berkowitz, 2002; Singhal & Gupta, 2010). As a result, it is necessary to use a highly resolved grid if details of the fracture geometry are to be explicitly represented within a computational domain. One approach to addressing this issue is to reduce the dimensionality of the fractures by representing them as lower-dimensional entities, such as lines or curves in a two-dimensional domain or surfaces in a three-dimensional domain. Thus, fractures are still explicitly represented in the computational domain but with a simplified geometrical description. The explicit modeling of fractures allows the displacement field over the fractures to be discontinuous, i.e., the fracture surfaces can move apart or slide. This model can further account for the contact and friction between the fracture surfaces, in which the surfaces are assumed to be nonpenetrating and allowed to shear slip (Kikuchi & Oden, 1988; Wriggers, 2006). The effect of the flows between the fracture and the surrounding porous medium can also be included in this conceptual model (de Borst, 2017). In addition,

this model is convenient to extend to consider the coalescence of fractures during fracture propagation, which affects the fracture network and behavior of the fluid (Weng, 2015).

Furthermore, a simplified representation of the porous medium is necessary due to the complexity of the pore structure. A porous medium contains numerous small pores that allow fluids to flow. In the geothermal reservoir, these pores can range in size from micrometers to centimeters, while the reservoirs size can be several kilometers (Kashif et al., 2019). Given the scale of these systems, explicitly describing each pore in a geothermal reservoir is not feasible. However, the effect of the pore structure and fine-scale fractures can be captured by simplified models, such as a continuum model (Biot, 1941; Pimienta et al., 2017).

Moreover, a simplified model is applicable for analyzing flow characteristics in a low permeability medium. The permeability indicates how easily a fluid can pass through a medium (Gueguen & Palciauskas, 1994). Consequently, in a low permeability medium such as geothermal reservoirs, fluid flows typically occur at a low velocity and are stable (Berre et al., 2019; Eggertsson et al., 2020). As a result, nonlinear flow regimes need not be considered.

To fully understand the interaction between fracture mechanisms and fluid flows in a porous medium, a unified model is needed. In this context, a unified model implies a combination of the equations governing the deformation of the porous medium with the equations governing the fluid flow through the pore structure and fractures. When fractures exist, they can provide pathways for fluids to flow through the medium, significantly impacting the fluid flow behavior. In fact, the presence of fractures can enhance the permeability of the medium, allowing for the fluid to flow more easily through the medium. Additionally, elevated fluid pressure can have significant impacts on fractures. When the pressure of the fluid within the fractures increases, it can cause the fracture surfaces to slide when in contact with each other. The slip can result in an accumulation of stress at the fracture tips, potentially triggering the fracture to propagate. Moreover, when the pressure

of the fluid exceeds the compressive strength of the rock surrounding the fracture, the fracture surfaces can move apart, and the fracture propagates further.

Based on the above discussions, this thesis aims to establish a hydromechanical coupled mathematical model based on several key assumptions. First, we model the domain surrounding the fractures as poroelastic and thereby take into account the interaction between the fluid flows and the solid deformations within a porous medium. Second, we model fractures as lower-dimensional objects compared to the medium, and we consider the fluid flow in the fracture. Finally, we consider fracture contact mechanics. Therefore, the resulting mathematical model consists of a system of differential equations for poroelasticity and fluid flow in fractures, along with inequalities for the fracture contact mechanics and friction. In addition, the proposed model includes the criterion to model fracture propagation.

Combining differential equations with inequalities and the fracture propagation criterion makes the model complex, and we are faced with several challenges in finding its solution. One such challenge is the complexity of the geometry when many fractures present. In addition, the extension of the fracture geometry as they propagate, is an unknown variable. Additionally, the relationship between the aperture and fluid flow in a fracture constitutes a nonlinear relationship in the mathematical model. A crucial outcome of this nonlinear relationship is that the transmissivity of a fracture, which assesses its ability to transmit fluid, is highly sensitive to aperture changes. Even slight modifications in the aperture can result in substantial variations in transmissivity, with potential consequences for the fluid flow dynamics. Moreover, all the variables in the model should be solved simultaneously to avoid a decoupling error. Pressure and displacement are tightly coupled in porous media, where the fluid flow affects the deformation of the solid matrix and vice versa. If these variables are solved independently, it is possible to obtain results that do not accurately reflect the actual behavior of the system, resulting in a decoupling error. In addition, the interdependence of pressure and displacement means that changes in one variable can

significantly impact the other, making it essential to solve them simultaneously to capture the full dynamics of the system.

Using numerical methods to find solutions for the proposed model leads to other challenges. First, the presence of fractures causes difficulty in controlling the quality of the computational grid, which affects the accuracy of the numerical solution. In numerical methods, the accuracy of the solution can be significantly affected by the presence of skew cells in the grid, which come from the small intersecting angles between the fractures (Zienkiewicz & Taylor, 2013). The skewed cells can cause distortions, resulting in inaccurate stress and strain calculations. These cells can also affect the convergence rate of the solution, leading to a slower convergence or even divergence. In addition, these cells can cause numerical instability and lead to numerical errors, such as oscillations and spurious modes. Second, fractures can propagate, causing geometric changes to the fracture domain during a simulation, requiring suitable adaptive meshing techniques. This technique must ensure that the fracture can develop in any direction, and adjusts the grid when the geometry changes. Third, the choice of numerical method plays an important role in accurately simulating the proposed model. Two of the most varied properties are permeability and porosity, which allow fluids to flow easily through the fractures but are at low levels in the surrounding medium. In addition, the fracture propagation mechanism is completely different from that of fluid flow, and different numerical methods have advantageous properties in simulating the various phenomena. For example, the finite element method (FEM), whose computation is node-based, is a computational method proposed and preferred in solid mechanics (Zienkiewicz et al., 2005). FEM is effectively performed on arbitrary grids and allows for easy application of boundary conditions due to a computation based on node interpolation. In addition, the system of algebraic equations resulting from discretization is symmetric and sparse, making it possible to solve it efficiently. Meanwhile, the finite volume method (FVM) has an advantage in the simulation of fluid mechanics (Kolditz, 2002; Moukalled et al., 2015). Similar to FEM, FVM results in a system of algebraic equations with similar properties. In addition, the FVM enforces the conservation of mass and momentum at discretized scales. As a result, fluxes between

adjacent control volumes are directly balanced, making the FVM efficient for solving fluid mechanics problems.

This thesis proposes a coupled mathematical model to simulate the interaction between flows and fractures in porous media. Furthermore, we will use a numerical approach to find the solution. However, many challenges arise in establishing a mathematical model and numerical approach. Therefore, this thesis tackles a portion of these challenges by considering the following main issues.

The first issue is to develop a model to simulate fracture propagation in porous media under the influence of fluid flow. Most previously proposed models consider tensile fracturing and ignore the effects of shear slip, contact, and friction (Lecampion et al., 2017), or they allow fractures to propagate only along predefined paths (McClure & Horne, 2014; Weng et al., 2011). Unlike these previous models, the proposed model in this study combines mixed-mode fractures with fracture contact mechanics. Mixed-mode fractures are references to the combination of different modes of fracture propagation, such as Mode I (opening mode) and Mode II (sliding mode). On the other hand, fracture contact mechanics considers the effects of contact and friction between the fracture surfaces. Thus, the current model has the ability to simulate the shear slip and propagation of the fractures induced by fluid flow.

The second issue is choosing the right numerical approach to perform the simulation. Compared to the fluid flow time scale, fracture propagation can be considered quasistatic, and can therefore be loosely coupled to the fluid flow problem (Adachi et al., 2007; Kim & Duarte, 2015). In addition, there will be no fracture propagation for significant periods, and efficiency can be gained by considering the coupled deformation and fluid flow without fracture propagation. In addition, while it is critical for the propagation problem to accurately capture the stress in the vicinity of the propagating fracture, including the singularity at the tip, the mechanical response of the more expansive reservoir can be given a coarser representation. This thesis proposes a novel approach that splits the coupled mathematical model into submodels that are solved by different numerical approaches.

Specifically, we consider deformations due to fluid pressure in the fractured porous media (poroelasticity) and fracture contact mechanics as a coarse-level model. Mechanical fracture propagation is evaluated in a local fine-level model. The FVM and FEM advantages in fluid and solid mechanic simulations allow us to discretize the coarse-level model by FVM and the fine-level model by FEM. The split model aims to achieve the best simulation efficiency, i.e., reduce the computational cost and ensure a sufficiently low error in the numerical results.

The third issue is the meshing of the fractured domain and fracture propagation. An adaptive meshing technique is considered to address the complexity caused by fracture propagation (Paluszny & Zimmerman, 2011; Salimzadeh et al., 2017). This technique is based on triangular elements/cells, where finer cells are generated at sensitive areas where the estimation error is significantly larger than that for the remaining area. In addition, regions around the fracture tips are remeshed to improve the accuracy in the computation of the fracture propagation along the cell faces. Then, the face-splitting technique is used to update the newly developed fracture in the computational grid.

The final issue arising from the numerical simulation is the complexity of implementation. Using numerical methods to solve nonlinear coupled models often requires numerous iterations to find the solutions, making programming challenging. To address this issue, this study proposes a new implementation that combines newly developed code with an open-source tool named PorePy (Keilegavlen et al., 2021). The new code focuses on fracture propagations, accounting for the fracture contact mechanics, and is associated with an adaptive remeshing technique. Porepy, on the other hand, can simulate poroelasticity with fracture contact mechanics (Berge et al., 2020; Berre et al., 2020; Stefansson, Berre, et al., 2021; Stefansson, Keilegavlen, et al., 2021). The proposed implementation aims to provide an efficient and reliable tool for simulating the coupled hydromechanical processes occurring in fractured porous media.

1.1. Main contribution

The main contributions of this thesis are as follows:

- **A numerical modeling of wing crack propagation accounting for fracture contact mechanics**. First, Papers A and B present a mathematical model and corresponding numerical solution approach to model fracture mechanics under shear processes. The proposed mathematical model has the ability to model wing crack propagation and the coalescence of preexisting fractures while accounting for fracture contact mechanics. The numerical solution approach is based on combining the finite element method with quarter-point elements to handle the singularity at the fracture tips. The fracture contact mechanics are modeled by using the active set strategy. Due to the significant difference in scale between the simulation domain and the fracturing processes, adaptive remeshing, based on an error estimator and Laplacian smoothing for implementation, is utilized for computational efficiency.
- **Modeling of injection-induced fracture slip and wing-crack propagation in poroelastic media for enhanced geothermal reservoirs**. Papers C and D present a mathematical model and a numerical solution strategy for coupling fluid flow, matrix deformation, fracture slip and fracture propagation and coalescence in porous media due to fluid injections. The governing mathematical model is based on Biot's model, with the deformation of the existing fractures represented by contact mechanics. The maximum tangential stress criterion is combined with Paris' law to govern the fracture growth processes. A two-level simulation is presented to reduce the computational costs and ensure accuracy. The numerical approach employs a novel combination of finite volume methods for the poroelastic deformation of the existing fractures with a finite element approach, as developed in Papers A and B, for the fracture propagation process. The effects of the injection rate, matrix permeability, and stress anisotropy on the stimulation outcome are studied to enhance our understanding of the hydromechanical processes in geothermal reservoirs.

1.2. Outline

This thesis is divided into two parts. Part I is an introduction to the mathematical model and numerical methods. Part II presents the main scientific contribution with four papers either published or submitted to scientific journals.

The remainder of Part I is organized as follows:

Chapter 2 gives a brief overview of the different conceptual models for fractured porous media, where the main focus is on the mixed-dimensional discrete fracture matrix model.

Chapter 3 presents a mathematical model for fracture propagation in a linearly elastic medium. This model is then extended to a fractured porous medium, in which deformation, fluid flow, and fracture propagation are considered.

Chapter 4 presents the discretizations of the mathematical models given in Chapter 3.

Chapter 5 summarizes the papers in Part II and their scientific contributions. The limitations of the current study and its prospects are also discussed in this section.

Chapter 2: Conceptual model

Conceptual models are the essential assumptions that guide the development of a suitable and efficient mathematical model for simulation. These assumptions are intended to define the application scope of the proposed model, providing a framework for accurately simulating the phenomenon of interest. Therefore, this chapter focuses on the conceptual models used for fractured porous media. After an introduction to different models in Section 2.1, the chapter provides more details on the mixed-dimensional discrete fracture-matrix model used throughout this thesis in Section 2.2.

While the purpose of this thesis is not to develop new conceptual models, this chapter serves as a brief introduction to prepare the reader for the mathematical modeling concepts discussed in Chapter 3, and the discretization techniques covered in Chapter 4. Both of these subsequent chapters rely on the choice of a conceptual model, and understanding the underlying assumptions and principles is crucial for the reader's comprehension.

2.1 Fractured porous media model

Fractured porous media are complex structures commonly found in geothermal reservoirs (Jung, 2013; McClure & Horne, 2011, 2014; Norbeck et al., 2018; Pine & Batchelor, 1984; Schoenball et al., 2020) and have attracted the interest of scientists in developing efficient mathematical models (Viswanathan et al., 2022). These structures are characterized by numerous pores and fractures that allow fluids to flow through them. Both the pores and fractures form in different sizes. While pores are significantly smaller than the domain of interest for the current modeling study, fractures exist in various sizes, from a few millimeters to several kilometers. Furthermore, the fracture surfaces are rough, with a nonuniform aperture, where the apertures are significantly smaller than the fracture length. In addition, the network of fractures in porous media is also highly complex because the fractures occur randomly and intersect.

For the pore structure, the arbitrary distribution of a large number of pores at a microscale can be represented by a continuum model based on the concept of a representative

elementary volume (REV) (Bear, 2013). In this approach, the porous medium is simplified by a continuum and does not consider the intricacies and fine details of the microscopic pore structure. Instead, upscaled parameters such as porosity and permeability, are used to describe this structure in the geometry domain at the macroscopic scale.

The single-continuum model is often used to represent porous media (Bear, 1993), however, it has limitations when fractures exist. This model is the simplest and most accessible because it assumes that the porous media is homogeneous, and it does not consider the presence of larger fractures or other types of heterogeneities. As such, this model is suitable for microfracture networks where the flow rates in the pores and fractures are not much different but it is not appropriate for larger fractures. Larger fractures can significantly alter the flow behavior by providing preferential pathways for fluid flows, increasing the effective permeability of the porous media, and causing fluid channeling. Because of this, it is not, in general, possible to define an REV and to use the single-continuum model to characterize the hydromechanics in both the fractures and pores.

The discrete fracture network (DFN) model is a relevant approach for a complex fracture network (Sahimi, 2012). This model explicitly presents the entire fracture network and ignores the details of the physical processes in the rock matrix, i.e., the domain surrounding the fractures is assumed to be impermeable. The fracture surfaces are approximated as planar and parallel, and the aperture parameter represents the average distance between them. This model allows a fracture to be mechanically closed, i.e., there is contact across the fine-scale rough fracture surfaces, even if the aperture is not zero. Even though this model captures the characteristics of the fracture network, neglecting the permeability in the rock leads to unsuitability when using this model to consider the flows in fractured porous media. The computational cost also presents challenges when dealing with a complex fracture network that involves many fractures of significantly different sizes.

The discrete fracture-matrix (DFM) model is proposed to address the limitations of the DFN model (Dietrich et al., 2005; Neuman, 2005). The DFM model combines the explicit representation of major fractures with the continuum approach for the surrounding medium.

Specifically, while the pore structure is represented entirely by a continuum domain, the fracture network is represented by two different models. Small-scale fractures are integrated as part of the continuum domain and represented through an upscaled effective permeability. Meanwhile, the large-scale dominant fractures are represented explicitly in the same manner as the DFN model (Frih et al., 2012; Nordbotten et al., 2019; Reichenberger et al., 2006). Thus the choice between the computational cost and accuracy in approximating the actual problem is flexibly set in this model.

2.2 Mixed-dimensional DFM model

Although the DFM model has many advantages in terms of computational cost and accuracy, it is still challenging to present the fracture aperture in the computational grid because of the high fracture aspect ratio, leading to the proposal of the mixed-dimensional DFM model. Indeed, a significant difference between the length and aperture of the fracture requires a spatial discretization of the domain with a high number of small and/or skewed cells that significantly affect the numerical solution. To address this challenge, a co-dimension-one object with a parameter for the aperture can be considered to represent the fracture (Martin et al., 2005; Reichenberger et al., 2006). Specifically, the fracture is still represented by two parallel faces in the computational grid but they overlap. Thus, this approach does not directly represent the fracture aperture on the grid. Instead, a fracture aperture parameter is associated with the computational grid of the fracture. With this approach, the fracture aperture does not affect the grid resolution.

Another dilemma when modeling fracture networks is the coalescence of the fractures. In this work, by representing fractures as co-dimension-one objects, we use a point to represent an intersection of the fractures. For preexisting fractures, the fractures can be considered intersecting in the V-, X-, and T-types. However, in this thesis, new intersections resulting from fracture propagation are only considered in the T-type due to the limitations of the current model, as shown in Papers B and D.

The next chapter focuses on developing a mathematical model for coupled hydromechanical problems based on the mixed-dimensional DFM conceptual model. The

porous medium, fractures, and intersection between fractures are defined as subdomains that are two-dimensional (2D), one-dimensional (1D), and zero-dimensional (0D), respectively. The 2D domain representing the porous medium is assumed to be geometrically continuous, however, solutions may be discontinuous across the fractures. This domain also considers the influence of pores and fractures at the microscopic level by continuum-scale parameters representing porosity and permeability (Koponen et al., 1997). Meanwhile, larger fractures are explicitly represented. In the 1D domain, the aperture parameter represents the fracture thickness. In addition, the roughness and friction between the fracture surfaces are simplified by the parameters and variables describing the fracture contact mechanics.

Chapter 3: Mathematical model

This chapter presents mathematical models based on the chosen conceptual model, i.e., the mixed-dimensional DFM model. First, we present a mathematical model for fracture contact mechanics and propagation in a solid domain. Then, the model is extended to fractured porous media. For the convenience of establishing the mathematical model, Table 1 lists the symbols used in this work, and the conceptual representation of each subdomain and interface is presented in Figure 3.1. The matrix is denoted by Ω^{M}, the fracture is denoted by Ω^{F}, and the intersection of the fractures is denoted by Ω^{I}. The interface between Ω^{M} and Ω^{F} is denoted by Γ, and that between Ω^{F} and Ω^{I} is denoted by Λ. The boundary of Ω^{M} that coincides with the interface Γ is denoted by $\partial\Omega^{\mathrm{M}}$.

Table 1. Definition of Symbols

Symbol	Description
Ω^{M}	matrix domain
Ω^{F}	fracture domain
Ω^{I}	intersection of fractures
Γ	interface between Ω^{M} and Ω^{F}
Λ	interface between Ω^{F} and Ω^{I}
$\partial\Omega$	boundary of Ω domain
Π	projection operators
$\boldsymbol{\sigma}$	stress tensor
$\boldsymbol{\varepsilon}$	symmetric infinitesimal strain tensor
$\mathbf{C}$	elasticity (Hooke's) tensor
$\mathbf{u}$	displacement
$[\![\mathbf{u}]\!]$	displacement jump
$\mathbf{f}$	traction
K_I, K_{II}	stress intensity factors
μ_s	friction coefficient
g	gap of fracture

a	aperture of fracture
a_0	residual aperture in the undeformed state
p	matrix pressure
ϕ	matrix porosity
c_p	fluid compressibility
μ	fluid viscosity
$\mathbf{q}$	matrix flux
ζ	inflow from the matrix to the fracture
$\mathcal{K}$	matrix permeability
κ	fracture permeability
$\mathcal{K}_F$	fracture transmissivity
p_F	fracture pressure
$\mathbf{q}_F$	fracture flux
λ	flux at the interface of matrix and fracture
η	flow from fracture to intersection of fractures
(r, θ)	polar coordinates
Oxy	cartesian system of coordinates

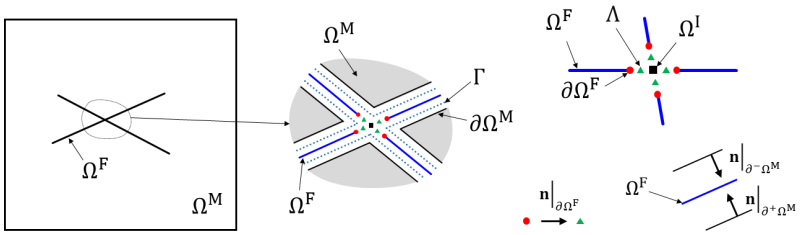

Figure 3.1. Conceptual representation of the subdomains and the interface

3.1 Linear elasticity

In the mixed-dimensional DFM model, the porous media is represented by a continuum, in which the theory of elasticity is assumed to govern the mechanical behavior. Under the effect of an external force and ignoring gravity, a stress field appears inside to balance and

keep the body in equilibrium. The relationship between them is represented by the conservation of momentum as given by

$$\nabla \cdot \boldsymbol{\sigma} + \mathbf{b} = 0 \quad \text{on} \quad \Omega^{\mathrm{M}}, \tag{1}$$

where ∇ is a gradient operator, $\boldsymbol{\sigma}$ is the stress, and $\mathbf{b}$ is the external force. By linear elastic theory, the stress is defined by

$$\boldsymbol{\sigma} = \mathbf{C} : \boldsymbol{\varepsilon} \quad \text{on} \quad \Omega^{\mathrm{M}}, \tag{2}$$

where $\mathbf{C}$ is the elasticity (Hooke's) tensor defined by Young's modulus and Poisson's ratio. The symmetric infinitesimal strain tensor, $\boldsymbol{\varepsilon}$, is defined from displacement $\mathbf{u}$, such that

$$\boldsymbol{\varepsilon} = \frac{1}{2}(\nabla \mathbf{u} + \nabla \mathbf{u}^{\mathrm{T}}) \quad \text{on} \quad \Omega^{\mathrm{M}}. \tag{3}$$

Eqs. (2) and (3) are obtained based on some assumptions. The first assumption is that the stress and strain are proportional to each other within the elastic limit, meaning that the material will return to its original shape when the applied forces are removed. The second assumption is that the deformation is sufficiently small, so the changes in each direction are negligible compared to the original shape. Therefore, the strains, which represent the changes in the shape of the material, are assumed to be small. Both assumptions are acceptable because porous rock is a sturdy structure with low elasticity. This mathematical model was used in Papers A and B.

3.2 Fracture propagation criteria

When a fracture exists, assuming the fracture is parallel to the *Ox* axis in the Cartesian system of coordinates, *Oxy*, the stresses around a fracture tip can be expressed in terms of scaling factors called the stress intensity factors (SIFs) for any subjected loading. These factors are defined by (Irwin, 1957)

$$K_I = \lim_{r \to 0} \sqrt{2\pi r}\, \sigma_{xx}(r, \theta = 0), \tag{4}$$

$$K_{II} = \lim_{r \to 0} \sqrt{2\pi r}\, \sigma_{xy}(r, \theta = 0), \tag{5}$$

where σ_{xx} and σ_{xy} are the normal and tangential stresses defined from the model presented in Section 3.1. The polar coordinates with the origin at the fracture tip are denoted by (r, θ). K_I is the SIF for Mode I, applied to the opening (tensile) mode where the fracture surfaces move directly apart. K_{II} is the SIF for Mode II (in-plane shear), where the fracture surfaces slide over one another in a direction perpendicular to the leading face of the fracture. Then, the stress field around the fracture tip is determined by (Erdogan & Sih, 1963; Williams & Ewing, 1984)

$$\sigma_{rr} = \frac{1}{\sqrt{2\pi r}}\left[\frac{K_I}{4}\left(5\cos\frac{\theta}{2} - \cos\frac{3\theta}{2}\right) + \frac{K_{II}}{4}\left(-5\sin\frac{\theta}{2} + 3\sin\frac{3\theta}{2}\right)\right], \tag{6}$$

$$\sigma_{\theta\theta} = \frac{1}{\sqrt{2\pi r}}\left[\frac{K_I}{4}\left(3\cos\frac{\theta}{2} + \cos\frac{3\theta}{2}\right) + \frac{K_{II}}{4}\left(-3\sin\frac{\theta}{2} - 3\sin\frac{3\theta}{2}\right)\right], \tag{7}$$

$$\sigma_{r\theta} = \frac{1}{\sqrt{2\pi r}}\left[\frac{K_I}{4}\left(\sin\frac{\theta}{2} + \sin\frac{3\theta}{2}\right) + \frac{K_{II}}{4}\left(\cos\frac{\theta}{2} + 3\cos\frac{3\theta}{2}\right)\right]. \tag{8}$$

By Eqs. (6)-(8), we can see that stresses at the tip of a fracture are infinite and independent of the applied load. According to this model, the failure of the structure always appears, even in a minor fracture and at an insignificant applied load. However, this stress field is still obtained from linear elastic theory, which is no longer suitable for the nonlinear behavior of materials approaching the fracture tip. Indeed, in the tiny region close to the tip, the concentration of stresses around the fracture tip can cause a localized plastic deformation or irreversible changes in the shape of the material (Anderson, 2017; Tada et al., 2000). Nevertheless, as the distance from the tip increases, the magnitude of the stresses decreases, and the material behavior becomes more elastic. Therefore, for the remaining region, such as the asymptotic region around the fracture tip, this stress field is still valid and can be used to design the fracture propagation criteria presented in the next section (Irwin, 1957; Rice, 1968).

As discussed in the previous chapter, this study utilizes the continuous mechanical fracture approach that considers only macroscale and deterministic fractures. In addition, we assume that a fracture propagates without branching and may connect to other fractures. Therefore, this section focuses on a propagation criteria consistent with these assumptions. There are three suitable criteria. The first is the maximum tangential stress criterion (MTS) (Beuth & Herakovich, 1989; Buczek & Herakovich, 1985; Carloni & Nobile, 2005; Paris & Erdogan, 1963; Saouma et al., 1987). This criterion states that the fracture propagates in the direction where the circumferential stress is maximum. The second criterion is the minimum strain energy density criterion (MSE) (Erdogan & Sih, 1963; Sih, 1974). The fracture grows in a direction in which the strain energy density reaches the minimum value by the MSE. The third criterion is the maximum strain energy release rate criterion based on the Griffith theory (GRT) (Chang et al., 2006). The GRT presents a general mixed-mode brittle fracture criterion based on the maximum potential energy release rate concept.

All of these criteria are consistent with experiments when simulating the unbranched growth of fractures in brittle material (Ingraffea & Heuze, 1980). The criterion with the simplest form, which is the MTS, is used in our work (Papers A, B, C, and D). Based on the MTS, the propagation angle is the solution of the equation $\partial\sigma_{\theta\theta}/\partial\theta = 0$ and subject to $\partial^2\sigma_{\theta\theta}/\partial\theta^2 < 0$. Hence, the propagation angle is defined by

$$\theta_0 = 2\tan^{-1}\left(\frac{K_{\mathrm{I}}}{4K_{\mathrm{II}}} \pm \frac{1}{4}\sqrt{\left(\frac{K_{\mathrm{I}}}{K_{\mathrm{II}}}\right)^2 + 8}\right), \tag{9}$$

$$K_{\mathrm{II}}\left(\sin\frac{\theta_0}{2} + 9\sin\frac{3\theta_0}{2}\right) < K_{\mathrm{I}}\left(\cos\frac{\theta_0}{2} + 3\cos\frac{3\theta_0}{2}\right). \tag{10}$$

Equation (9), subjected to condition (10), always returns a unique solution depending on the SIFs. This means that the fracture propagates in a single direction from each tip at each specific stress state. The propagation length will be discussed in Chapter 4.

3.3 Fracture contact mechanics

The fracture surfaces are typically in contact because the porous media in a geothermal reservoir are under compressive stress, so fracture contact mechanics should be considered in the model. Before establishing the contact model, three assumptions are considered. First, even though the fracture is mechanically closed, it can contain a volume of fluid caused by the small-scale fracture roughness. Therefore, the residual aperture in the undeformed state should be considered, and is denoted by a_0. Then, the fracture aperture, indicated by a, is a function determined based on the residual aperture and normal displacement jump, such as

$$a = a_0 + [\![\mathbf{u}]\!]_{\mathrm{n}} \quad \text{on} \quad \Omega^{\mathrm{F}}, \tag{11}$$

where $[\![\mathbf{u}]\!]_{\mathrm{n}}$ is the normal displacement jump on the fracture interfaces.

Second, a gap, denoted by g, is defined as the normal displacement jump, $[\![\mathbf{u}]\!]_{\mathrm{n}}$, between two fracture interfaces when they are in contact. This value depends on the tangential displacement on the fracture interfaces. Indeed, tangential displacements on the fracture may induce dilation as a result of the roughness of the interfaces when they slide over each other (Hossain et al., 2002). In this case, the fracture is still considered mechanically closed even though the gap between them is nonzero. Therefore, the formulation of the gap is given by (Rahman et al., 2002)

$$g = -\tan(\psi)\|[\![\mathbf{u}]\!]_{\tau}\| \quad \text{on} \quad \Omega^{\mathrm{F}}, \tag{12}$$

where $[\![\mathbf{u}]\!]_{\tau}$ is the tangential displacement jump on the fracture interfaces, and ψ is the dilation angle.

Third, there is contact traction on Ω^{F} projected from the matrix domain. We consider that contact forces, which are defined by the stress (defined in Section 3.1) and the normal vector on the fracture surfaces in Ω^{M}, obey Newton's third law, i.e., they are equal but have

opposite signs when the surfaces are in contact. Then, the value of traction on Ω^{F} is equal to the value of the corresponding forces from Ω^{M}. The traction is defined by

$$\mathbf{f} = \boldsymbol{\sigma} \cdot \mathbf{n} \ \text{ on } \ \Gamma^{+}, \tag{13}$$

where $\mathbf{n}$ denotes the normal vector initiating from Γ^{+} to Γ^{-}, in which $\Gamma^{\pm}$ are the interfaces between Ω^{M} and Ω^{F} at each side of Ω^{F}. In the following, the fracture contact mechanics model is considered independently in the normal and tangential directions. In the normal direction, whenever the normal deformation jump is equal to the gap, the fracture is considered closed but not penetrating, and when it is larger, it is considered open. Whenever the fracture comes into contact, the normal contact traction keeps the forces in equilibrium. In contrast, this traction is zero when a fracture opens. These assumptions are expressed in the form of the Karush Kuhn-Tucker (KKT) conditions (Wohlmuth, 2011) as follows

$$[\![\mathbf{u}]\!]_{\mathrm{n}} - g \geq 0, \quad f_{\mathrm{n}} \leq 0, \quad ([\![\mathbf{u}]\!]_{\mathrm{n}} - g) f_{\mathrm{n}} = 0 \quad \text{on} \quad \Omega^{\mathrm{F}}, \tag{14}$$

where f_{n} is the normal contact traction acting on the fracture.

Next, considering the tangential direction, whenever the fracture interfaces come in contact, they can slide in the opposite direction. This slip is affected by the friction between them. By the Coulomb friction law, the sliding, or deformation in the tangential direction when the fracture is closed, satisfies the following system (Popov, 2010)

$$\begin{array}{ll} |f_{\tau}| \leq -\mu_s f_{\mathrm{n}} & \\ |f_{\tau}| < -\mu_s f_{\mathrm{n}} \rightarrow [\![\dot{\mathbf{u}}]\!]_{\tau} = 0 & \text{on} \quad \Omega^{\mathrm{F}}, \\ |f_{\tau}| = -\mu_s f_{\mathrm{n}} \rightarrow \exists \varepsilon \in \mathbb{R},\ f_{\tau} = -\varepsilon [\![\dot{\mathbf{u}}]\!]_{\tau} & \end{array} \tag{15}$$

where f_{τ} is the tangential contact traction and $\dot{\mathbf{u}}$ is the derivative of $\mathbf{u}$ with respect to time. The tangential traction of the fracture is bounded from above by the normal traction scaled by the friction μ_s, and when the frictional resistance is overcome, the fracture surfaces slip parallel to the tangential traction.

The mathematical model for fracture contact mechanics presented in this subsection was used in Papers B, C, and D.

3.4 Deformation and fluid flow in fractured porous media

This section extends the fracture propagation model accounting for the fracture contact mechanics presented in Sections 3.1–3.3 to porous media, and was used in Papers C and D. Hence, we will consider deformation, fluid flow, and fracture propagation in porous media. The assumptions for the deformation and fracture propagation are as in the above sections, i.e., we utilize the theory of linear elasticity accounting for fracture contact mechanics. We assume that the temperature effects on fluid flow are negligible, and we model the flow as a single phase with a low Reynolds number, i.e., laminar flow. The expansion of the model requires the incorporation of new variables. Specifically, we need to account for the pressure variable in the pores, since the fluid flows through the pore structure. Moreover, we also need to consider the flow behavior in the fracture.

3.4.1 Matrix deformation and flow

In porous media, momentum conservation is similar to that in solids, i.e., governed by Eq. (1). Meanwhile, the stress is the result of not only deformation but also pore pressure, so that (Biot, 1941)

$$\boldsymbol{\sigma} = \mathbf{C}\nabla_s \mathbf{u} - \alpha p \mathbf{I} \quad \text{on} \quad \Omega^{\mathrm{M}}, \tag{16}$$

where $\mathbf{C}$ is the elasticity tensor defined the same as Eq. (2), $\mathbf{I}$ is the second-order identity matrix and p is the pressure in the porous medium. The Biot coefficient of the matrix is $\alpha \in [0,1]$.

By considering the fluid flow, the conservation of mass is governed by

$$\alpha \frac{\partial(\nabla \cdot \mathbf{u})}{\partial t} + M \frac{\partial p}{\partial t} + \nabla \cdot \mathbf{q} = q_0 \quad \text{on} \quad \Omega^{\mathrm{M}}, \tag{17}$$

where t is the time variable. The Biot modulus is given by $M = \left(\phi c_p + \frac{\alpha-\phi}{K}\right)$, c_p is the fluid compressibility, ϕ is the matrix porosity, K denotes the bulk modulus, and q_0 is the source/sink team. The flux, **q**, is defined by Darcy's law such that

$$\mathbf{q} = -\frac{\mathcal{K}}{\mu}\nabla p \quad \text{on} \quad \Omega^{\mathrm{M}}, \tag{18}$$

where μ is the fluid viscosity and $\mathcal{K}$ denotes the matrix permeability. Eqs. (17) and (18) are developed based on the continuous model for porous media, in which the pore structure and permeability of porous media are upscaled by ϕ and $\mathcal{K}$.

3.4.2 Fluid flow in the fracture

The simplest flow model through a fracture is called the parallel plate model, where the fracture is assumed to be bounded by two smooth, parallel surfaces separated by an aperture. Based on this model, the permeability of the fracture can be identified as (Witherspoon et al., 1980; Zimmerman & Bodvarsson, 1996)

$$\kappa = \frac{a^2}{12} \quad \text{on} \quad \Omega^{\mathrm{F}}, \tag{19}$$

where a is the fracture aperture, given by Eq. (11). The product of the permeability and the fracture aperture, which is sometimes known as transmissivity, is equal to

$$\mathcal{K}_F = \kappa a = \frac{a^3}{12} \quad \text{on} \quad \Omega^{\mathrm{F}}. \tag{20}$$

Eq. (20) is called the cubic law. An important consequence of the cubic law is that the fracture transmissivity is extremely sensitive to aperture change.

The dominant pathway for fluid flow through a fracture is along its length due to the difference between the fracture aperture and pore diameters in the surrounding rock matrix. The aperture of a fracture is typically much larger than the pore diameters in the matrix, providing a preferential pathway for fluid flow. As a result, fluid flows more easily through

the fracture than through the surrounding rock matrix. Under this observation, the equation for the conservation of mass in the fracture can be simplified to a one-dimensional equation, defined along the length of the fracture (Martin et al., 2005; Stefansson, Berre, et al., 2021),

$$\frac{\partial a}{\partial t} + ac_p \frac{\partial p_F}{\partial t} + \nabla_{\parallel} \cdot \mathbf{q}_F - \zeta = q_F^0 \quad \text{on} \quad \Omega^{\mathrm{F}}, \tag{21}$$

$$\mathbf{q}_F = -\frac{\mathcal{K}_F}{\mu} \nabla_{\parallel} p_F \quad \text{on} \quad \Omega^{\mathrm{F}}, \tag{22}$$

where the differential operator, $\nabla_{\parallel}$, is defined on the tangent space of Ω^{F}. In Eqs. (21) and (22), μ is the fluid viscosity; $\mathbf{q}_F$, p_F, and q_F^0 are the flux, pressure, and source/sink in the fracture; and the term ζ represents inflow from the matrix to the fracture.

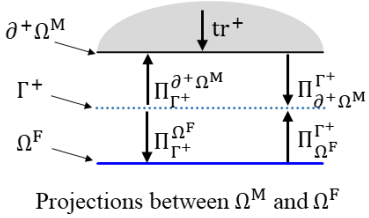

a) Projections between Ω^{M} and Ω^{F}

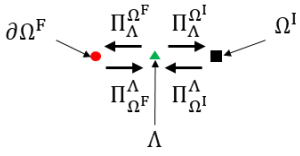

b) Projections between Ω^{F} and Ω^{I}

Figure 3.2. Projection representation for the coupling between subdomains

To facilitate coupling between subdomains, specifically between Ω^{M} and Ω^{F} and between Ω^{F} and Ω^{I}, we introduce projection operators Π, as depicted in Figure 3.2. Details of these operators can be found in the work of Keilegavlen et al. (Keilegavlen et al., 2021). The subscripts of Π denote the origin, while the superscripts indicate the destination of the projection. The trace operator tr maps quantities from Ω^{M} to its boundary $\partial\Omega^{\mathrm{M}}$.

To establish the mapping between Ω^{M} and Ω^{F}, we first determine the flux at the interfaces $\Gamma^{\pm}$, which is generated by pressure in both the fracture and matrix. Then, we enforce the balance of flux at the interfaces. The flux on the $\Gamma^{\pm}$ is defined as

$$\lambda^{\pm} = -\frac{\kappa}{\mu}\left(\frac{\Pi_{\Omega^{\mathrm{F}}}^{\Gamma^{\pm}} p_F - \Pi_{\partial^{\pm}\Omega^{\mathrm{M}}}^{\Gamma^{\pm}} \mathrm{tr}^{\pm}\, p}{a/2}\right) \quad \text{over} \quad \Gamma^{\pm}. \tag{23}$$

The balance of the flux between the matrix and fracture is enforced in the interfaces as follows:

$$\mathbf{q}\cdot\mathbf{n}|_{\partial^{\pm}\Omega^{\mathrm{M}}} = \Pi_{\Gamma^{\pm}}^{\partial^{\pm}\Omega^{\mathrm{M}}} \lambda^{\pm} \quad \text{on} \quad \partial\Omega^{\mathrm{M}}, \tag{24}$$

The inflow from the matrix to the fracture in Eq. (21), ζ, is defined by (Martin et al., 2005)

$$\zeta = \Pi_{\Gamma^{+}}^{\Omega^{\mathrm{F}}} \lambda^{+} + \Pi_{\Gamma^{-}}^{\Omega^{\mathrm{F}}} \lambda^{-} \quad \text{on} \quad \Omega^{\mathrm{F}}. \tag{25}$$

When fractures intersect, the conservation equation in the intersection, Ω^{I}, is defined by

$$\frac{d(a_I^2)}{dt} + a_I^2 c_p \frac{\partial p_I}{\partial t} - \sum_{i=1}^{N} \Pi_{\Lambda^{\mathrm{i}}}^{\Omega^{\mathrm{I}}} \eta_i = q_I^0 \quad \text{on} \quad \Omega^{\mathrm{I}}, \tag{26}$$

where N is the number of intersecting fractures around Ω^{I} and a_I is taken to be the average of the apertures of the intersecting fractures. For T-type and X-type intersections, $N = 3$ and $N = 4$, respectively. q_{I}^0 is the source/sink term in the fracture intersection. η_i is a variable that represents the flow from fracture i to Ω^{I}, defined by

$$\eta_i = -\frac{\mathcal{K}_F}{\mu}\left(\frac{\Pi_{\Omega^{\mathrm{I}}}^{\Lambda^{\mathrm{i}}} p_I - \Pi_{\Omega^{\mathrm{F}}}^{\Lambda^{\mathrm{i}}} p_F}{a_I/2}\right) \quad \text{on} \quad \Lambda_i, \tag{27}$$

Then, a balance between the fracture and fracture intersection is enforced as

$$\mathbf{q}_F\cdot\mathbf{n}|_{\partial\Omega_i^{\mathrm{F}}} = \Pi_{\Lambda^{\mathrm{i}}}^{\Omega^{\mathrm{F}}} \eta_i \quad \text{on} \quad \partial\Omega_i^{\mathrm{F}}, \tag{28}$$

where $\mathbf{n}|_{\partial\Omega_i^{\mathrm{F}}}$ is the normal vector pointing out from $\partial\Omega_i^{\mathrm{F}}$ in the direction of Λ_i.

3.4.3 Contact mechanics in a fractured porous medium

The presence of fluid in a fracture affects the contact force on the fracture surface. Therefore, the contact traction used to establish the fracture contact mechanics in Eq. (13), denoted by **f,** is modified as follows:

$$\mathbf{f}_{\pm} = \pm\left(\Pi^{\Gamma^{\pm}}_{\partial^{\pm}\Omega_M}\boldsymbol{\sigma} + \mathbf{I}\,\alpha_f\,\Pi^{\Gamma^{\pm}}_{\Omega_F} p_F\right) \quad \text{on} \quad \Gamma^{\pm}, \tag{29}$$

where $\boldsymbol{\sigma}$ represents the hydromechanical stress in the matrix as defined in Eq. (16), and α_f represents the Biot coefficient in the fracture. Except for the modified contact traction, the rest of Subsection 3.3 remains unchanged when the flow effect is included in the fracture.

Chapter 4: Numerical methods

This chapter presents a numerical approach to discretize the mathematical models proposed in Chapter 3. Since the mathematical model depends on both the space and time variables, model discretization must be considered for both variables. For the variation with time, the mathematical model only contains the first derivative, so time discretization is directly accomplished by the backward Euler method. In contrast, the model is more complex in terms of the spatial variations of the variables. Therefore, examples of spatial discretization methods are presented below. Based on the meshing, these approaches can be divided into two main categories: meshing independent of the fracture and conforming to the fracture.

The extended finite element method (XFEM) models the fracture independently of the computational grid, and it is specially designed for treating the discontinuities caused by the fracture (Belytschko & Black, 1999). This method uses a grid that is independent of the fractures, and the discontinuity is handled by using enrichment functions locally in elements around fractures. Hence, it is convenient for fracture propagation modeling because it avoids remeshing. To consider coupled fluid flow and fracture propagation, by using a special enriched shape function, the fluid pressure variable is introduced to describe the fluid flow within the fracture and its contribution to the fracture deformation (Lecampion, 2009; Liu et al., 2017; Mohammadnejad & Khoei, 2013). The XFEM is also extended to simulate the fracture contact mechanics by considering a Heaviside function based on the normal jump between the interfaces (Khoei & Nikbakht, 2006).

The conforming grid approach forces fracture growth along the faces of the grid cells. The FEM and FVM methods (Golovin et al., 2015; Hunsweck et al., 2013; Settgast et al., 2017) are widely used methods based on this approach. First, a conforming grid with fractures is generated and refined in the region where fractures may propagate. Then, the fracture extension in the grid is determined by the faces that either best fit the numerical solution or are locally adjusted based on the estimated propagation orientation. Compared with XFEM, this approach is made more expensive by increasing the number of computational cells to capture the fracture geometry, and the accuracy of this approach is highly dependent on the

grid resolution. However, by the explicit representation of the fracture geometry, this approach is more straightforward in modeling the mechanical characteristics of fracture such as the deformation, stress, strain, energy, and friction inside and surrounding the fracture.

The highly dependent grid resolution of the conforming grid approach can be solved by the adaptive remeshing technique (ARM). In the ARM, mesh refinement is performed around the fracture tips after each fracture propagation step (Paluszny & Zimmerman, 2011; Secchi et al., 2007; Simoni & Secchi, 2003). The propagation results in the modification of fracture geometry and changes in the grid to ensure that the grid face coincides with the fracture extension. As a result, with the conforming grid approach combined with ARM, capturing the propagating fractures with a rather coarse mesh is possible.

Based on the above discussion, we use the conforming grid approach associated with the adaptive remeshing technique. The grid generation details will be discussed later.

4.1 Time discretization

Papers B, C, and D include a mathematical model that contains a first-order derivative with respect to time. To ensure stability with relatively large time steps, Backward Euler's method (also known as the implicit scheme) is used (John Charles Butcher, 2003). Typically, we address with an initial value problem as follows:

$$\frac{\partial \mathbf{x}(t)}{\partial t} = \mathbf{y}(\mathbf{x}, t), \quad \mathbf{x}(0) = \mathbf{x}_0, \tag{30}$$

where $\mathbf{x}$ is an unknown vector, and $\mathbf{y}$ is a nonlinear function.

Let $t_k, k = 0, 1, 2, \ldots$, be a sequence in time with time step Δt, then $t_{k+1} = t_k + \Delta t$. Therefore, $\mathbf{x}(t_{k+1})$ is obtained from $\mathbf{x}(t_k)$ as follows:

$$\mathbf{x}(t_{k+1}) = \mathbf{x}(t_k) + \Delta t \mathbf{y}[\mathbf{x}(t_{k+1}), t_{k+1}]. \tag{31}$$

As shown in Eq. (31), the new approximation $\mathbf{x}(t_{k+1})$ appears on both sides of the equation, so an iteration method, such as Newton, can be used to find the solution.

4.2 Spatial grids

The utilization of the mixed-dimensional model requires the adoption of mixed-dimensional grids for spatial discretization, which pertains to the computational grid used in each subdomain. Specifically, we discretize the computational domain by three distinct groups of grids. These grids are designed to match each other. The first group is a 2D grid for Ω^{M}, denoted by Ω_h, which contains the nonoverlapping triangle computational cells conforming to the fractures. The cells around the fracture are significantly smaller than the others. In this grid, the nodes and faces along the fracture are split to capture the discontinuity caused by the fractures. The second group is 1D grids containing the nonoverlapping segments generated for Ω^{F} and Γ, denoted by Ω_l. The 1D grid matches the 2D grid, i.e., the segments are identical to the faces along the fractures of the 2D grid. The last group has points, i.e., 0D grids, generated for Ω^{I} and Λ. An illustration of the mixed-dimensional grids can be found in (Keilegavlen et al., 2021). When considering the pure mechanics (i.e., the model presented in Sections 3.1–3.3), only 2D and 1D grids are needed for the simulation, as were used in Papers A and B. Otherwise, the fully coupled model needs all three groups of grids for discretization, as was used in Papers C and D.

4.3 Numerical approach

The selection of a numerical method for spatial discretization relies on the characteristics of the problem under consideration. Based on the properties of the FEM and FVM discussed earlier in this thesis, we divide the mathematical model into two submodels: coarse- and fine-level models. Then, we use the FVM and FEM for discretization in each model.

The coarse-level model, as presented in Chapter 3 with the exception of the fracture propagation criteria, describes the poroelasticity and fracture contact mechanics (as demonstrated in Papers C and D). This model considers the coupling between the fluid flow, deformation, and fracture contact mechanics in the porous media but does not directly

incorporate fracture propagation. Meanwhile, the fine-level model, which involves deformation and fracture propagation in a linear elasticity domain, is represented by Eqs. (1) - (10) and is demonstrated in Paper A. The fine-level model can be extended to include fracture contact mechanics by considering Eqs. (11) - (15), as demonstrated in Paper B.

The concepts of coarse and fine come from the numerical implementation, in which a coarse grid is used to discretize the poroelasticity and fracture contact mechanics. In contrast, a finer grid is used to simulate fracture propagation. The use of both coarse-level and fine-level grids aims to reduce the simulation cost while limiting the error of the numerical solution. For example, considering the fluid flow problem in porous media, a coarse grid is acceptable for discretization because the flow is considered laminar with a low velocity. In contrast, fracture propagation is sensitive to any change in the stress field around the tip. Thus, a fine grid will ensure a better capture of the fracture propagation.

The finite volume method (FVM) and the finite element method (FEM) are employed to discretize the coarse-level and fine-level models, respectively, to simulate the behavior of fractured porous media under various conditions. FVM allows for accurate modeling of the fluid flow behavior in the fracture and porous media, while FEM captures the deformation of the fractured domain. To ensure accurate simulations, it is crucial to consider the coupling between the two submodels. In the fine-level model, the displacement on the fracture surfaces is constrained by that from the coarse-level model. Meanwhile, the coarse-level fracture geometry is updated based on the fine-level fracture propagation. This ensures a continuous representation of the evolving geometry in both models.

As both the coarse-level and fine-level models are based on elliptic problems, the following subsection will provide a brief overview of the FVM and FEM for general elliptic problems. Additionally, we will discuss our approach to treating fracture contact mechanics, fracture propagation, and coalescence. A general elliptic steady-state problem for 2D solid mechanics is defined as

$$\nabla_s^{\mathrm{T}} \cdot \boldsymbol{\sigma} + \tilde{\mathbf{q}}_s = 0 \qquad \text{on } \Omega^{\mathrm{M}}, \tag{32}$$

$$\boldsymbol{\sigma} = \mathbf{D}\nabla_s \mathbf{u} \quad \text{on } \Omega^{\mathrm{M}}, \tag{33}$$

where $\boldsymbol{\sigma}$ is the stress and $\mathbf{u}$ is the displacement. $\mathbf{D}$ is the material matrix obtained from the elasticity tensor. ∇_s denotes the gradient operators.

A general elliptic steady-state problem for fluid flow is defined as

$$\nabla \cdot \mathbf{q} = \tilde{q}_f \quad \text{on } \Omega, \tag{34}$$

$$\mathbf{q} = -\mathbf{T}\nabla p \quad \text{on } \Omega, \tag{35}$$

where Ω is the computational domain, such as Ω^{M} or Ω^{F}. $\mathbf{q}$ is the flux, and p is the pressure. $\mathbf{T}$ is the matrix defined as permeability divided by viscosity.

4.3.1 Finite volume methods

The domain Ω is discretized by a set of computational cells $\{\Omega_e\}$. At each cell Ω_e, the discretization of Eqs. (32) and (34) by FVM is defined as

$$\int_{\partial\Omega_e} \boldsymbol{\sigma} \cdot \mathbf{n} \mathrm{d}l = \int_{\Omega_e} \tilde{\mathbf{q}}_s \mathrm{d}\Omega, \tag{36}$$

$$-\int_{\partial\Omega_e} \mathbf{q} \cdot \mathbf{n} \mathrm{d}l = \int_{\Omega_e} \tilde{q}_f \mathrm{d}\Omega, \tag{37}$$

where $\partial\Omega_e$ denotes the faces of cell Ω_e. Eqs. (36) and (37) are obtained by integrating Eqs. (32) and (34) over each computational cell and applying the divergence theorem. The body force and source/sink term are explicitly defined, so appropriate quadrature rules can be used to compute the right-hand side of Eqs. (36) and (37). The left-hand sides of Eqs. (36) and (37) are the stress and flux acting on the boundary of the computational cells, which can be assumed to be the approximate value at the face center and can be approximated by

$$\frac{1}{|\gamma^{kl}|}\int_{\gamma^{kl}} \boldsymbol{\sigma}\cdot\mathbf{n}\mathrm{d}l \approx \boldsymbol{\sigma}^{kl} = \sum_{e=1}^{n_c} \mathbf{d}_{\Omega_e}^{kl}\mathbf{u}_{\Omega_e}, \tag{38}$$

$$\frac{1}{|\gamma^{kl}|}\int_{\gamma^{kl}} \mathbf{q}\cdot\mathbf{n}\mathrm{d}l \approx \mathbf{q}^{kl} = \sum_{e=1}^{n_c} t_{\Omega_e}^{kl} p_{\Omega_e}, \tag{39}$$

where γ denotes the face in the computational grid. $\mathbf{d}_{\Omega_e}^{kl}$ and $t_{\Omega_e}^{kl}$ are the transmissibilities from cell Ω_e to face γ^{kl}, which are defined from **D** and **T**. $\mathbf{u}_{\Omega_e}$ and p_{Ω_e} are the displacement and pressure representing cell Ω_e, which can be assumed to be the approximate values at the center of the cell.

Depending on the determination of the cells that connect to the face γ^{kl}, this method can be classified into a two-point flux approximation (TPFA) and multipoint flux/stress approximation (MPFA/MPSA) (Aavatsmark, 2002; Nordbotten, 2015, 2016). Specifically, if γ^{kl} is the common face of cells Ω_k and Ω_l, then $n_c = 2$, and the discretization in Eq. (39) leads to the TPFA. On the other hand, if a cell Ω_e and face γ^{kl} share at least one vertex, n_c is the total number of cells that connect to face γ^{kl}. In this case, the discretization in Eqs. (38) and (39) lead to MPSA and MPFA, respectively.

For the poroelasticity problem, the displacement and pressure interact, so the discretization should treat the coupled system of deformation and flow directly instead of combining the discretizations for the two separate subproblems. This approach ensures both accuracy and computational efficiency. An implementation of this approach is the MPFA/MPSA-FVM proposed by Nordbotten (Nordbotten, 2016).

By implementing the discretization presented by Eqs. (38) and (39) for all computational cells, then assembling, we obtain a linear system given by the potential

$$\mathbf{A}\mathbf{v} = \mathbf{B}, \tag{40}$$

where **A** is the discretization matrix, **v** is the vector of potentials associated with each cell, and **B** is the integrated source/sink term and possible boundary conditions.

4.3.2 Finite element methods

By multiplying the governing equation (32) with a test function and integrating over each computational cell, ignoring the boundary condition, the FEM weak formulation is defined by

$$\int_{\Omega_e} (\nabla_s \mathbf{u}_h)^{\mathrm{T}} \mathbf{D} \nabla_s \bar{\mathbf{u}}_h \mathrm{d}\Omega = \int_{\Omega_e} \tilde{\mathbf{q}}_s \bar{\mathbf{u}}_h \mathrm{d}\Omega \quad \text{on } \Omega, \tag{41}$$

where $\mathbf{u}_h$ is the approximate solution and $\bar{\mathbf{u}}_h$ is the test function.

The variables $\mathbf{u}_h$ and $\bar{\mathbf{u}}_h$ in Eq. (41) are then approximated by the values at the nodes located at the vertices and middle of the faces of each computational cell through the shape functions. The shape functions are constructed based on singularity elements for the cells around the fracture tip and, as the usual quadratic function for the remaining cells. Similar to the coarse-level domain, a linear equation is also obtained in the fine-level domain to find an approximate solution for the mathematical model. Details are presented in Paper B.

4.3.3 Discretization for fracture contact mechanics

To incorporate the fracture contact mechanics into the model, it is necessary to discretize the contact traction and displacement on the fracture surfaces, and determine the state of the surfaces based on these discrete variables. The numerical solution obtained from the coarse-level model is used to approximate the discrete contact traction, $\mathbf{f}(\mathbf{x})$, based on Eq. (29), and the displacement jump on the fracture surfaces, $[\![\mathbf{u}(\mathbf{x})]\!]$, where $\mathbf{x}$ represents a point corresponding to an element in Ω_l. Using the discrete variables $\mathbf{f}(\mathbf{x})$ and $[\![\mathbf{u}(\mathbf{x})]\!]$, we check the nonpenetration condition and Coulomb friction law, as presented in Section 3.3, to determine the state of each element - whether it is open, sticking, or sliding. This checking of the state of the fracture surfaces is accomplished using an active set approach (Hintermüller et al., 2002; Hüeber & Wohlmuth, 2005; Wohlmuth, 2011).

First, at each time step, we predict a set of possible contact points $\{\mathbf{x}, \mathfrak{R}(\mathbf{x})\}$, where $\mathbf{x} \in \Gamma^+$ and $\mathfrak{R}(\mathbf{x})$ is the projection of $\mathbf{x}$ in Γ^-. Then we define the normal and tangential tractions

$(f_{\mathrm{n}}(\mathbf{x}), f_{\tau}(\mathbf{x}))$ on Γ^{+} as a set of Lagrange multipliers, and the displacement jump $([\![\mathbf{u}(\mathbf{x})]\!]_{\mathrm{n}}, [\![\mathbf{u}(\mathbf{x})]\!]_{\tau})$ on Γ. After that, we define a friction bound by $b^{k}(\mathbf{x}) = \mu_s\left[-f_{\mathbf{n}}^{k}(\mathbf{x}) + c\left([\![\mathbf{u}(\mathbf{x})]\!]_{\mathbf{n}}^{k} - g(\mathbf{x})\right)\right]$, where $c > 0$ is a given numerical parameter, and k is the iteration step. The nonpenetration condition and Coulomb friction, presented in inequalities (14) and (15), can be rewritten as a nonlinear optimization problem by means of the complementary functions

$$C_{\mathbf{n}}\left([\![\mathbf{u}(\mathbf{x})]\!]_{\mathrm{n}}, f_{\mathrm{n}}(\mathbf{x})\right) = -f_{\mathrm{n}}(\mathbf{x}) - \frac{1}{\mu_s}\max\{0, b^{k}(\mathbf{x})\}, \tag{42}$$

$$\begin{aligned} C_{\tau}\left([\![\dot{\mathbf{u}}(\mathbf{x})]\!]_{\tau}, f_{\tau}(\mathbf{x})\right) & \\ = -f_{\tau}(\mathbf{x}) \cdot \max\{b^{k}(\mathbf{x}), \|-f_{\tau}(\mathbf{x}) + c[\![\mathbf{u}(\mathbf{x})]\!]_{\tau}\|\} & \\ - (-f_{\tau}(\mathbf{x}) + c[\![\dot{\mathbf{u}}(\mathbf{x})]\!]_{\tau})\max\{0, b^{k}(\mathbf{x})\}. & \end{aligned} \tag{43}$$

When $C_{\mathbf{n}}\left([\![\mathbf{u}(\mathbf{x})]\!]_{\mathrm{n}}, f_{\mathrm{n}}(\mathbf{x})\right) = 0$ and $C_{\tau}\left([\![\dot{\mathbf{u}}(\mathbf{x})]\!]_{\tau}, f_{\tau}(\mathbf{x})\right) = 0$, we find the solution pair $\{\mathbf{u}(\mathbf{x}), \mathbf{f}(\mathbf{x})\}$ that satisfies the nonpenetration condition and the Coulomb friction law. Equation $C_n = 0$ and $C_\tau = 0$ can be solved by a semismooth Newton scheme, which results in an active set strategy.

4.3.4 Fracture propagation, coalescence and grid update

As discussed in Section 3.2, fracture propagation is evaluated by SIFs, which can be estimated using the nodal displacement correlation technique (Barsoum, 1977; Parks, 1974). In this method, K_{I} and K_{II} are estimated through normal and tangent displacements at some point near the fracture tip, respectively (Barsoum, 1977; Chen & Kuang, 1992; Kuang & Chen, 1993). The accuracy of this method has been verified through previously published studies (Fu et al., 2012; Nikishkov, 2013; Ramamurthy et al., 1986).

To simulate fracture propagation, the propagation length must also be determined, in addition to determining the propagation direction. In fact, for any acting force, the fracture always grows a corresponding length that may be below the resolution of the grid. Instead, the new fracture is updated and taken into account in the model if the fracture propagates

to a sufficient distance. In this study, the propagation length is computed by a Paris-type law (Paris & Erdogan, 1963). This law assumes that a single fracture inside a fine-level domain grows with a length equal to a preset value. If more than one fracture grows simultaneously, the tips with higher energy advance further than the others (Paris & Erdogan, 1963; Renshaw & Pollard, 1994).

This work also allows fractures to coalesce, and assumes the connection by a T-type model. They are considered connected when the distance between a growing crack tip, and a boundary or another fracture, is less than the crack tip rosette radius. Then the fracture is extended by a connection point defined by the projection of the fracture tip on the boundary. Finally, splitting the new fracture extension path creates a T-type connection. Details can be found in Papers B and D.

Grid updates are implemented independently in the coarse-level and fine-level grids. In the fine-level domain, the grid is updated whenever a fracture is propagated. However, small increases in the fracture length on the fine-level domain are not immediately projected to the coarse-level problem for simulation efficiency. Instead, a fracture propagating on the fine-level domain is updated on the coarse-level fracture only when they are connected, or when the change is significant enough to affect the coarse-level domain. Further details on the grid update process can be found in Papers C and D.

Chapter 5: Summary and outlook

5.1 Summary of papers

This chapter describes each of the four papers constituting Part II.

Paper A

Title: Numerical investigation of wing crack initiation and propagation due to shear slip

Authors: Hau Trung Dang, Eirik Keilegavlen, Inga Berre

Book: European Geothermal Congress. 2019

Paper A presents a simple numerical modeling and an adaptive remeshing method (ARM) to simulate fracture propagation in rock material. The ARM technique helps reduce the computational costs and accurately captures the geometrical changes caused by fracture propagation. The model is established based on linear elasticity theory and the maximum tangential stress criterion. The ARM technique is developed based on an error estimator, deleted-replaced process, and Laplacian smoothing. The numerical solution approach is based on combining the finite element method with quarter-point elements to handle the singularity at the fracture tips. The main contribution of Paper A is to present a mathematical model and numerical approach to simulate the initiation, propagation, and coalescence of wing cracks caused by compression and shear slip.

Paper B

Title: Numerical modeling of wing crack propagation accounting for fracture contact mechanics

Authors: Hau Trung Dang, Eirik Keilegavlen, Inga Berre

Journal: International Journal of Solids and Structures. Volumes 204–205, Pages 233-247. 2020

One of the restrictions of the model presented in Paper A is that it ignores the fracture contact mechanics. Paper B, hence, based on the previously proposed model, accounts for the fracture contact mechanics, in which fracture surfaces are allowed to be in contact or fully open. In this contact model, a nonpenetration condition is enforced in the normal direction of the fracture segments. For the tangential direction, either the fracture surfaces are modeled as frictionless, or the displacement jump in the tangential direction is specified. The proposed model also has the ability to consider multiple fractures propagating simultaneously at different speeds based on Paris's law. This paper uses ARM technique to ensure computational efficiency. The obtained results are verified by analytical solutions and experimental observations to show the accuracy of the presented model. In addition, more complex numerical test cases demonstrated the capabilities of this model in investigating the development of wing cracks for situations where multiple fractures interact.

Paper C

Title: Two-level simulation of injection-induced fracture slip and wing-crack propagation in poroelastic media

Authors: Hau Trung Dang, Eirik Keilegavlen, Inga Berre

Journal: International Journal of Rock Mechanics and Mining Sciences. Vol. 160, 105248. 2022

This study extends Paper B to a fully coupled model for fracture propagation caused by anisotropic compressive stresses and fluid injection. The governing mathematical model is based on Biot's model, with the contact mechanics representing the deformation of the existing fractures. The normal contact traction and the friction between the fracture surface are considered in the proposed model. A two-level simulation was presented to reduce the

computational costs and ensure accuracy. The numerical approach employs a novel combination of finite volume methods for the poroelastic deformation of the existing fractures with a finite element approach for the fracture propagation process. The obtained results show that the current model has potential in the simulation of mixed-mechanism hydraulic stimulation of fractured reservoirs. Both fracture shearing and the corresponding wing-crack propagation lead to an increase in permeability.

Paper D

Title: Modeling of mixed-mechanism stimulation for the enhancement of geothermal reservoirs

Authors: Hau Trung Dang, Eirik Keilegavlen, Inga Berre

Journal: Submitted manuscript. 2023

This study builds upon the mathematical model presented in Paper C by considering the coalescence between fractures. We conduct numerous complex numerical test cases to better comprehend the role and impact of mixed-mechanism stimulations on permeability in fractured geothermal reservoirs. The obtained results indicate the following:

1) Fluid injection at low pressure causes shear slip and dilation of the fractures, depending on the principal stress scenario.

2) A more permeable bulk domain causes flow leakage and slows fracture growth. Thus, stimulation by a low-pressure fluid injection may not be as effective for areas with high permeability.

3) The relationship between the injection rate and fracture growth speed is nonlinear. It takes a significantly longer injection time at a low rate for the fracture to propagate than in the higher rate case. Hence, if an injection is at a too-low rate, fracture propagation may not occur.

4) The location of the preexisting fractures can significantly impact the expansion of the fracture network. Fractures generally propagate along the direction of the maximum principal stress, and the presence of preexisting fractures can either facilitate or restrain the development of the propagating fractures.

5.2 Summary and outlook

Collecting the contributions described in the previous section, this section provides a unified summary of the thesis before some possible extensions and future possibilities are suggested.

This thesis presented a mathematical model and numerical approach to simulate injection-induced fracture slip and wing-crack propagation in fractured porous media. The model is based on a coupled hydromechanical model, considering poroelastic and fracture contact mechanics, allowing the preexisting fracture to grow and coalesce through a fracture propagation model. A two-level simulation is presented to reduce the computational costs and ensure accuracy. A finite volume method is combined with an active set strategy to discretize the poroelastic deformation of the existing fractures on the coarse level. The implementation is performed by PorePy for this level. A finite element method is combined with collapsed quarter-point elements at the fracture tips to capture the stress singularity for fracture propagation on the fine level. Adaptive remeshing, based on an error estimator and Laplacian smoothing, was introduced on both levels to account for fracture propagation.

The verification and validation for pure mechanics have been presented, showing an appropriate agreement between the analytical solutions and experimental observations for single fracture computations. For more complicated simulations, i.e., the propagation of multiple fractures under anisotropic principal stresses and fluid injection, the stability of the solution with different time steps, coarse-level grid sizes, and fine-level grid sizes was verified. This approach is capable of simulating complex problems, such as the simultaneous propagation of multiple fractures combined with the slip and dilation of

fractures in contact and tensile openings. In addition, hydraulically and mechanically interacting fractures are handled naturally.

Some of the results obtained in Paper D show that the effect of mixed mechanism stimulations can significantly enhance fracture permeability and connectivity. The effect on the enhancement of overall reservoir permeability in geothermal reservoirs will, in general, be complex. As this paper has shown, parameters such as the background stress state, permeability of the porous medium, injection rate, and fracture location significantly affect the expansion of the fracture network.

Therefore, the results in this thesis partly help us better understand the hydromechanical mechanisms of fracture slip, opening, and propagation in geothermal reservoirs, and the parameters that may affect the efficiency of geothermal energy extractions.

Although the results of modeling hydromechanical interactions in fractured porous media are impressive, this work still has limitations that need improvement to extend the application into practice. First, the model developed is 2D, which is unrealistic when geothermal reservoirs are complex 3D structures. Therefore, a 2D model is incapable of simulating physical phenomena accurately. Second, the flow in this study is assumed to be single phase. In reality, flow in the subsurface is multicomponent and multiphase with complex physical properties. Third, a phase change can occur under high temperatures in geothermal reservoirs, so it should be included in the model. Finally, fracture initiation should not be limited to emerging from preexisting fracture tips, and fracture connectivity should be considered in more forms, such as crossings with or without an offset. Hopefully, we will see new studies address the current limitations in the coming years.

Bibliography

Aavatsmark, I. (2002). An Introduction to Multipoint Flux Approximations for Quadrilateral Grids. *Computational Geosciences*, *6*(3), 405–432. https://doi.org/10.1023/A:1021291114475

Abe, A., & Horne, R. N. (2023). Investigating fracture network creation and stimulation mechanism of EGS reservoirs. *Geothermics*, *107*, 102606. https://doi.org/10.1016/j.geothermics.2022.102606

Adachi, J., Siebrits, E., Peirce, A., & Desroches, J. (2007). Computer simulation of hydraulic fractures. *International Journal of Rock Mechanics and Mining Sciences*, *44*(5), 739–757. https://doi.org/10.1016/j.ijrmms.2006.11.006

Anderson, T. L. (2017). *Fracture Mechanics: Fundamentals and Applications, Fourth Edition*. CRC Press.

Barsoum, R. S. (1977). Triangular quarter-point elements as elastic and perfectly-plastic crack tip elements. *International Journal for Numerical Methods in Engineering*, *11*(1), 85–98. https://doi.org/10.1002/nme.1620110109

Bear, J. (1993). *1 - Modeling Flow and Contaminant Transport in Fractured Rocks* (J. Bear, C.-F. Tsang, & G. B. T.-F. and C. T. in F. R. de Marsily, Eds.; pp. 1–37). Academic Press. https://doi.org/10.1016/B978-0-12-083980-3.50005-X

Bear, J. (2013). *Dynamics of Fluids in Porous Media*. Dover Publications, INC.

Belytschko, T., & Black, T. (1999). Elastic crack growth in finite elements with minimal remeshing. *International Journal for Numerical Methods in Engineering*, *45*(5), 601–620. https://doi.org/10.1002/(SICI)1097-0207(19990620)45:5<601::AID-NME598>3.0.CO;2-S

Berge, R. L., Berre, I., Keilegavlen, E., Nordbotten, J. M., & Wohlmuth, B. (2020). Finite volume discretization for poroelastic media with fractures modeled by contact mechanics. *International Journal for Numerical Methods in Engineering*, *121*(4), 644–663. https://doi.org/10.1002/nme.6238

Berkowitz, B. (2002). Characterizing flow and transport in fractured geological media: A review. *Advances in Water Resources*, *25*(8–12), 861–884. https://doi.org/10.1016/S0309-1708(02)00042-8

Berre, I., Doster, F., & Keilegavlen, E. (2019). Flow in Fractured Porous Media: A Review of Conceptual Models and Discretization Approaches. *Transport in Porous Media*, *130*(1), 215–236. https://doi.org/10.1007/s11242-018-1171-6

Berre, I., Stefansson, I., & Keilegavlen, E. (2020). Fault slip in hydraulic stimulation of geothermal reservoirs: Governing mechanisms and process-structure interaction. *The Leading Edge*, *39*(12), 893–900. https://doi.org/10.1190/tle39120893.1

Beuth, J. L., & Herakovich, C. T. (1989). Analysis of crack extension in anisotropic materials based on local normal stress. *Theoretical and Applied Fracture Mechanics*, *11*(1), 27–46. https://doi.org/10.1016/0167-8442(89)90023-2

Biot, M. A. (1941). General theory of three-dimensional consolidation. *Journal of Applied Physics*, *12*(2), 155–164.

Buczek, M. B., & Herakovich, C. T. (1985). A Normal Stress Criterion for Crack Extension Direction in Orthotropic Composite Materials. *Journal of Composite Materials*, *19*(6), 544–553. https://doi.org/10.1177/002199838501900606

Carloni, C., & Nobile, L. (2005). Maximum circumferential stress criterion applied to orthotropic materials. *Fatigue & Fracture of Engineering Materials & Structures*, *28*(9), 825–833. https://doi.org/10.1111/j.1460-2695.2005.00922.x

Chang, J., Xu, J., & Mutoh, Y. (2006). A general mixed-mode brittle fracture criterion for cracked materials. *Engineering Fracture Mechanics*, *73*(9), 1249–1263. https://doi.org/10.1016/j.engfracmech.2005.12.011

Chen, L. S., & Kuang, J. H. (1992). A modified linear extrapolation formula for determination of stress intensity factors. *International Journal of Fracture*, *54*(1), R3–R8. https://doi.org/10.1007/BF00040859

de Borst, R. (2017). Fluid flow in fractured and fracturing porous media: A unified view. *Mechanics Research Communications*, *80*, 47–57. https://doi.org/10.1016/j.mechrescom.2016.05.004

Dietrich, P., Helmig, R., Sauter, M., Hötzl, H., Köngeter, J., & Teutsch, G. (2005). *Flow and Transport in Fractured Porous Media*. Springer-Verlag. https://doi.org/10.1007/b138453

Eggertsson, G. H., Lavallée, Y., Kendrick, J. E., & Markússon, S. H. (2020). Improving fluid flow in geothermal reservoirs by thermal and mechanical stimulation: The case of Krafla volcano, Iceland. *Journal of Volcanology and Geothermal Research*, *391*, 106351. https://doi.org/10.1016/j.jvolgeores.2018.04.008

Erdogan, F., & Sih, G. C. (1963). On the Crack Extension in Plates Under Plane Loading and Transverse Shear. *Journal of Basic Engineering*, *85*(4), 519–525. https://doi.org/10.1115/1.3656897

Frih, N., Martin, V., Roberts, J. E., & Saâda, A. (2012). Modeling fractures as interfaces with nonmatching grids. *Computational Geosciences*, *16*(4), 1043–1060. https://doi.org/10.1007/s10596-012-9302-6

Fu, P., Johnson, S. M., Settgast, R. R., & Carrigan, C. R. (2012). Generalized displacement correlation method for estimating stress intensity factors. *Engineering Fracture Mechanics*, *88*, 90–107. https://doi.org/10.1016/j.engfracmech.2012.04.010

Golovin, S. V, Isaev, V. I., Baykin, A. N., Kuznetsov, D. S., & Mamontov, A. E. (2015). Hydraulic fracture numerical model free of explicit tip tracking. *International Journal of Rock Mechanics and Mining Sciences*, *76*(Supplement C), 174–181. https://doi.org/10.1016/j.ijrmms.2015.03.003

Gueguen, Y., & Palciauskas, V. (1994). *Introduction to the Physics of Rocks*. Princeton University Press.

Hintermüller, M., Ito, K., & Kunisch, K. (2002). The Primal-Dual Active Set Strategy as a Semismooth Newton Method. *SIAM Journal on Optimization*, *13*, 865–888. https://doi.org/10.1137/S1052623401383558

Hossain, M., Rahman, M., & Rahman, S. S. (2002). A Shear Dilation Stimulation Model for Production Enhancement From Naturally Fractured Reservoirs. *SPE Journal - SPE J*, *7*, 183–195. https://doi.org/10.2118/78355-PA

Hüeber, S., & Wohlmuth, B. (2005). A primal–dual active set strategy for non-linear multibody contact problems. *Computer Methods in Applied Mechanics and Engineering*, *194*, 3147–3166. https://doi.org/10.1016/j.cma.2004.08.006

Hunsweck, M. J., Shen, Y., & Lew, A. J. (2013). A finite element approach to the simulation of hydraulic fractures with lag. *International Journal for Numerical and Analytical Methods in Geomechanics*, *37*(9), 993–1015. https://doi.org/10.1002/nag.1131

Ingraffea, A. R., & Heuze, F. E. (1980). Finite element models for rock fracture mechanics. *International Journal for Numerical and Analytical Methods in Geomechanics*, *4*(1), 25–43. https://doi.org/10.1002/nag.1610040103

Irwin, G. R. (1957). Analysis of Stresses and Strains Near the End of a Crack Traversing a Plate. *Journal of Applied Mechanics*, *24*(3), 361–364. https://doi.org/10.1115/1.4011547

John Charles Butcher. (2003). *Numerical Methods for Ordinary Differential Equations*. John Wiley & Sons.

Jung, R. (2013). EGS — Goodbye or Back to the Future. In *Effective and Sustainable Hydraulic Fracturing* (pp. 95–121). InTech. https://doi.org/10.5772/56458

Kashif, M., Cao, Y., Yuan, G., Asif, M., Javed, K., Mendez, J. N., Khan, D., & Miruo, L. (2019). Pore size distribution, their geometry and connectivity in deeply buried Paleogene Es1 sandstone reservoir, Nanpu Sag, East China. *Petroleum Science*, *16*(5), 981–1000. https://doi.org/10.1007/s12182-019-00375-3

Keilegavlen, E., Berge, R., Fumagalli, A., Starnoni, M., Stefansson, I., Varela, J., & Berre, I. (2021). PorePy: an open-source software for simulation of multiphysics processes in fractured porous media. *Computational Geosciences*, *25*(1), 243–265. https://doi.org/10.1007/s10596-020-10002-5

Khoei, A. R., & Nikbakht, M. (2006). Contact friction modeling with the extended finite lement method (X-FEM). *Journal of Materials Processing Technology*, *177*, 58–62. https://doi.org/10.1016/j.jmatprotec.2006.03.185

Kikuchi, N., & Oden, J. (1988). A study of variational inequalities and finite element methods. In *Contact Problems in Elasticity* (pp. 201–239). Society for Industrial and Applied Mathematics. https://doi.org/doi:10.1137/1.9781611970845.ch8

Kim, J., & Duarte, C. A. (2015). A new generalized finite element method for two-scale simulations of propagating cohesive fractures in 3-D. *International Journal for Numerical Methods in Engineering*, *104*(13), 1139–1172. https://doi.org/10.1002/nme.4954

Kolditz, O. (2002). *Finite Volume Method BT - Computational Methods in Environmental Fluid Mechanics* (O. Kolditz, Ed.; pp. 173–190). Springer Berlin Heidelberg. https://doi.org/10.1007/978-3-662-04761-3_8

Koponen, A., Kataja, M., & Timonen, J. (1997). Permeability and effective porosity of porous media. *Physical Review E*, *56*(3), 3319–3325. https://doi.org/10.1103/PhysRevE.56.3319

Kuang, J. H., & Chen, L. S. (1993). A displacement extrapolation method for two-dimensional mixed-mode crack problems. *Engineering Fracture Mechanics*, *46*(5), 735–741. https://doi.org/10.1016/0013-7944(93)90123-A

Lecampion, B. (2009). An extended finite element method for hydraulic fracture problems. *Communications in Numerical Methods in Engineering*, *25*(2), 121–133. https://doi.org/10.1002/cnm.1111

Lecampion, B., Bunger, A., & Zhang, X. (2017). Numerical methods for hydraulic fracture propagation: A review of recent trends. *Journal of Natural Gas Science and Engineering*, *49*. https://doi.org/10.1016/j.jngse.2017.10.012

Liu, F., Gordon, P., Meier, H., & Valiveti, D. (2017). A stabilized extended finite element framework for hydraulic fracturing simulations. *International Journal for Numerical and Analytical Methods in Geomechanics*, *41*(5), 654–681. https://doi.org/10.1002/nag.2565

Martin, V., Jaffré, J., & Roberts, J. (2005). Modeling Fractures and Barriers as Interfaces for Flow in Porous Media. *SIAM J. Scientific Computing*, *26*, 1667–1691. https://doi.org/10.1137/S1064827503429363

McClure, M. W., & Horne, R. N. (2011). Investigation of injection-induced seismicity using a coupled fluid flow and rate/state friction model. *GEOPHYSICS*, *76*(6), WC181–WC198. https://doi.org/10.1190/geo2011-0064.1

McClure, M. W., & Horne, R. N. (2014). An investigation of stimulation mechanisms in Enhanced Geothermal Systems. *International Journal of Rock Mechanics and Mining Sciences*, *72*, 242–260. https://doi.org/10.1016/j.ijrmms.2014.07.011

Mohammadnejad, T., & Khoei, A. R. (2013). An extended finite element method for hydraulic fracture propagation in deformable porous media with the cohesive crack model. *Finite Elements in Analysis and Design*, *73*(Supplement C), 77–95. https://doi.org/10.1016/j.finel.2013.05.005

Moukalled, F., Mangani, L., & Darwish, M. (2015). *The Finite Volume Method in Computational Fluid Dynamics: An Advanced Introduction with OpenFOAM® and Matlab*. Springer International Publishing.

Neuman, S. P. (2005). Trends, prospects and challenges in quantifying flow and transport through fractured rocks. *Hydrogeology Journal*, *13*(1), 124–147. https://doi.org/10.1007/s10040-004-0397-2

Nikishkov, G. P. (2013). Accuracy of Quarter-point Element in Modeling Crack-tip Fields. In *Computer Modeling in Engineering \& Sciences* (Vol. 93, Issue 5). https://doi.org/10.3970/cmes.2013.093.335

Norbeck, J. H., McClure, M. W., & Horne, R. N. (2018). Field observations at the Fenton Hill enhanced geothermal system test site support mixed-mechanism stimulation. *Geothermics*, *74*, 135–149. https://doi.org/10.1016/j.geothermics.2018.03.003

Nordbotten, J. M. (2015). Convergence of a cell-centered finite volume discretization for linear. *SIAM Journal on Numerical Analysis*, *53*(6), 2605–2625.

Nordbotten, J. M. (2016). Stable Cell-Centered Finite Volume Discretization for Biot Equations. *SIAM Journal on Numerical Analysis*, *54*(2), 942–968. https://doi.org/10.1137/15M1014280

Nordbotten, J. M., Boon, W. M., Fumagalli, A., & Keilegavlen, E. (2019). Unified approach to discretization of flow in fractured porous media. *Computational Geosciences*, *23*(2), 225–237. https://doi.org/10.1007/s10596-018-9778-9

Paluszny, A., & Zimmerman, R. W. (2011). Numerical simulation of multiple 3D fracture propagation using arbitrary meshes. *Computer Methods in Applied Mechanics and Engineering*, *200*(9), 953–966. https://doi.org/10.1016/j.cma.2010.11.013

Paris, P., & Erdogan, F. (1963). A Critical Analysis of Crack Propagation Laws. *Journal of Fluids Engineering*, *85*(4), 528–533. https://doi.org/10.1115/1.3656900

Parks, D. M. (1974). A stiffness derivative finite element technique for determination of crack tip stress intensity factors. *International Journal of Fracture*, *10*(4), 487–502. https://doi.org/10.1007/BF00155252

Pimienta, L., Fortin, J., & Guéguen, Y. (2017). New method for measuring compressibility and poroelasticity coefficients in porous and permeable rocks. *Journal of Geophysical Research: Solid Earth*, *122*(4), 2670–2689. https://doi.org/10.1002/2016JB013791

Pine, R. J., & Batchelor, A. S. (1984). Downward migration of shearing in jointed rock during hydraulic injections. *International Journal of Rock Mechanics and Mining Sciences & Geomechanics Abstracts*, *21*(5), 249–263. https://doi.org/10.1016/0148-9062(84)92681-0

Popov, V. L. (2010). *Coulomb's Law of Friction BT - Contact Mechanics and Friction: Physical Principles and Applications* (V. L. Popov, Ed.; pp. 133–154). Springer Berlin Heidelberg. https://doi.org/10.1007/978-3-642-10803-7_10

Rahman, M., Hossain, M., & Rahman, S. S. (2002). A shear-dilation-based model for evaluation of hydraulically stimulated naturally fractured reservoirs. *International Journal for Numerical and Analytical Methods in Geomechanics*, *26*, 469–497. https://doi.org/10.1002/nag.208

Ramamurthy, T. S., Krishnamurthy, T., Narayana, K. B., Vijayakumar, K., & Dattaguru, B. (1986). Modified crack closure integral method with quarter point elements. *Mechanics Research Communications*, *13*(4), 179–186. https://doi.org/10.1016/0093-6413(86)90016-9

Reichenberger, V., Jakobs, H., Bastian, P., & Helmig, R. (2006). A mixed-dimensional finite volume method for two-phase flow in fractured porous media. *Advances in Water Resources*, *29*(7), 1020–1036. https://doi.org/10.1016/j.advwatres.2005.09.001

Renshaw, C. E., & Pollard, D. D. (1994). Numerical simulation of fracture set formation: A fracture mechanics model consistent with experimental observations. *Journal of*

Geophysical Research: Solid Earth, *99*(B5), 9359–9372. https://doi.org/10.1029/94JB00139

Rice, J. R. (1968). A Path Independent Integral and the Approximate Analysis of Strain Concentration by Notches and Cracks. *Journal of Applied Mechanics*, *35*(2), 379–386. https://doi.org/10.1115/1.3601206

Sahimi, M. (2012). *Flow and Transport in Porous Media and Fractured Rock: From Classical Methods to Modern Approaches*. Wiley.

Salimzadeh, S., Paluszny, A., & Zimmerman, R. W. (2017). Three-dimensional poroelastic effects during hydraulic fracturing in permeable rocks. *International Journal of Solids and Structures*, *108*(Supplement C), 153–163. https://doi.org/10.1016/j.ijsolstr.2016.12.008

Saouma, V. E., Ayari, M. L., & Leavell, D. A. (1987). Mixed mode crack propagation in homogeneous anisotropic solids. *Engineering Fracture Mechanics*, *27*(2), 171–184. https://doi.org/10.1016/0013-7944(87)90166-4

Schoenball, M., Ajo-Franklin, J. B., Blankenship, D., Chai, C., Chakravarty, A., Dobson, P., Hopp, C., Kneafsey, T., Knox, H. A., Maceira, M., Robertson, M. C., Sprinkle, P., Strickland, C., Templeton, D., Schwering, P. C., Ulrich, C., Wood, T., & Team, T. E. G. S. C. (2020). Creation of a Mixed-Mode Fracture Network at Mesoscale Through Hydraulic Fracturing and Shear Stimulation. *Journal of Geophysical Research: Solid Earth*, *125*(12), e2020JB019807. https://doi.org/10.1029/2020JB019807

Secchi, S., Simoni, L., & Schrefler, B. A. (2007). Mesh adaptation and transfer schemes for discrete fracture propagation in porous materials. *International Journal for Numerical and Analytical Methods in Geomechanics*, *31*(2), 331–345. https://doi.org/10.1002/nag.581

Secretariat-REN21. (2021). *Renewables 2021 global status report*.

Settgast, R. R., Fu, P., Walsh, S. D. C., White, J. A., Annavarapu, C., & Ryerson, F. J. (2017). A fully coupled method for massively parallel simulation of hydraulically driven fractures in 3-dimensions. *International Journal for Numerical and Analytical Methods in Geomechanics*, *41*(5), 627–653. https://doi.org/10.1002/nag.2557

Sih, G. C. (1974). Strain-energy-density factor applied to mixed mode crack problems. *International Journal of Fracture*, *10*(3), 305–321. https://doi.org/10.1007/BF00035493

Simoni, L., & Secchi, S. (2003). Cohesive fracture mechanics for a multi-phase porous medium. *Engineering Computations*, *20*(5/6), 675–698. https://doi.org/10.1108/02644400310488817

Singhal, B., & Gupta, R. P. (2010). *Applied Hydrogeology of Fractured Rocks: Second Edition*. Springer Netherlands.

Stefansson, I., Berre, I., & Keilegavlen, E. (2021). A fully coupled numerical model of thermo-hydro-mechanical processes and fracture contact mechanics in porous media. *Computer Methods in Applied Mechanics and Engineering*, *386*, 114122. https://doi.org/10.1016/j.cma.2021.114122

Stefansson, I., Keilegavlen, E., Halldórsdóttir, S., & Berre, I. (2021). Numerical modelling of convection-driven cooling, deformation and fracturing of thermo-poroelastic media. *Transport in Porous Media*. https://doi.org/10.1007/s11242-021-01676-1

Tada, H., Paris, P. C., & Irwin, G. R. (2000). *The stress analysis of cracks handbook*. ASME Press.

Viswanathan, H. S., Ajo-Franklin, J., Birkholzer, J. T., Carey, J. W., Guglielmi, Y., Hyman, J. D., Karra, S., Pyrak-Nolte, L. J., Rajaram, H., Srinivasan, G., & Tartakovsky, D. M. (2022). From Fluid Flow to Coupled Processes in Fractured Rock: Recent Advances and New Frontiers. *Reviews of Geophysics*, *60*(1), e2021RG000744. https://doi.org/10.1029/2021RG000744

Weng, X. (2015). Modeling of complex hydraulic fractures in naturally fractured formation. *Journal of Unconventional Oil and Gas Resources*, *9*, 114–135. https://doi.org/10.1016/j.juogr.2014.07.001

Weng, X. ., Kresse, O. ., Cohen, C. ., Wu, R. ., & Gu, H. . (2011). Modeling of Hydraulic-Fracture-Network Propagation in a Naturally Fractured Formation. *SPE Production & Operations*, *26*(04), 368–380. https://doi.org/10.2118/140253-PA

Williams, J. G., & Ewing, P. D. (1984). Fracture under complex stress — The angled crack problem. *International Journal of Fracture*, *26*(4), 346–351. https://doi.org/10.1007/BF00962967

Witherspoon, P. A., Wang, J. S. Y., Iwai, K., & Gale, J. E. (1980). Validity of Cubic Law for fluid flow in a deformable rock fracture. *Water Resources Research*, *16*(6), 1016–1024. https://doi.org/10.1029/WR016i006p01016

Wohlmuth, B. (2011). Variationally consistent discretization schemes and numerical algorithms for contact problems. *Acta Numerica*, *20*, 569–734. https://doi.org/10.1017/S0962492911000079

Wriggers, P. (2006). *Computational Contact Mechanics*. Springer Berlin Heidelberg.

Zienkiewicz, O. C., & Taylor, R. L. (2013). *The Finite Element Method for Solid and Structural Mechanics*. Elsevier Science.

Zienkiewicz, O. C., Taylor, R. L., & Zhu, J. Z. (2005). *The Finite Element Method: Its Basis and Fundamentals*. Elsevier Science.

Zimmerman, R. W., & Bodvarsson, G. S. (1996). Hydraulic conductivity of rock fractures. *Transport in Porous Media*, *23*(1), 1–30. https://doi.org/10.1007/BF00145263

Part II: Scientific results

A **Numerical investigation of wing crack initiation and propagation due to shear slip**

Hau Trung Dang, Eirik Keilegavlen, Inga Berre

In Proceedings of European Geothermal Congress, 11-14 June 2019, Den Haag, The Netherlands.

https://europeangeothermalcongress.eu/wp-content/uploads/2019/07/304.pdf

B **Numerical modeling of wing crack propagation accounting for fracture contact mechanics**

Hau Trung Dang, Eirik Keilegavlen, Inga Berre

International Journal of Solids and Structures. Vol. 204–205: 233-247. 2020

DOI: 10.1016/j.ijsolstr.2020.08.017

https://www.sciencedirect.com/science/article/pii/S0020768320303152

C **Two-level simulation of injection-induced fracture shear deformation and wing-crack propagation in poroelastic media (2022)**

Hau Trung Dang, Eirik Keilegavlen, Inga Berre

International Journal of Rock Mechanics and Mining Sciences. Vol. 160, 105248. 2022

DOI: 10.1016/j.ijrmms.2022.105248

https://www.sciencedirect.com/science/article/pii/S1365160922002143

D **Modeling of mixed-mechanism stimulation for the enhancement of geothermal reservoirs**

Hau Trung Dang, Eirik Keilegavlen, Inga Berre

Submitted manuscript. 2023

Paper A

Numerical investigation of wing crack initiation and propagation due to shear slip

Hau Trung Dang, Eirik Keilegavlen, Inga Berre

In Proceedings of European Geothermal Congress, 11-14 June 2019, Den Haag, The Netherlands. 2019.

https://europeangeothermalcongress.eu/wp-content/uploads/2019/07/304.pdf

Numerical investigation of wing crack initiation and propagation due to shear slip

Hau Trung Dang[1], Eirik Keilegavlen[1], Inga Berre[1,2].

[1] Department of Mathematics, University of Bergen, Bergen, Norway

[2] NORCE, Bergen, Norway

Hau.Dang@uib.no

Keywords: Geothermal system, wing crack, fracture propagation, shear slip, adaptive remeshing technique.

ABSTRACT

The expansion of wing cracks produced by slip of fractures due to water injection at pressure far below the minimum principal stress affects the performance of geothermal system. This work investigates how the wing cracks are emerged, propagated and connected due to slip at the interfaces of a pre-existing fracture. A mathematical model is presented and followed by an adaptive remeshing technique for the simulation. Several numerical investigations are conducted to validate the present model and study the initiation and propagation of wing cracks.

1. INTRODUCTION

An enhanced geothermal system (EGS) is a volume of hot rock that has been stimulated by reactivating natural fractures in the subsurface. By water injection at low pressure, slip is caused if the reduction in normal stress is sufficient to overcome the frictional resistance to the shear stresses on the fracture. The slip of fracture surfaces in opposite directions can cause the fracture to propagate in the form of wing crack (Cheng et al. 2019; Jung 2013; Kamali and Ghassemi 2016; Lin et al. 2010). In a system of multiple pre-existing natural fractures, many wing cracks are created and filled by massive water injection during stimulation. Some of them result in new connected flow paths and enhance permeability (Norbeck et al. 2018). While the propagation of wing crack could be central in stimulation of geothermal reservoirs, the mechanism has been only to a limited extent been studied by mathematical modeling and simulation in this context. Further improvements in modeling and simulation, will lead to increased understanding of this mechanism, while predictions will still be challenging due to the uncertainties in initial stress acting on the natural fractures as well as their locations (Lin et al. 2010). This leads to the lack of knowledge about the mechanism of wing cracks in EGS.

Many studies about behaviours of wing cracks in specimens made of rock/rock-like materials have been published, both related to experimental observations (Abdollahipour and Fatehi Marji 2016; Ashby and Hallam 1986; Bobet and Einstein 1998; Haeri et al. 2014; Horii and Nemat-Nasser 1985; Ingraffea and Manu 1980; Janeiro and Einstein 2010; Lee and Jeon 2011; Li et al. 2005; Park and Bobet 2009; Park and Bobet 2010; Shen et al. 1995; Wong and Einstein 2009; Xu et al. 2018; Yang et al. 2009; Yang 2011) and mathematical modeling (Bryant and Sun 2018; Fatehi Marji 2014; Gonçalves da Silva and Einstein 2013; Haeri et al. 2013; Ingraffea and Heuze 1980; Li and Wong 2012; Sharafisafa and Nazem 2014; Sivakumar and Maji 2016; Xie et al. 2016; Zhang et al. 2017). In these experiments, it is observed that emerging wing cracks at the tips of pre-existing fractures tend to align with the direction of the maximum compressive stress. By mathematical modeling, the behaviour of wing cracks in brittle material is usually modeled by use of the stress intensity factors (Lehner and Kachanov 1996) and/or a fracture criteria (Erdogan and Sih 1963; Hussain et al. 1973; Sih 1974). The maximum tangential stress (MTS) criterion seems to be the best choice for wing crack modeling because of the simplification and agreement with the observed trajectories (Gonçalves da Silva and Einstein 2013; Ingraffea and Heuze 1980). All these studies focused on the formation, growth and connection of wing cracks under external compressive load, as is relevant for EGS applications.

An inherent problem in simulation of fracture propagation is the disparate lengths scales involved: While the simulation domain can be quite large – in an EGS setting the reservoir is commonly measured in at least hundreds of meters - the fracturing processes takes place on a scale that is several of orders of magnitude smaller. Moreover, most numerical methods for fracture propagation are dependent on resolving the fracture in the grid, however, the fracture path is not known *a priori*. A possible remedy for both these issues is to apply adaptive remeshing (ARM) techniques to refine and adjust the mesh around an advancing fracture path.

This paper aims to present the mathematical model and an ARM technique conjunction with finite element method to understand how do wing cracks emerge, propagate and connect in a 2D-EGS model due to slip of pre-existing fracture interfaces. First, in section 2, the mathematical model for a wing crack was formulated based on linear elasticity theory, in combination with the MTS criterion. The displacement

at interfaces of the pre-existing fracture is assumed to enforce a jump condition on displacement along the fracture. In section 3, a novel ARM technique that based on a simple error estimator, a deleted-displace process and Laplacian smoothing is proposed. The discretization will be presented in section 4. Several examples are discussed in section 5, in comparison with experiment data to validate and show the accuracy of the proposed model and procedure. Then a physical model is attempted to understand the role of wing cracks in shear stimulation of fractured geothermal reservoirs EGS.

2. GOVERNING EQUATIONS

Here we give the governing equations for the deformation of a linearly elastic medium, with emphasis on conditions placed on the boundaries of existing and newly created fractures. We also describe the criterion used to decide when and where a fracture will propagate.

2.1 Elasticity

Consider a plane strain domain $\Omega \subset \mathbb{R}^2$ with outward unit normal vector $\mathbf{n}$ on its boundary and a pre-existing fracture with boundary denoted by Γ_c as shown in Figure 1. The Dirichlet and Neumann conditions are applied on $\Gamma_D \subset \Omega$ and $\Gamma_N \subset \Omega$, respectively. For a linear elastic fracture problem, the strong form of governing equations can be expressed as

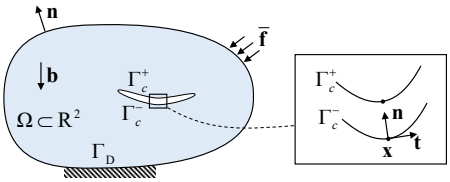

Figure 1: An elastic body containing a pre-existing fracture.

$$\begin{cases} \nabla\cdot\boldsymbol{\sigma}+\mathbf{b}=0 & \text{in } \Omega & \text{Equilibrium eq.} \\ \boldsymbol{\sigma}=\mathbf{C}:\boldsymbol{\varepsilon} & \text{in } \Omega & \text{Constitutive eq.} \\ \boldsymbol{\varepsilon}=\frac{1}{2}\left(\nabla\mathbf{u}+\nabla\mathbf{u}^{\mathrm{T}}\right) & \text{in } \Omega & \text{Kinematic eq.} \\ \mathbf{u}=\bar{\mathbf{u}} & \text{on } \Gamma_D & \text{Dirichlet BC} \\ \boldsymbol{\sigma}\cdot\mathbf{n}=\bar{\mathbf{f}} & \text{on } \Gamma_N & \text{Neumann BC} \end{cases} \quad [1]$$

where $\boldsymbol{\sigma}$, $\boldsymbol{\varepsilon}$ and $\mathbf{u}$ are the Cauchy stress tensor, the symmetric infinitesimal strain tensor and the displacement field, respectively. $\mathbf{C}$ is the fourth-order elasticity (Hooke's) tensor defined from Young's modulus, *E*, and Poisson's ratio, *v*. $\mathbf{b}$ is the body force. $\bar{\mathbf{u}}$ and $\bar{\mathbf{f}}$ are the prescribed displacement along the Dirichlet boundary and the applied traction along the Neumann boundary, respectively.

When a pre-existing fracture Γ_c is compressed and/or slipped, the normal jump displacement condition is imposed at the fractures' interfaces Γ_c^+ and Γ_c^-. As the focus in this work is on the effect of shear slip, it is for simplicity assumed that the normal fracture dilation is zero, i.e.,

$$\left[\mathbf{u}\right]_{\mathbf{n}}^{\Gamma_c}=\left[\mathbf{u}^{\Gamma_c^+}(\mathbf{x})-\mathbf{u}^{\Gamma_c^-}(\mathbf{x})\right]\cdot\mathbf{n}(\mathbf{x})=0 \quad [2]$$

For the tangential direction of Γ_c, two types of conditions are considered: Either, the fracture surfaces are modeled as frictionless, thus the tangential traction is zero at Γ_c,

$$\boldsymbol{\sigma}\cdot\mathbf{t}=0 \quad [3]$$

where $\mathbf{t}$ is the tangential vector on the surfaces of a pre-existing fracture. This assumption, in practice, leads to an exaggeration of the slip, but is acceptable herein, as the trajectory of fracture is the primary quantity of interest. For the friction-free case, the deformation of the elastic medium and the fractures contained within is driven by external boundary conditions on Γ_D and Γ_N, or by displacements on other fractures.

The second type of condition considered in the tangential direction of Γ_c is a specified displacment jump i.e.,

$$\left[\mathbf{u}\right]_{\mathbf{t}}^{\Gamma_c}=\left[\mathbf{u}^{\Gamma_c^+}(\mathbf{x})-\mathbf{u}^{\Gamma_c^-}(\mathbf{x})\right]\cdot\mathbf{t}=u_0' \quad [4]$$

where the total slip at Γ_c, u_0', is considered as known. In the context of low-pressure stimulation of geothermal systems, this type of condition applies to sliding fractures.

The wing cracks emerged after compressed and/or slipped are the tensile cracks (Bobet and Einstein 1998; Wong and Einstein 2009). This means that the surfaces of this cracks are in not contact and both normal and tangential tractions at these faces are zeros, i.e.,

$$\boldsymbol{\sigma}\cdot\mathbf{n}=\boldsymbol{\sigma}\cdot\mathbf{t}=0 \quad [5]$$

The wing cracks are not present in the computational domain at the start of the simulations. Indeed, the computation of the time of fracturing and the paths of wing cracks is the main challenge in this work.

2.2 Fracture criteria

The primary mechanism for permeability enhancement in the construction of EGS systems is believed to be sliding of pre-existing fractures. This motion will alter the stress field in the rock surrounding rock matrix, and may trigger propagation of new fractures, commonly denoted wing cracks, emanating from the fracture tips. The modeling and computation of this secondary fracturing is of interest in this work.

From the mathematical model for elastic deformation, the stress at an arbitrary point can be directly calculated for a certain problem. So, the fracture criteria based on maximum tensile stress (MTS) (Erdogan and Sih 1963) that is simple and accuracy (Gonçalves da Silva and Einstein 2013; Ingraffea and Heuze 1980), should be

adapted to predict the initiation and propagation of wing cracks in EGS. This criterion states that a crack grows when the maximum average tangential stress in the fracture process zone ahead of the crack tip reaches a critical value. Moreover, the crack growth direction coincides with the direction of the maximum average tangential stress along a constant radius around the crack tip. It is a local approach since it is based on local stress fields around the crack front. The tangential stress in around a crack tip is given by

$$\sigma_\theta = \frac{1}{\sqrt{2\pi l}}\left(K_I \cos^3\frac{\theta}{2} - \frac{3}{2}K_{II}\cos\frac{\theta}{2}\sin\theta \right) \quad [6]$$

The wing crack emerges if the tangential stress reaches a critical value, i.e.

$$\sigma_{\theta_0}\sqrt{2\pi l} = K_I \cos^3\frac{\theta_0}{2} - \frac{3}{2}K_{II}\cos\frac{\theta_0}{2}\sin\theta_0 = K_{IC} \quad [7]$$

where K_{IC} is the fracture toughness, θ_0 is the crack initiation angle with respect to the original crack plane. θ_0 is obtained by solving $\partial\sigma_\theta/\partial\theta = 0$ for θ and combining with sufficient condition $\partial^2\sigma_\theta/\partial\theta^2 < 0$ such as

$$\theta_0 = 2\tan^{-1}\left(\frac{1}{4}\mu \pm \frac{1}{4}\sqrt{\mu^2+8} \right),\ \mu = K_I/K_{II} \quad [8]$$

$$K_{II}\left(\sin\frac{\theta_0}{2} + 9\sin\frac{3\theta_0}{2} \right) < K_I\left(\cos\frac{\theta_0}{2} + 3\cos\frac{3\theta_0}{2} \right) \quad [9]$$

in which K_I and K_{II} are the stress intensity factors (SIFs), as parameters for the intensity of stresses close to the crack tip, can be evaluated by several techniques (Moran and Shih 1987; Parks 1974; Phongthanapanich and Dechaumphai 2004). In this work, SIFs are computed by the nodal displacement correlation technique (Parks 1974) in conjunction of collapsed quarter point singular elements (CQPE) (Barsoum 1976; Henshell and Shaw 1975). CQPEs considerably improve the numerical solution near the crack tip, result in more accurate computation of SIFs (Khoei et al. 2008). Through the displacement of CQPE around a crack tip, these SIFs can be calculated as

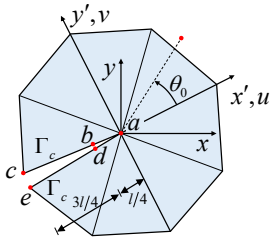

Figure 2: The collapsed quarter point singular elements around a crack tip.

$$K_I = \frac{E}{12(1-\nu^2)}\sqrt{\frac{2\pi}{l}}\left[4(v'_b - v'_d) - \frac{1}{2}(v'_c - v'_e) \right]$$
$$K_{II} = \frac{E}{12(1-\nu^2)}\sqrt{\frac{2\pi}{l}}\left[4(u'_b - u'_d) - \frac{1}{2}(u'_c - u'_e) \right] \quad [10]$$

where l is the crack tip rosette radius. u' and v' are the local displacements of nodal points located on the crack in CQPE, in which x' is aligned in the direction of crack axis, as shown in Figure 2.

3. DISCRETIZATION

The finite element discretization of the governing equations shown in the previous section are presented in this section, together with an adaptive remeshing technique. The propagation of wing cracks is complicated, and their trajectories are difficult to achieve by analytical approach. In this case numerical solutions by the finite element method (FEM) is a natural alternative. The finite element formulation is based on the weak formulation established from the governing equation and states: Find $\mathbf{u} \in V$ such that $\forall \mathbf{v} \in V$

$$\int_\Omega \mathbf{u}^{\mathrm{T}}\mathbf{L}^{\mathrm{T}}\mathbf{D}\mathbf{L}\mathbf{v}\mathrm{d}\Omega - \int_{\Gamma_c}\boldsymbol{\sigma}\cdot\mathbf{n}[\mathbf{v}]_{\mathbf{n}}\,\mathrm{d}\Gamma = \int_\Omega \mathbf{b}\mathbf{v}\mathrm{d}\Omega + \int_{\Gamma_N}\bar{\mathbf{f}}\mathbf{v}\mathrm{d}\Gamma \quad [11]$$

where $\mathbf{u}$ must be selected from a set of admissible functions in the space V such that

$$\mathbf{u} \in V := \left\{ \mathbf{v} \in H^1(\Omega),\ \mathbf{v}|_{\Gamma_u} = 0 \right\} \quad [12]$$

in which H^1 is the standard Sobolev space. In Eq. [11] $\mathbf{L}$ and $\mathbf{D}$ are the differential operator and the material matrix modified from $\mathbf{C}$ given by

$$\mathbf{L}^{\mathrm{T}} = \begin{bmatrix} \frac{\partial}{\partial x} & 0 & \frac{\partial}{\partial y} \\ 0 & \frac{\partial}{\partial y} & \frac{\partial}{\partial x} \end{bmatrix},\ \mathbf{D} = \frac{E}{1-\nu^2}\begin{bmatrix} 1 & \nu & 0 \\ \nu & 1 & 0 \\ 0 & 0 & \frac{1}{2}(1-\nu) \end{bmatrix} \quad [13]$$

3.1 Finite element method

The approximate solution of Eq. [11], denoted by $\mathbf{u}_h$, can be evaluated by using a subset of the allowable function space $V_h \subset V$ composed of first order Lagrangian shape functions, that is, piecewise linear functions. This requires discretizing the domain Ω into m non-overlapping finite elements that conform to the fracture geometry, such that

$$\Omega \cong \Omega^h \equiv \bigcup_{e=1}^{m}\Omega_e \quad [14]$$

where Ω_e are triangular elements in this work. For each element Ω_e, the displacement field is approximated as a linear function, which is expressed in terms of the displaced values at the three vertices such that

$$\mathbf{u} = \begin{Bmatrix} u \\ v \end{Bmatrix} \cong \begin{Bmatrix} N_i u_i \\ N_i v_i \end{Bmatrix} = \mathbf{N}\mathbf{u}_h^e \quad [15]$$

By substituting Eq. [15] into Eq. [11], the discretized system can be written as

$$\mathbf{K}\mathbf{u}_h = \mathbf{F} \quad [16]$$

where **K** and **F** are the global stiffness matrix and global load vector, respectively. For elements that are not adjacent to a fracture surface, they are obtained by assembly from each element and expressed as follows

$$\mathbf{K} = \sum_{e=1}^{m} \mathbf{K}_e = \sum_{e=1}^{m} \int_{\Omega_e} \mathbf{B}^{\mathrm{T}}\mathbf{D}\mathbf{B}\mathrm{d}\Omega \quad [17]$$

$$\mathbf{F} = \sum_{e=1}^{m} \mathbf{F}_e + \mathbf{F}_t = \sum_{e=1}^{m} \int_{\Omega_e} \mathbf{N}^{\mathrm{T}}\mathbf{b}\mathrm{d}\Omega + \int_{\Gamma_t} \mathbf{N}^{\mathrm{T}}\bar{\mathbf{t}}\mathrm{d}\Gamma \quad [18]$$

where **B** is gradient matrix defined as

$$\mathbf{B} = \mathbf{L}\mathbf{N} \quad [19]$$

3.2 Adaptive remeshing technique

The accuracy of the FEM simulation depends on the quality of the mesh that is affected by the geometric discretization errors and the gradients of solution within individual elements. For the fracture propagation problem in a linearly elastic medium, the stress is singular at the fracture tip and drops quickly away from the fracture tip. In this work, we consider a combination of two techniques to give a reasonable representation of this behaviour in the vicinity of the crack tip: First mesh refinement based on an error estimation to improve the accuracy of FEM, and second, remeshing around crack tip domain by the collapsed quarter point elements to represent the tip singularity, and thus improve the accuracy in computation of the stress intensity factors and to easily extend crack in this domain. In addition, a third ingredient of our approach is Laplacian smoothing to improve the quality of the mesh.

4. NUMERICAL INVESTIGATION

In this section, three numerical examples are investigated. The first and second intended for validation purposes, while the last one is designed for EGS applications: To validate the proposed model, the propagation paths of wing cracks in domains with a single and two pre-existing fractures under uniaxial compression are considered and compared with experimental observations. After that, this model is extended to a more complex problem where the surfaces of one fracture slip and creates wing cracks that connects to other fractures.

4.1 Validation

The compression test of a rock specimen with a single pre-existing fracture as shown in Figure 3 is adapted. The fracture is inclined located at 45˚ to the horizontal direction at center of the specimen. The material parameters are Young's modulus E = 36.2 GPa, Poisson's ratio ν = 0.21, fracture toughness K_{IC} = 6.5 MPa·m$^{1/2}$. The size of specimen is 102 × 102 mm^2 and of the length of fracture is 20.32 mm. Boundary conditions on the specimen are indicated in Figure 3; on the existing fracture, a no-friction condition is assigned in the tangential direction.

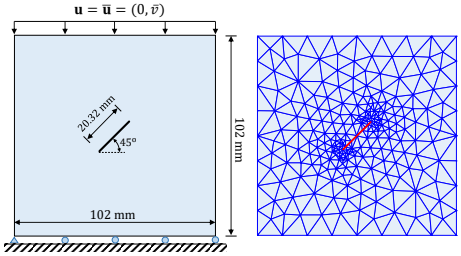

Figure 3: Geometry of specimen with a single pre-existing fracture.

The propagation paths of two wing cracks originated from tips of the pre-existing fracture is shown in Figure 4. The paths are curvilinear and tend to migrate of around 70 degrees and gradually turn in the loading direction. The trajectories of the wing cracks obtained in this work is similar to the observation from the experiments reported in (Ashby and Hallam 1986; Haeri et al. 2014; Ingraffea and Manu 1980; Lee and Jeon 2011; Shen et al. 1995).

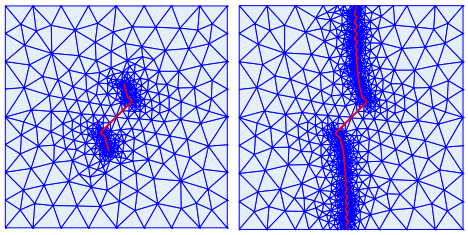

Figure 4: The trajectories of wing cracks from a single pre-existing crack.

As a second test, consider the connection of double pre-existing fractures in a specimen under the uniaxial compression. The specimen shown in Figure 5 is made from gypsum with the material parameters are as follows: Young's modulus E = 5.96 GPa, Poisson's ratio ν = 0.24, fracture toughness K_{IC} = 0.1778 MPa·m$^{1/2}$. The size of the specimen is 152.4 × 76.2 mm^2. There are two pre-existing fractures are in the specimen and inclined at 45˚ to the horizontal direction. Boundary conditions on the specimen are indicated in Figure 5; again, no-friction conditions are assigned in the tangential direction of the pre-existing fractures.

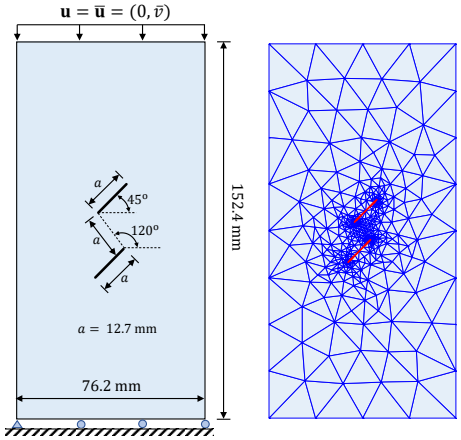

Figure 5: Geometry of a specimen with two pre-existing fractures.

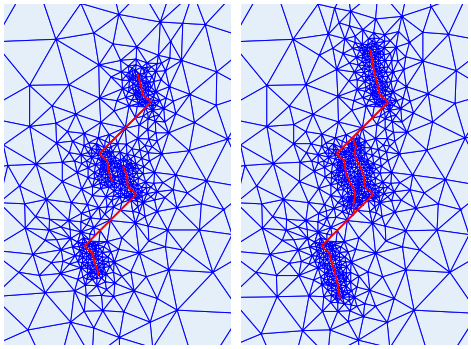

Figure 6: The trajectories of wing cracks from double pre-existing cracks

The fracture propagation process is shown in Figure 6. The wings cracks initiate at the two tips of each pre-existing fracture and propagate in opposite directions. Then the wing crack originating from one fracture links to other fractures to extend the failure. The trajectories of the wing cracks are curvilinear and similar to that observed previously in the compression test of the rock (Park and Bobet 2009; Shen et al. 1995).

The agreement with experimental observations in the above examples shows that the mathematical model proposed in this work is valid for the fracture propagation in type of wing cracks. Compared to a finely resolved static grid, the ARM technique significantly reduces the computational cost, while preserving accuracy of the predicted fracture trajectory. Motivated by this confirmation, the procedure is extended to investigate a typical problem in EGS that wing cracks emerge and propagate not by compression stress but by sliding in opposite direction of interfaces of a pre-existing fracture. This extension is presented in the next example.

4.2 EGS application

This example extends the proposed model to the problem of enhanced permeability in EGS. The example setup and geometry are shown in Figure 7, in which three natural horizontal fractures exist initially in a specimen. The size and length of the specimen and fractures are, respectively, 3000×2000 mm^2 and 500 mm. The material parameters are the same as for first example. A measurable slip is imposed on the middle fracture, mimicking the slip due to water injection in fracture shear stimulation. Instead of compressive stress, the slip is considered the cause of wing cracks in EGS.

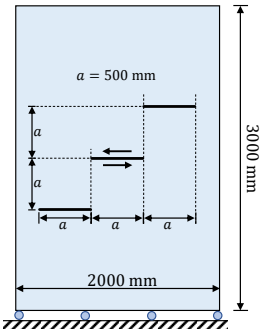

Figure 7: Geometry of specimens with three pre-existing fractures.

The initiation and propagation of wing cracks are shown in Figure 8. When a pre-existing fracture experience a jump in tangential displacements, wing cracks may emerge at its tips, tend to migrate of around 70 degrees and gradually turn in the almost perpendicular directions. If the tectonic stress stored in this fracture is large enough, wing cracks propagate away and link to nearby fractures to form connected flow pathways. Then water flows to these fractures and the process of developing wing cracks is repeated to enhance permeability in EGS.

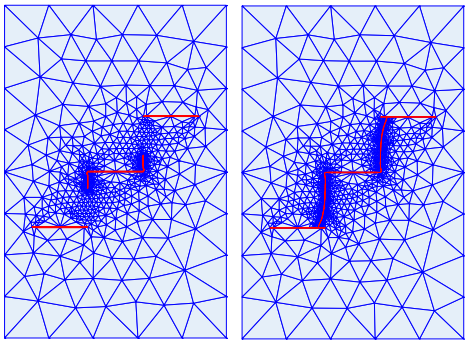

Figure 8: The trajectories of wing cracks caused by shear slip at interfaces a pre-existing crack

The obtained results in this example show that, the mechanism of wing cracks caused by the shear slip in the interfaces of a pre-existing fracture is predictable.

This is important for improving the performance of geothermal systems which are significantly influenced by permeability.

5. CONCLUSIONS

The simple mathematical model and the ARM technique are presented in this work to simulate the wing cracks initiation and propagation in rock material. The model is established based on the linear elasticity theory, in combination with MTS criterion. An ARM technique is developed based on a simple error estimator, deleted-replaced process and Laplacian smoothing. Three examples are considered. The first and second examples are for validation purposes, while the last one is designed to investigate the mechanism of wing cracks in EGS. The obtained results in this work show the accuracy and effectiveness of the proposed model and procedure in the prediction of wing cracks propagation caused by both compression and shear slip.

REFERENCES

Abdollahipour, A. and Fatehi Marji, M.: Analyses of Inclined Cracks Neighboring Two Iso-Path Cracks in Rock-Like Specimens Under Compression, *Geotechnical and Geological Engineering*, **35**, (2016), 169–181.

Ashby, M. F. and Hallam, S. D.: The failure of brittle solids containing small cracks under compressive stress states, *Acta Metallurgica*, **34**, (1986), 497–510.

Barsoum, R. S.: On the use of isoparametric finite elements in linear fracture mechanics, *International Journal for Numerical Methods in Engineering*, **10**, (1976), 25–37.

Bobet, A. and Einstein, H. H.: Fracture coalescence in rock-type materials under uniaxial and biaxial compression, *International Journal of Rock Mechanics and Mining Sciences*, **35**, (1998), 863–888.

Bryant, E. C. and Sun, W.: A mixed-mode phase field fracture model in anisotropic rocks with consistent kinematics, *Computer Methods in Applied Mechanics and Engineering*, **342**, (2018), 561–584.

Cheng, Q., Wang, X. and Ghassemi, A.: Numerical simulation of reservoir stimulation with reference to the Newberry EGS, *Geothermics*, **77**, (2019), 327–343.

Erdogan, F. and Sih, G. C.: On the Crack Extension in Plates Under Plane Loading and Transverse Shear, *Journal of Basic Engineering*, **85**, (1963), 519–525.

Fatehi Marji, M.: Numerical analysis of quasi-static crack branching in brittle solids by a modified displacement discontinuity method, *International Journal of Solids and Structures*, **51**, (2014), 1716–1736.

Gonçalves da Silva, B. and Einstein, H.: Modeling of crack initiation, propagation and coalescence in rocks, *International Journal of Fracture*, **182**, (2013), 167–186.

Haeri, H., Shahriar, K., Fatehi Marji, M. and Moarefvand, P.: A coupled numerical–experimental study of the breakage process of brittle substances, *Arabian Journal of Geosciences*, **8**, (2013), 809–825.

Haeri, H., Shahriar, K., Fatehi Marji, M. and Moarefvand, P.: Experimental and numerical study of crack propagation and coalescence in pre-cracked rock-like disks, *International Journal of Rock Mechanics and Mining Sciences*, **67**, (2014), 20–28.

Henshell, R. D. and Shaw, K. G.: Crack tip finite elements are unnecessary, *International Journal for Numerical Methods in Engineering*, **9**, (1975), 495–507.

Horii, H. and Nemat-Nasser, S.: Compression-induced microcrack growth in brittle solids: Axial splitting and shear failure, *Journal of Geophysical Research: Solid Earth*, **90**, (1985), 3105–3125.

Hussain, M. A., Pu, S. L. and Underwood, J.: Strain Energy Release Rate for a Crack Under Combined Mode I and Mode II, *Proceedings of the National Symposium on Fracture Mechanics 1973*, Washington, USA, (1973), paper #001, 2-28.

Ingraffea, A. R. and Heuze, F. E.: Finite element models for rock fracture mechanics, *International Journal for Numerical and Analytical Methods in Geomechanics*, **4**, (1980), 25–43.

Ingraffea, A. R. and Manu, C.: Stress-intensity factor computation in three dimensions with quarter-point elements, *International Journal for Numerical Methods in Engineering*, **15**, (1980), 1427–1445.

Janeiro, R. P. and Einstein, H. H.: Experimental study of the cracking behavior of specimens containing inclusions (under uniaxial compression), *International Journal of Fracture*, **164**, (2010), 83–102.

Jung, R.: EGS — Goodbye or Back to the Future, in: Effective and Sustainable Hydraulic Fracturing, Rob, J. (Ed.) 95–121, *INTECH*, (2013).

Kamali, A. and Ghassemi, A.: Analysis of Natural Fracture Shear Slip and Propagation in Response to Injection, *Proceeding of the 41st Workshop on Geothermal Reservoir Engineering 2016*, California, USA, (2016), paper #050, 584-593.

Khoei, A. R., Azadi, H. and Moslemi, H.: Modeling of

crack propagation via an automatic adaptive mesh refinement based on modified superconvergent patch recovery technique, *Engineering Fracture Mechanics*, **10**, (2008), 2921–2945.

Lee, H. and Jeon, S.: An experimental and numerical study of fracture coalescence in pre-cracked specimens under uniaxial compression, *International Journal of Solids and Structures*, **48**, (2011), 979–999.

Lehner, F. and Kachanov, M.: On modelling of 'winged" cracks forming under compression, *International Journal of Fracture*, **77**, (1996), 69–75.

Li, H. and Wong, L.: Influence of flaw inclination angle and loading condition on crack initiation and propagation, *International Journal of Solids and Structures*, **49**, (2012), 2482–2499.

Li, Y.-P., Chen, L.-Z. and Wang, Y.-H.: Experimental research on pre-cracked marble under compression, *International Journal of Solids and Structures*, **42**, (2005), 2505–2516.

Lin, W., Yeh, E.-C., Hung, J.-H., Haimson, B. and Hirono, T.: Localized rotation of principal stress around faults and fractures determined from borehole breakouts in hole B of the Taiwan Chelungpu-fault Drilling Project (TCDP), *Tectonophysics*, **482**, (2010), 82–91.

Moran, B. and Shih, C. F.: A general treatment of crack tip contour integrals, *International Journal of Fracture*, **35**, (1987), 295–310.

Norbeck, J. H., McClure, M. W. and Horne, R. N.: Field observations at the Fenton Hill enhanced geothermal system test site support mixed-mechanism stimulation, *Geothermics*, **74**, (2018), 135–149.

Park, C. H. and Bobet, A.: Crack coalescence in specimens with open and closed flaws: A comparison, *International Journal of Rock Mechanics and Mining Sciences*, **46**, (2009), 819–829.

Park, C. H. and Bobet, A.: Crack initiation, propagation and coalescence from frictional flaws in uniaxial compression, *Engineering Fracture Mechanics*, **77**, (2010), 2727–2748.

Parks, D. M.: A stiffness derivative finite element technique for determination of crack tip stress intensity factors, *International Journal of Fracture*, **10**, (1974), 487–502.

Phongthanapanich, S. and Dechaumphai, P.: Adaptive Delaunay triangulation with object-oriented programming for crack propagation analysis, *Finite Elements in Analysis and Design*, **40**, (2004), 1753–1771.

Sharafisafa, M. and Nazem, M.: Application of the distinct element method and the extended finite element method in modelling cracks and coalescence in brittle materials, *Computational Materials Science*, **91**, (2014), 102–121.

Shen, B., Stephansson, O., Einstein, H. H. and Ghahreman, B.: Coalescence of fractures under shear stresses in experiments, *Journal of Geophysical Research: Solid Earth*, **100**, (1995), 5975–5990.

Sih, G. C.: Strain-energy-density factor applied to mixed mode crack problems, *International Journal of Fracture*, **10**, (1974), 305–321.

Sivakumar, G. and Maji, V.: Simulation of crack propagation in rocks by XFEM, *Proceedings of the conference on Recent Advances in Rock Engineering 2016*, Karnataka, India, (2016), paper #046.

Wong, L. N. Y. and Einstein, H. H.: Systematic evaluation of cracking behavior in specimens containing single flaws under uniaxial compression, *International Journal of Rock Mechanics and Mining Sciences*, **46**, (2009), 239–249.

Xie, Y., Cao, P., Liu, J. and Dong, L.: Influence of crack surface friction on crack initiation and propagation: A numerical investigation based on extended finite element method, *Computers and Geotechnics*, **74**, (2016), 1–14.

Xu, J., Zheng, Z., Xiao, X. and Li, Z.: Crack propagation and coalescence due to dual non-penetrating surface flaws and their effect on the strength of rock-like material, *Journal of Geophysics and Engineering*, **15**, (2018), 938–951.

Yang, S. Q.: Crack coalescence behavior of brittle sandstone samples containing two coplanar fissures in the process of deformation failure, *Engineering Fracture Mechanics*, **78**, (2011), 3059–3081.

Yang, S. Q., Dai, Y. H., Han, L. and Q. Jin, Z.: Experimental study on mechanical behavior of brittle marble samples containing different flaws under uniaxial compression, *Engineering Fracture Mechanics*, **76**, (2009), 1833–1845.

Zhang, X., Sloan, S., Vignes, C. and Sheng, D.: A modification of the phase-field model for mixed mode crack propagation in rock-like materials, *Computer Methods in Applied Mechanics and Engineering*, **322**, (2017), 123–136.

Acknowledgements

This work was funded by the ERiS project, grant #267909, Research Council of Norway.

Paper B

Numerical modeling of wing crack propagation accounting for fracture contact mechanics

Hau Trung Dang, Eirik Keilegavlen, Inga Berre

International Journal of Solids and Structures. Vol. 204–205: 233-247. 2020.

DOI: 10.1016/j.ijsolstr.2020.08.017

https://www.sciencedirect.com/science/article/pii/S0020768320303152

International Journal of Solids and Structures 204–205 (2020) 233–247

Contents lists available at ScienceDirect

International Journal of Solids and Structures

journal homepage: www.elsevier.com/locate/ijsolstr

Numerical modeling of wing crack propagation accounting for fracture contact mechanics

Hau Dang-Trung *, Eirik Keilegavlen, Inga Berre

Department of Mathematics, University of Bergen, Bergen, Norway

ARTICLE INFO

Article history:
Received 2 January 2020
Received in revised form 1 August 2020
Accepted 21 August 2020
Available online 6 September 2020

Keywords:
Fracture propagation
Wing crack development
Shear slip
Adaptive remeshing
Linear elastic fracture mechanics
Contact mechanics

ABSTRACT

As a consequence of shearing, wing cracks can emerge from pre-existing fractures. The process involves the interaction of sliding of the existing fracture surfaces and the tensile material failure that creates wing cracks. This work devises a numerical model to investigate how wing cracks emerge, propagate and connect pre-existing fractures under shear processes. A mathematical and numerical model for wing crack propagation based on linear elastic fracture mechanics that also accounts for fracture contact mechanics is presented. Computational efficiency is ensured by an adaptive remeshing technique. The numerical model is verified and validated through a comparison of the analytical and experimental results. Additional numerical examples illustrate the performance of the method for complex test cases where wing-cracks develop for multiple pre-existing and interacting fractures.

1. Introduction

Wing cracks can develop from a pre-existing fracture when the fracture is subjected to shear processes. This occurs for many applications where fractured media are subjected to anisotropic stress regimes. For example, in fractured subsurface systems, fractures will slip if shear forces overcome the cohesion and frictional strength of the contact between the fracture surfaces. This can occur due to natural changes in tectonic stresses, but the process can also be induced by fluid injection, such as in situations of geothermal reservoirs. In the latter case, elevated pressures reduce the effective normal stress on the fracture, ultimately causing slip if the reduction in the normal stress is sufficient for the shear forces to overcome the cohesion and frictional resistance of the fracture. The slip of the fracture surfaces in opposite directions can cause the fracture to propagate in the form of wing cracks, possibly creating enhanced reservoir connectivity (Cheng et al., 2019; Jung, 2013; McClure and Horne, 2014; Norbeck et al., 2018). Understanding this mechanism is, thus, crucial in the simulation of fractured subsurface formations.

Many experimental studies have been published that consider the formation, growth and connection of wing cracks caused by external compressive loading in specimens made of rock or rock-like materials (Haeri et al., 2014a, 2014b; Horii and Nemat-Nasser, 1985; Ingraffea and Manu, 1980). In these experiments, if the pre-existing fracture is not perpendicular to the external load, wing cracks emerge at the tip and tend to align with the direction of the maximum compressive stress. The same conclusion is drawn from mathematical modeling. Based on the finite element method (FEM), Ingraffea and Heuze (1980) predicted the propagation of wing cracks in rock structures by using three different criteria based on stress, energy and strain. Primary crack trajectories predicted by the stress and energy criteria are in good agreement with the observed trajectories. Based on the phase-field model (Bryant and Sun, 2018) and a modified phase-field model (Zhang et al., 2017), wing crack propagation was modeled using energy criteria that divided the active energy density into distinct parts corresponding to different crack modes (mode I and mode II). Sharafisafa and Nazem (2014) used the vector level set with both the discrete element method (DEM) and the extended finite element method (XFEM) to model the wing crack propagation and coalescence in fractured rock masses. Among these methods and failure criteria, the FEM is the simplest method in implementation and the stress criterion is one of the most extensively used and least complicated. Specifically, the combination of FEM with the stress criterion (the maximum tangential stress) for modeling of wing cracks has been shown to produce simulation in good agreement with observed crack trajectories (Gonçalves da Silva and Einstein, 2013; Ingraffea and Heuze, 1980).

* Corresponding author at: Department of Mathematics, University of Bergen, Postboks 7803, 5020 Bergen, Norway.
E-mail addresses: Hau.Dang@uib.no, dtrhau@gmail.com (H. Dang-Trung).

https://doi.org/10.1016/j.ijsolstr.2020.08.017
0020-7683/

While wing cracks develop as tensile fractures, the pre-existing fractures that wing cracks emerge from may be either open or in contact. This necessitates the inclusion of fracture contact mechanics in the wing crack models (Hüeber et al., 2008; Oden and Pires, 1983). There are several ways to formulate the contact mechanics corresponding to the different types of discretizations. For example, Kim and Duarte (2015) simulated the mode I propagation of cohesive fractures in 3D by the cohesive law using a generalized finite element method. Because of the difference of material behaviour in the vicinity of propagating crack fronts compared to the rest of the domain, this approach requires updates of global–local enrichments during the analysis, which increases the computational cost. Hesch et al. (2016) formulated the contact mechanics by Coulomb's friction law and Karush Kuhn-Tucker (KKT) conditions applied to a phase-field approach within the context of isogeometric analysis. A fourth order approach for the crack-density functional was used to ensure sufficient accuracy of the chosen phase-field approach. This leads to a request of at least C^1 continuity within the domain. Also using Coulomb's friction law and the KKT conditions, Nejati et al. (2016) modeled the internal contact in fractured media by a sophisticated algorithm based on isoparametric integration-point-to-integration-point discretization of the contact contribution to enforce the contact constraint accurately over the crack surfaces. Based on the semianalytical displacement discontinuity method, Kamali and Ghassemi (2018) developed a simulation model in which the closed natural fractures were represented by so-called contact displacement discontinuity elements (Asgian, 1988), approximating the contact mechanics condition. However, the approach has limitations in dealing with the interaction between multiple fractures due to inherent limitations of the semianalytical displacement discontinuity method.

The FEM model for elasticity can be derived by using one of the following widely used methods: the weighted-residual method based on the linear momentum balance or minimization of an energy function (Liu and Quek, 2003). By using the energy principle, the contact should be considered as an inequality constraint of the optimization formulation of the potential energy. This means that the potential energy is minimized while satisfying a contact constraint assumed to be a nonpenetration condition between the surfaces of the fracture. The inequality constraint can be solved by some methods, such as the active-set, Frank-Wolfe, penalty or barrier methods (Hüeber et al., 2008; Hüeber and Wohlmuth, 2005).

An inherent problem in the simulation of fracture propagation is the disparate length scales. While the simulation domain can be quite large, the fracturing processes occur on a scale that is several orders of magnitude smaller. Moreover, most numerical methods for fracture propagation are dependent on resolving the fracture in a grid; however, the fracture path is not known a priori. A possible remedy for both of these issues is to apply adaptive remeshing (ARM) techniques to refine and adjust the mesh around an advancing fracture path.

This paper presents a mathematical model and corresponding numerical solution approach to simulate the development of wing cracks while accounting for fracture contact mechanics. First, in Section 2, the mathematical model for wing crack propagation is formulated based on the linear elasticity theory, in combination with the criteria for a mixed-mode fracture propagation. Fracture surfaces are allowed to be in contact or fully open, modeled by contact mechanics formed by the KKT conditions. Section 3 presents the numerical solution approach. The governing equations are discretized using a finite element method with collapsed quarter-point elements at the fracture tips. This is combined with an adaptive remeshing technique based on error estimates and Laplacian smoothing. The contact mechanics are implemented by using an active set method. Section 4 presents several numerical test cases. The obtained results are compared with both the analytical and experimental data to verify, validate and show the accuracy of the proposed model and procedure. Finally, more complex test cases where wing cracks develop for multiple pre-existing and interacting fractures show the capability of the proposed approach in modeling the development of wing cracks under shear processes.

2. Governing equations

A mathematical model for wing crack propagation based on linear elastic fracture mechanics is presented in the following section. Emphasis is placed on the conditions on the boundaries of existing and newly formed fracture paths. We also describe the criterion used to decide when, where and how far a fracture will propagate.

2.1. Elasticity and contact mechanics

Consider a domain $\Omega \subset \mathbb{R}^2$ with an outward unit normal vector $\mathbf{n}$ on its boundary and a pre-existing fracture with boundaries denoted by $\Gamma_C^{\pm}$ as shown in Fig. 1. The Dirichlet and Neumann conditions are applied on the boundary. Ignoring, for the moment, the internal boundary conditions on the fracture, the governing equations for a linear elastic body can be expressed as (Jaeger et al., 2007)

$$\begin{cases} \nabla \cdot \boldsymbol{\sigma} + \mathbf{b} = 0 & \text{in } \Omega \quad \text{Equilibrium eq.} \\ \boldsymbol{\sigma} = \mathbf{C} : \boldsymbol{\varepsilon} & \text{in } \Omega \quad \text{Constitutive eq.} \\ \boldsymbol{\varepsilon} = \frac{1}{2}(\nabla \mathbf{u} + \nabla \mathbf{u}^{\mathrm{T}}) & \text{in } \Omega \quad \text{Kinematic eq.} \\ \mathbf{u} = \mathbf{u}_0 & \text{on } \Gamma_D \quad \text{Dirichlet BC} \\ \boldsymbol{\sigma} \cdot \mathbf{n} = \mathbf{f} & \text{on } \Gamma_N \quad \text{Neumann BC} \end{cases} \tag{1}$$

where, $\boldsymbol{\sigma}$, $\boldsymbol{\varepsilon}$ and $\mathbf{u} = \{u, v\}^{\mathrm{T}}$ are the Cauchy stress tensor, the symmetric infinitesimal strain tensor and the displacement field, respectively; $\mathbf{C}$ is the fourth-order elasticity (Hooke's) tensor defined by the Young's modulus, E, and Poisson's ratio, ν; $\mathbf{b}$ is the body force; and $\mathbf{u}_0$ and $\mathbf{f}$ are the prescribed displacement along the Dirichlet boundary and the applied traction along the Neumann boundary, respectively.

To formulate the contact mechanics at the internal boundary, the fracture's boundary is divided into a positive side Γ_C^+ and a negative side Γ_C^-. Let $\mathbf{n}(\mathbf{x})$ denote the normal vector initiating from $\mathbf{x}$ at side Γ_C^+ to side Γ_C^-. The initial gap between the two fracture sides is $g(\mathbf{x}) \geqslant 0$. The jump in the normal direction of the fracture, $[\mathbf{u}(\mathbf{x})]_{\mathbf{n}}$, and the surface traction in the normal direction, $f_{\mathbf{n}}(\mathbf{x})$, are given by

$$[\mathbf{u}(\mathbf{x})]_{\mathbf{n}} = [\mathbf{u}(\mathbf{x})] \cdot \mathbf{n}(\mathbf{x}), \quad f_{\mathbf{n}}(\mathbf{x}) = \mathbf{f}(\mathbf{x}) \cdot \mathbf{n}(\mathbf{x}), \quad \mathbf{x} \in \Gamma_C^+ \tag{2}$$

where $\mathbf{f}(\mathbf{x}) = \boldsymbol{\sigma}(\mathbf{x}) \cdot \mathbf{n}(\mathbf{x})$ is the traction at the fracture's boundary, which vanishes in the case of an open fracture.

A nonpenetration condition is enforced in the normal direction of the fracture segments. This condition is governed in the form of Karush-Kuhn-Tucker (KKT) condition for the normal displacement jump and the normal surface traction (Wohlmuth, 2011), which reads

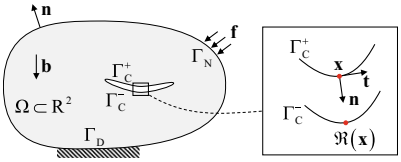

Fig. 1. An elastic body containing a pre-existing fracture.

$$[\mathbf{u}(\mathbf{x})]_{\mathbf{n}} - g(\mathbf{x}) \leqslant 0, \quad f_{\mathbf{n}}(\mathbf{x}) \leqslant 0, \quad f_{\mathbf{n}}(\mathbf{x})\left([\mathbf{u}(\mathbf{x})]_{\mathbf{n}} - g(\mathbf{x})\right) = 0, \quad \mathbf{x} \in \Gamma_C^+ \tag{3}$$

If Γ_C^+ and Γ_C^- are in contact, by Newton's third law, the surface tractions on both sides are equal but in opposite directions; that is

$$\mathbf{f}(\mathbf{x}) = -\mathbf{f}(\Re(\mathbf{x})), \quad \mathbf{x} \in \Gamma_C^+ \tag{4}$$

in which $\Re : \Gamma_C^+ \to \Gamma_C^-$ is a mapping that projects a point from side Γ_C^+ onto side Γ_C^- in the normal direction. The displacement jump, $[\mathbf{u}(\mathbf{x})]$, is then defined by

$$[\mathbf{u}(\mathbf{x})] = \mathbf{u}(\mathbf{x}) - \mathbf{u}(\Re(\mathbf{x})), \quad \mathbf{x} \in \Gamma_C^+ \tag{5}$$

For the tangential direction of Γ_C, two types of conditions are considered: Either the fracture surfaces are modeled as frictionless, or the displacement jump in the tangential direction is specified. For frictionless fracture surfaces, the tangential traction is zero at Γ_C; i.e.

$$\boldsymbol{\sigma}(\mathbf{x}) \cdot \mathbf{t}(\mathbf{x}) = \boldsymbol{\sigma}(\Re(\mathbf{x})) \cdot \mathbf{t}(\Re(\mathbf{x})) = 0, \quad \mathbf{x} \in \Gamma_C^+ \tag{6}$$

where $\mathbf{t}(\mathbf{x})$ is the tangential vector initiating from $\mathbf{x}$ at side Γ_C^+. The assumption of zero friction leads to an exaggeration of the slip but is acceptable herein, as the trajectory of the fracture is the primary quantity of interest. For the friction-free case, the deformation of the elastic medium and the fractures contained within are driven by the body force, external boundary conditions on Γ_D and Γ_N, or displacements on other fractures.

The second type of condition is a specified displacement jump in the tangential direction of the fracture, i.e.

$$[\mathbf{u}(\mathbf{x})]_{\mathbf{t}} = [\mathbf{u}(\mathbf{x}) - \mathbf{u}(\Re(\mathbf{x}))] \cdot \mathbf{t}(\mathbf{x}) = u_0 \tag{7}$$

where the total slip at Γ_C, u_0, is considered as known. This type of condition is relevant to mimic the slip along an existing fracture, which in applications, may be triggered by effects not considered in the present model.

The wing cracks emerging due to the shear force on existing fractures are tensile cracks (Bobet and Einstein, 1998; Wong and Einstein, 2009). This means that their surfaces are in not contact and both normal and tangential tractions at the corresponding fracture faces are zero; i.e.

$$\boldsymbol{\sigma} \cdot \mathbf{n} = \boldsymbol{\sigma} \cdot \mathbf{t} = 0 \tag{8}$$

The wing cracks are not present in the computational domain at the start of the simulations. Indeed, the computation of the point of failure and the paths of the wing crack that develop are the main challenges that are addressed in this work.

2.2. Failure and propagation

The wing crack growth processes are governed by a mixed-mode fracture criterion. From the mathematical model for elastic deformation, the stress at an arbitrary point can be directly calculated for a certain problem. In this work, we chose to adapt the fracture criterion based on the maximum tangential stress (MTS) (Erdogan and Sih, 1963), which is simple and sufficiently accurate (Gonçalves da Silva and Einstein, 2013; Ingraffea and Heuze, 1980), to predict the initiation and propagation angle of wing cracks. This criterion states that a crack grows when the maximum average tangential stress in the fracture process zone ahead of the crack tip reaches a critical value. Moreover, the crack growth direction coincides with the direction of the maximum average tangential stress along a constant radius around the crack tip. In polar coordinates (r, θ) with the origin at the crack tip, the tangential stress for a mixed-mode crack has the following form (Erdogan and Sih, 1963)

$$\sigma_\theta(r,\theta) = \frac{1}{\sqrt{2\pi r}}\left(K_{\mathrm{I}}\cos^3\frac{\theta}{2} - \frac{3}{2}K_{\mathrm{II}}\cos\frac{\theta}{2}\sin\theta\right) \tag{9}$$

where r is the distance from the tip. K_{I} and K_{II} are the stress intensity factors (SIFs), which are measures for the intensity of stresses close to the crack tip. The wing crack emerges if the tangential stress reaches a critical value, i.e.,

$$\sigma_{\theta_0}\sqrt{2\pi r} = K_{\mathrm{I}}\cos^3\frac{\theta_0}{2} - \frac{3}{2}K_{\mathrm{II}}\cos\frac{\theta_0}{2}\sin\theta_0 = K_{\mathrm{IC}} \tag{10}$$

where K_{IC} is the material toughness and θ_0 is the crack initiation angle with respect to the original crack plane. θ_0 is obtained by solving $\partial\sigma_\theta/\partial\theta = 0$ for θ and combining the result with the sufficient condition $\partial^2\sigma_\theta/\partial\theta^2 < 0$ such that

$$\theta_0 = 2\tan^{-1}\left(\frac{1}{4}\mu \pm \frac{1}{4}\sqrt{\mu^2+8}\right), \quad \mu = K_{\mathrm{I}}/K_{\mathrm{II}} \tag{11}$$

$$K_{\mathrm{II}}\left(\sin\frac{\theta_0}{2} + 9\sin\frac{3\theta_0}{2}\right) < K_{\mathrm{I}}\left(\cos\frac{\theta_0}{2} + 3\cos\frac{3\theta_0}{2}\right) \tag{12}$$

When the wing crack emerges, i.e., the criterion shown in Eq. (10) is satisfied, the increment of each fracture needs to be determined. For a single crack propagation, the increment is defined by a fixed distance such as the crack tip rosette radius h. In the case where more than one crack grows simultaneously, the tips with the highest energy in the fracture set advance significantly further than the others (Paluszny and Matthäi, 2009). The increment for each tip is defined by the Paris-type law (Paris and Erdogan, 1963; Renshaw and Pollard, 1994)

$$L_{\mathrm{adv}}^i = L_{\max}\left(\frac{G_i}{\max(G_i)}\right)^\alpha \tag{13}$$

where L_{adv}^i and G_i are the propagation length and the energy release rate for the ith propagation crack, respectively, $L_{\max}$ is the maximum length increase at any propagation step, and the exponent α is a numerical parameter, which is set to 0.35 in this work (Renshaw and Pollard, 1994). For a general fracture in a two-dimensional domain, the energy release around the fracture tip is given by

$$G = \frac{(1+\nu)(1+k)}{4E}\left(k_{\mathrm{I}}^2 + k_{\mathrm{II}}^2\right) \tag{14}$$

here, k_{I} and k_{II} are the local mode I and mode II stress intensity factors at the tip obtained by summing the normal and shear stresses (Anderson, 2017), respectively

$$\begin{aligned} k_{\mathrm{I}} &= \sigma_{yy}\sqrt{2\pi h} \\ &= \frac{1}{4}\left[3\cos\left(\frac{\theta_0}{2}\right) + \cos\left(\frac{3\theta_0}{2}\right)\right]K_{\mathrm{I}} \\ &\quad - \frac{1}{4}\left[3\sin\left(\frac{\theta_0}{2}\right) - 3\sin\left(\frac{3\theta_0}{2}\right)\right]K_{\mathrm{II}} \end{aligned} \tag{15}$$

$$\begin{aligned} k_{\mathrm{II}} &= \tau_{xy}\sqrt{2\pi h} \\ &= \frac{1}{4}\left[\sin\left(\frac{\theta_0}{2}\right) + \sin\left(\frac{3\theta_0}{2}\right)\right]K_{\mathrm{I}} \\ &\quad + \frac{1}{4}\left[\cos\left(\frac{\theta_0}{2}\right) + 3\cos\left(\frac{3\theta_0}{2}\right)\right]K_{\mathrm{II}} \end{aligned} \tag{16}$$

3. Discretization

This section presents the finite element discretization of the governing equations presented in Section 2, together with an adaptive remeshing technique. The propagation of wing cracks is complicated, and their trajectories are difficult to achieve by analytical

or semianalytical approaches, particularly when multiple fractures interact. In this case, numerical solutions by means of the finite element method (FEM) are a common approach. The finite element formulation is based on the weak formulation established from the governing equation and states: Find $\mathbf{u} \in V_S$ such that $\forall \mathbf{v} \in V_T$ (Zienkiewicz et al., 2005)

$$\int_\Omega \mathbf{u}^T \mathbf{L}^T \mathbf{D} \mathbf{L} \mathbf{v} d\Omega - \int_{\Gamma_c} \boldsymbol{\sigma} \cdot \mathbf{n} \mathbf{v} d\Gamma = \int_\Omega \mathbf{b} \mathbf{v} d\Omega + \int_{\Gamma_N} \bar{\mathbf{f}}\, \mathbf{v} d\Gamma \tag{17}$$

where V_T and V_S are the test space and the solution space satisfying the inhomogeneous Dirichlet boundary conditions (so-called essential boundary conditions), respectively. V_T and V_S are defined by

$$V_T := \left\{ \mathbf{v} \in H_0^1(\Omega),\ \ \mathbf{v}|_{\Gamma_D} = 0 \right\},$$
$$V_S := \left\{ \mathbf{v} \in H^1(\Omega),\ \ \mathbf{v}|_{\Gamma_D} = \mathbf{u}_0 \right\} \tag{18}$$

where $H^1(\Omega)$ is the Sobolev space of functions that are square integrable and have a square integrable first derivative. In Eq. (17), $\mathbf{L}$ is the differential operator, and $\mathbf{D}$ is the material matrix modified from $\mathbf{C}$ and defined by

$$\mathbf{L} = \begin{bmatrix} \partial/\partial x & 0 & \partial/\partial y \\ 0 & \partial/\partial y & \partial/\partial x \end{bmatrix}^T \tag{19}$$

$$\mathbf{D} = \frac{E}{1-\nu^2} \begin{bmatrix} 1 & \nu & 0 \\ \nu & 1 & 0 \\ 0 & 0 & \frac{1}{2}(1-\nu) \end{bmatrix}, \text{ for plane stress} \tag{20}$$

$$\mathbf{D} = \frac{E}{(1+\nu)(1-2\nu)} \begin{bmatrix} 1-\nu & \nu & 0 \\ \nu & 1-\nu & 0 \\ 0 & 0 & \frac{1}{2}(1-2\nu) \end{bmatrix}, \text{ for plane strain} \tag{21}$$

3.1. Deformation and contact mechanics

The approximate solution of Eq. (1), denoted by $\mathbf{u}^h$, can be evaluated by using a subset of the allowable function space $V_h \subset V_S$ composed of piecewise polynomial functions. This requires discretizing the domain Ω into m nonoverlapping finite elements that conform to the fracture geometry, such that

$$\Omega \cong \Omega^h \equiv \bigcup_{e=1}^m \Omega_e \tag{22}$$

In this work, Ω_e are chosen as triangular elements.

The stress field at fracture tip as shown in Eq. (9) is dominated by the singularity whilst the stress field at remaining points is finite. So, in this work, the numerical approximation employed on the grid differs between the interior elements that are close to the fracture tip and the interior elements that are not. On elements that are not connected to the crack tip, the displacement field is approximated as a quadratic function, which is expressed in terms of the displaced values, $\mathbf{d}^h$, at the three vertices and the midpoints of the three edges such that

$$\mathbf{u} = \begin{Bmatrix} u \\ v \end{Bmatrix} \cong \mathbf{u}^h = \sum_{i=1}^6 \begin{Bmatrix} N_i(\xi,\eta) u_i \\ N_i(\xi,\eta) v_i \end{Bmatrix} = \mathbf{N} \mathbf{d}^h \tag{23}$$

where N_i are the shape functions of a 6-node triangular plane isoparametric element defined by Eq. A(1).

To represent the stress singularity at the fracture tip, quarter-point elements (QPE) (Barsoum, 1977) are employed. Each element around the crack tip, as shown in Fig. 2(a), is mapped by an 8-node plane isoparametric quadrilateral element, as shown in Fig. 2(b), so that

$$x = \sum_{i=1}^8 N_i(\xi,\eta) x_i,\ \ y = \sum_{i=1}^8 N_i(\xi,\eta) y_i \tag{24}$$

where N_i are the shape functions defined by Eq. A(2). Then, the displacement field is approximated through the displacements at 6 nodes, $\mathbf{d}^h$, as a quadratic function such that

$$\mathbf{u} = \begin{Bmatrix} u \\ v \end{Bmatrix} \cong \mathbf{u}^h = \sum_{i=1}^6 \begin{Bmatrix} N_i^*(\xi,\eta) u_i \\ N_i^*(\xi,\eta) v_i \end{Bmatrix} = \mathbf{N} \mathbf{d}^h \tag{25}$$

where N_i^* are defined by

$$\begin{cases} N_i^*(\xi,\eta) = N_1 + N_7 + N_8, & \text{if } i = 1, \\ N_i^*(\xi,\eta) = N_i, & \text{otherwise.} \end{cases} \tag{26}$$

By using the approximation given in Eq. (25), the numerical stress is singular at the crack tip, similar to the analytical formula shown in Eq. (9). More details are shown in Appendix A.

By substituting Eqs. (23) and (25) into Eq. (17), the discretized system can be written as

$$\mathbf{K} \mathbf{d}^h = \mathbf{F} = \mathbf{F}_b + \int_{\Gamma_N} \mathbf{N}^T \bar{\mathbf{t}}\, d\Gamma \tag{27}$$

where $\mathbf{K}$ and $\mathbf{F}_b$ are the global stiffness matrix and global body load vector, respectively, and are obtained by the assembly of the stiffness matrix and body load vector of each element ($\mathbf{K}_e$ and $\mathbf{F}_e$) that are expressed as

$$\mathbf{K}_e = \int_{\Omega_e} \mathbf{B}^T \mathbf{D} \mathbf{B} d\Omega,\ \ \mathbf{F}_e = \int_{\Omega_e} \mathbf{N}^T \mathbf{b} d\Omega \tag{28}$$

where $\mathbf{B}$ is the gradient matrix defined as

$$\mathbf{B} = \mathbf{L}\mathbf{N} \tag{29}$$

In the discrete system, the contact mechanics relations defined in Eq. (3) are manifested in the boundary conditions on the fracture, which takes different from depending on whether the fracture is in contact or not. This is treated at each pair of contact points by the active set strategy (Hüeber and Wohlmuth, 2005). The details of the active set algorithm are shown in Fig. 3 and explained as follows:

(1) Set k = 1, initialize $\mathbf{d}$ as an initial solution, predict a set of possible contact points V_P and assume the actual contact zone $\mathbb{C}^1 = V_P$. V_P is defined as

$$V_P = \{\mathbf{x}, \Re(\mathbf{x})\}, \quad \mathbf{x} \in \Gamma_C^+ \tag{30}$$

(2) Define the normal displacement jump $[\mathbf{u}(\mathbf{x})]_\mathbf{n}$ and normal traction $f_\mathbf{n}(\mathbf{x})$ at points $\{\mathbf{x}, \Re(\mathbf{x})\}$ by Eq. (2).

(3) With the current solution, the points $\{\mathbf{x}, \Re(\mathbf{x})\}$ are in contact if the normal displacement jump and normal traction satisfy the following condition:

$$c f_\mathbf{n}(\mathbf{x}) - \left\{ [\mathbf{u}(\mathbf{x})]_\mathbf{n} - g(\mathbf{x}) \right\} < 0, \quad \mathbf{x} \in \Gamma_C^+ \tag{31}$$

where c is a positive constant depending on the material. If Eq. (31) is satisfied, either $f_\mathbf{n}(\mathbf{x}) < 0$, $[\mathbf{u}(\mathbf{x})]_\mathbf{n} - g(\mathbf{x}) \geqslant 0$ or $f_\mathbf{n}(\mathbf{x}) = 0$, $[\mathbf{u}(\mathbf{x})]_\mathbf{n} - g(\mathbf{x}) > 0$. Therefore, the pair $\{\mathbf{x}, \Re(\mathbf{x})\}$ should be considered as the contact points for the calculation in the next step.

(4) Check if the contact zone at step k, $\mathbb{C}^k$, is the same as step $k+1$, $\mathbb{C}^{k+1}$. If yes then stop, else, the nonpenetration condition $[\mathbf{u}(\mathbf{x})]_\mathbf{n} - g(\mathbf{x}) = 0$ at the contact points is counted for the system by using the Lagrangian multiplier, then go to step (2).

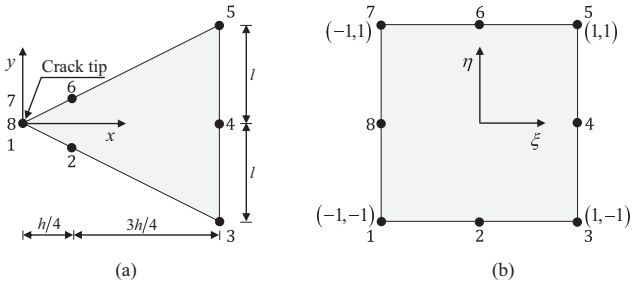

Fig. 2. Definition of the elements around the crack tip (a) and an 8-node plane isoparametric element (b).

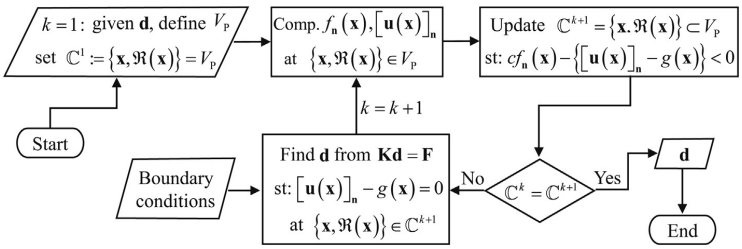

Fig. 3. The numerical solver for the contact mechanics problem.

3.2. Fracture propagation

The modeling of wing crack propagation is based on two assumptions. First, the wing crack emerges from the tip of the fracture, and second, a crack stops growing whenever its tip reaches a domain boundary or another fracture. That is, we do not consider the fracture propagation that crosses other fractures.

As detailed in Section 2.2, the fracture computation is based on the stress intensity factor evaluation. In this work, we compute SIFs by using the nodal displacement correlation technique (Parks, 1974) in conjunction with QPE (Barsoum, 1977; Henshell and Shaw, 1975) that not only captures the singularity of the stresses but also considerably improves the displacement near the crack tip, resulting in a more accurate computation of the SIFs (Khoei et al., 2008). Through the displacement of the QPE around a crack tip, these SIFs can be calculated as (Chen and Kuang, 1992; Kuang and Chen, 1993)

$$K_{\mathrm{I}} = \frac{E}{6(1+v)(1+k)}\sqrt{\frac{2\pi}{h}}[8(v'_{\mathrm{b}} - v'_{\mathrm{d}}) - (v'_{\mathrm{c}} - v'_{\mathrm{e}})] \tag{32}$$

$$K_{\mathrm{II}} = \frac{E}{6(1+v)(1+k)}\sqrt{\frac{2\pi}{h}}[8(u'_{\mathrm{b}} - u'_{\mathrm{d}}) - (u'_{\mathrm{c}} - u'_{\mathrm{e}})] \tag{33}$$

where $k = (3-v)/(1+v)$ for a plane stress problem and $k = 3-4v$ for a plane strain problem. As shown in Fig. 4(a), h is the crack tip rosette radius or size of the element around the crack tip. u' and v' are the local displacements of the nodal points located on the crack in the QPE, in which x' is aligned in the direction of the crack axis.

The advance of a fracture may cause difficulties in the current approach, and thus some special conditions need to be defined for the tip of propagating, approaching and intersecting fractures. For the propagating fracture, a new crack tip must be defined by the propagation length L_{adv} and crack initiation angle θ_0 each time a crack propagates. To ensure the validity of the grid and to reduce the computational cost associated with updates to the grid geometry, a tolerance for geometric mismatch based on the crack tip rosette radius h, $L^i_{\min} = 0.4h^i$ is introduced. If $L^i_{adv} < L^i_{\min}$, the crack will not be allowed to move, except in the special case when $\theta^i_0 = 0$, when the tip position is updated by moving the tip node to a new position. If $L^i_{adv} \geqslant L^i_{\min}$, the crack tip is extended by splitting the previous tip into two new nodes, as shown in Fig. 4(b). For the approaching fracture, when the distance between a growing crack tip and a boundary (external boundary or surface of another fracture), denoted by d_{bou}, is less than the crack tip rosette radius, they are assumed to be connected. A new crack tip belonging on the boundary is determined by the stretching of the current crack tip as shown in Fig. 5(a). After that the fracture joint is considered a T-shape, as shown in Fig. 5(b), by splitting both the previous and current tips.

A limitation of the present approach is its unability to predict through-going fracturing, which is one of the most challenging problem in computational fracture mechanics. The fracture propagation process presented here also entails that the grid geometry is updated in the vicinity of the crack, as detailed in the next subsection.

3.3. Adaptive remeshing

The accuracy of the numerical simulation depends on the quality of the mesh that is affected by the geometric discretization errors and the gradients of the solution within the individual elements. In this work, we use the adaptive mesh refinement to obtain a solution that satisfies a given mesh discretization error while minimizing the number of elements. The adaptive remeshing (ARM) process involves two techniques: first, mesh refinement based on the error estimator (Zienkiewicz and Zhu, 1987) is used to improve the accuracy of the numerical solution, and second, Laplacian smoothing (Buell and Bush, 1973; Field, 1988) is used to improve the quality of the mesh.

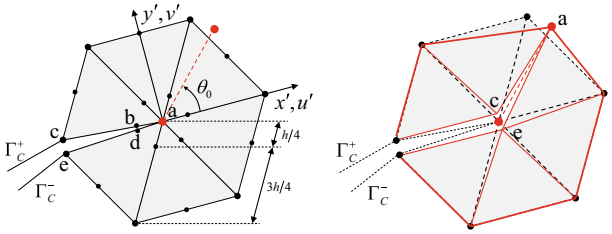

a) The quarter point elements around a crack tip b) Extension of a fracture

Fig. 4. The quarter point elements around a crack tip and the extension of a fracture.

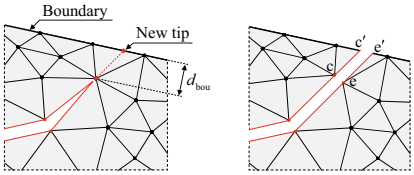

a) Determine new crack tip on boundary b) Fracture joined by T-shape

Fig. 5. The T-shaped intersection between a fracture and boundary.

3.3.1. Error estimator and refinements

The error estimator is based on the comparison between the numerical stress computed directly from the computed displacement field and a recovered stress with higher regularity. The numerical stress is directly computed by Eq. (1):

$$\boldsymbol{\sigma}^{\mathrm{h}} = \mathbf{C} : \frac{1}{2}\left[\nabla \mathbf{u}^{\mathrm{h}} + \left(\nabla \mathbf{u}^{\mathrm{h}}\right)^{\mathrm{T}}\right] \tag{34}$$

The quadratic approximation for the displacement renders a numerical stress that is a piecewise linear function on the elements and discontinuous across the interelement boundaries. To recover a globally continuous stress, we first define a nodal stress $\boldsymbol{\sigma}_i^*$ by area-weighted averaging of the elements in the surrounding node:

$$\boldsymbol{\sigma}_i^* = \frac{1}{\sum_{i=1}^{n} A_{\Omega_i}} \sum_{i=1}^{n} \int_{\Omega_i} \boldsymbol{\sigma}^{\mathrm{h}} \mathrm{d}\Omega \tag{35}$$

where A_{Ω_i} is the area of element Ω_i that has node i as a vertex. The recovered stress is then defined by linear interpolation between the stress values $\boldsymbol{\sigma}_i^*$.

The error at each element is estimated by the difference between the numerical and recovered stresses, such as

$$e_{\Omega_i} = \| \boldsymbol{\sigma}^{\mathrm{h}} - \boldsymbol{\sigma}^* \|_{\Omega_i} \tag{36}$$

The refinement is then performed based on a calculated error estimator. The essence of this process is to balance the errors between the elements. This means that the elements in regions of high error are locally refined. This process is repeated until the desired accuracy is obtained.

Fig. 6 illustrates the recovery process and mesh refinement in the case of the 1D domain. The refinement with a high estimated error (Ω_1 and Ω_2) increases the accuracy in both the displacement and the stress computations. With the same idea as the 1D, in a 2D problem, the element Ω_i that needs to be refined (Fig. 7(a)) is divided into four subelements by the connection between the midpoints of the edges (Fig. 7(b)). Three hanging nodes appear. These nodes are removed by connecting it to an opposite vertex, as shown in Fig. 7(c).

3.3.2. The mesh smoothing process

The mesh refinement process proposed above is local and therefore has a low implementation cost. However, the locality sometimes causes triangles with undesirable properties, such as overlapping elements. We improve the quality of the mesh by using the Laplacian smoothing process that is defined as follows: Let triangles $E_i,\ i = 1, \ldots, n$, share an internal vertex $\mathbf{x}^* = (x^*, y^*)$, and let the remaining vertices of E_i, be $\mathbf{x}_i = (x_i, y_i)$. The node $\mathbf{x}^*$ is updated by the equation

$$\mathbf{x}^* = \frac{1}{n}\sum_{i=1}^{M} \mathbf{x}_i \tag{37}$$

A precaution is taken to guarantee that the new coordinate assigned to $\mathbf{x}^*$ will define valid triangles. The new coordinate for $\mathbf{x}^*$ is immediately used for all subsequent Laplacian smoothing of other coordinates.

The general algorithm for the fracture propagation simulation in conjunction with the adaptive remeshing and accounting for the fracture contact mechanics is presented in Fig. 8. The item "numerical solver" requires the solution of the contact mechanics problem, as shown in Fig. 3.

4. Numerical investigation

In this section, four numerical examples are investigated. The first and second examples are intended for verification and validation purposes, investigating the convergence rates and comparison with the analytical solutions and experimental results. The last two examples are designed to show how the methodology can handle the complex case of shear deformation for a domain with multiple fractures, accounting for wing crack formation as well as fracture contact mechanics.

4.1. Method verification through convergence of computed strain energy

To evaluate the new approach, we consider a benchmark problem with the propagation of an isolated crack in a medium that undergoes tensile or shear stress. The medium is a general isotropic material characterised by its Young's modulus and Poisson ratio. For this problem, the performance of the second order finite element method and quarter point elements (FEM-QPE) with and without adaptive mesh refinement is compared to that of conventional finite elements. The performance is measured in terms of the accuracy of the strain energy and SIF computation under grid refinement.

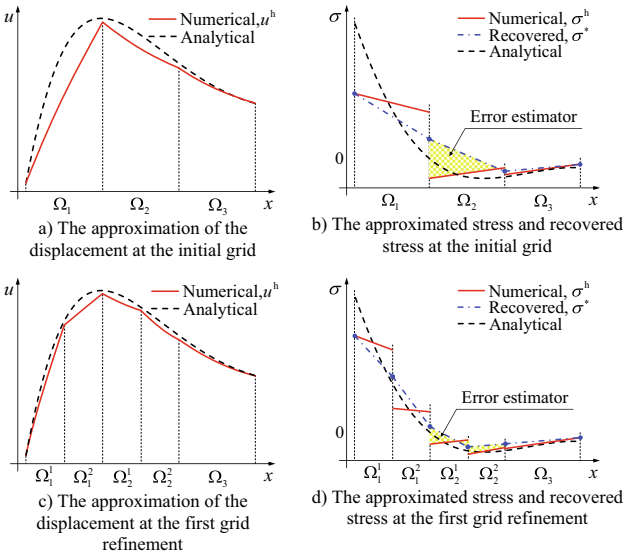

Fig. 6. The procedures for the error estimator and mesh refinement for a one-dimensional problem using a quadratic approximation.

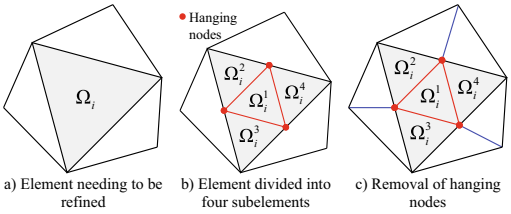

Fig. 7. The refinement processes.

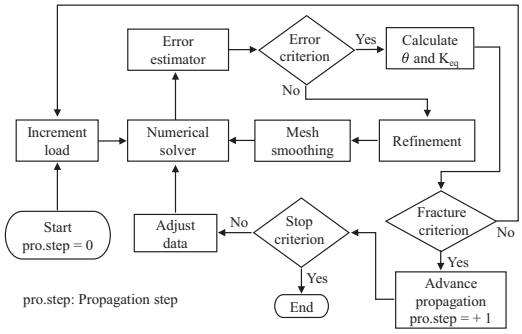

Fig. 8. Processing of the fracture propagation simulation.

The model problem is a thin rectangular plate (length L, width b, and thickness t) including a pre-existing edge fracture, which is subject to tensile (mode I) or shear (mode II) stress as illustrated in Fig. 9. To make a fair comparison, as shown in Fig. 10, the FEM and FEM-QPE use a unique mesh, while the variant of the latter method that includes ARM (FEM-ARM-QPE) uses a multi-size-mesh controlled by the error estimator. The strain energy is given by

$$U(\mathbf{u}) = \frac{1}{2}\int_{\Omega} \boldsymbol{\sigma}^{\mathrm{T}}\boldsymbol{\varepsilon}\,\mathrm{d}\Omega \tag{38}$$

For the plane stress singularity problem, the rate of convergence of the numerical solution is bounded satisfying (Pin and Pian, 1973)

$$U(\mathbf{u}^{\mathrm{h}} - \mathbf{u}^{\mathrm{exact}}) \leqslant ch^{2\alpha-2+n} \tag{39}$$

where $\mathbf{u}^{\mathrm{h}}$ and $\mathbf{u}^{\mathrm{exact}}$ denote the solution from the numerical method and the exact solution, and n and α are the spatial dimension of the domain and the singularity degree of solution near the point of singularity, respectively. In the current case, $n = 2$ and $\alpha = 1/2$ (by Eq. (9)); hence, the convergence of the strain energy is linear with h.

For the mode I study, the comparisons of the convergence of the strain energy between the three different methods are shown in Fig. 11(a, b). A linear convergence rate for the strain energy can be observed, in accordance with Eq. (39) and the conclusions by previous published studies (Mirza and Olson, 1978; Pin and Pian, 1973). However, the FEM-QPE is significantly more accurate than the FEM. The convergence rate of the FEM-ARM-QPE is better than that of the FEM, and its accuracy approaches that of the FEM-QPE if the mesh refinement is sufficiently good. The comparison with the analytical solution (Tada et al., 2000) for the stress intensity factor is shown in Fig. 11(c). The QPEs considerably improve the solution near and ahead of the crack tip and result in a more accurate computation of the SIF. The ARM technique reduces the computational cost while still ensures the accuracy of the computation of the strain energy and stress intensity factor. This is confirmed by Table 1, which shows the total number of degrees of freedom (DOF) and total number of elements for the three methods under grid refinement.

For the mode II study, the reference solutions are obtained by ANSYS for the strain energy and by ABAQUS (Treifi et al., 2008)

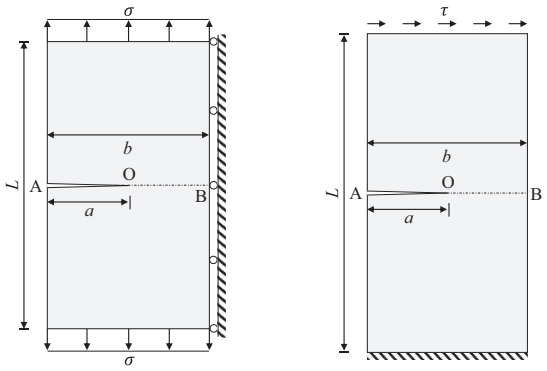

a) Edge-cracked plate subjected to a mode I loading condition

b) Edge-cracked plate subjected to a mode II loading condition

Fig. 9. Plane stress problem considered for the investigation of the convergence of the strain energy and SIFs.

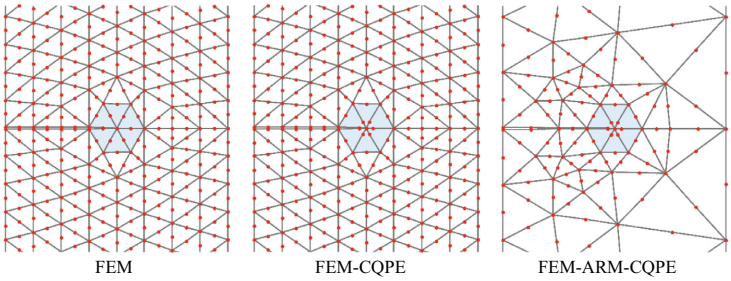

Fig. 10. The discretization with $h = b/8$.

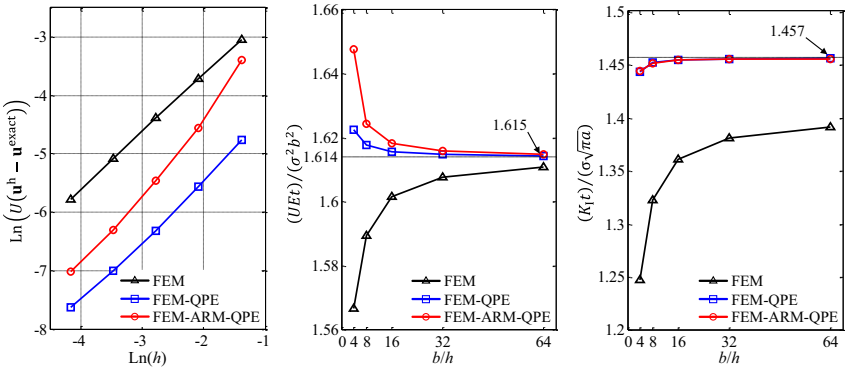

a) Error in the strain energy for mode I with grid refinement $b = 1$ m, $L/b = 2$, $b/a = 2$

b) Strain energy for mode I with grid refinement $b = 1$ m, $L/b = 2$, $b/a = 2$

c) SIF for mode I with grid refinement $b = 1$ m, $L>>b$, $b/a = 2$

Fig. 11. Convergence study for mode I.

for K_{II}. As shown in Fig. 12, as in the case of tensile stress, the QPE improves the accuracy of the solutions close to the stress singularity, and the ARM technique preserves the accuracy with fewer degrees of freedom.

The demonstrated accuracy and efficiency of the FEM-ARM-QPE methodology, shown in previous studies, make it suitable for numerical examples considering more complex geometries in the following section.

Table 1
Comparison between the computational costs of the three methods under grid refinement (L/b = 2, b/a = 2).

Computational costs	Method	b/h				
		4	8	16	32	64
Degrees of freedom (DOF)	FEM	330	1106	4290	16802	66402
	FEM-QPE	330	1106	4290	16802	66402
	FEM-ARM-QPE	214	678	1454	4970	17742
Total number of elements	FEM	68	248	1016	4088	16376
	FEM-QPE	68	248	1016	4088	16376
	FEM-ARM-QPE	44	152	340	1196	4348

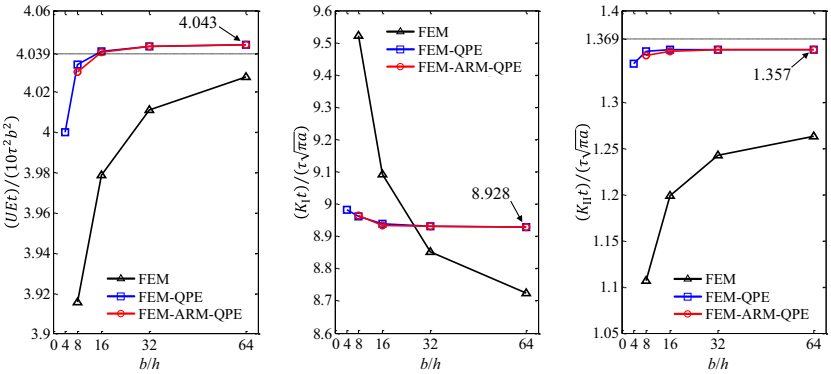

a) Strain energy for mode II with grid refinement b = 1 m, L/b = 2, b/a = 2

b) SIF for mode I with grid refinement b = 1 m, L/b = 2, b/a = 2

c) SIF for mode II with grid refinement b = 1 m, L/b = 2, b/a = 2

Fig. 12. Convergence study for mode II.

4.2. Model validation through stress intensity factor accuracy

To further validate the presented numerical model, FEM-ARM-QPE, the initiation and propagation of wing cracks from the ends of a pre-existing fracture under uniaxial compression loading are investigated. The test case focuses on the accuracy in the computation of the SIFs and fracture propagation paths for a case where both analytical (Atkinson et al., 1982) and experimental (Haeri et al., 2014b) data are available.

The computational domain is a disc-shaped rock specimen containing a central single pre-existing fracture, as shown in Fig. 13. Here, R and t denote the radius and thickness of the disc, and $2a$ is the length of the fracture. The fracture is inclined at an angle φ to the vertical direction at the center of the specimen. The specimen is compressed by two line loads $\mathbf{f}_0 = \{0, f_0\}$ and $-\mathbf{f}_0 = \{0, -f_0\}$ acting parallel to the y-axis. The material parameters are the Young's modulus E = 15 GPa, Poisson's ratio ν = 0.21, and fracture toughness K_{IC} = 2 MPa m$^{1/2}$ (Haeri et al., 2014b). On the existing fracture, a no-friction condition is assigned in the tangential direction. For this problem, the analytical solution for the SIFs is given by (Atkinson et al., 1982)

$$\left\{ \begin{matrix} K_I \\ K_{II} \end{matrix} \right\} = \frac{f_0\sqrt{a}}{\sqrt{\pi R}} \left\{ \begin{matrix} 1 - 4\sin^2\varphi + 4\sin^2\varphi(1 - 4\cos^2\varphi)\frac{a^2}{R^2} \\ 2\sin(2\varphi) + \sin(2\varphi)(8\cos^2\varphi - 5)\frac{a^2}{R^2} \end{matrix} \right\} \tag{40}$$

The fracture is a purely mode I fracture for $\varphi = 0^o$ and $\varphi = 90^o$, while it is a mixed mode fracture for all other angles, with shear effects being most pronounced at $\varphi = 45^o$.

Numerical, analytical and experimental results for the nondimensional SIFs considering different crack inclination angles are shown in Table 2 and Fig. 14. The computation of the SIFs by the FEM-ARM-QPE model is in good agreement with both the analytical solution (Atkinson et al., 1982) and the experimental data (Haeri et al., 2014b) for various inclination angles of the pre-existing crack.

Fig. 15 shows the computed propagation paths together with the experimental observations (Haeri et al., 2014b) of two wing cracks originating from the tips of the pre-existing fracture. The paths are symmetrically curvilinear and tend to migrate stably and gradually turn in the loading direction. A good agreement between the proposed model and the experiment is recognized in cases where $\varphi = 30^o$ and $\varphi = 60^o$. For $\varphi = 45^o$, the wing cracks obtained by the experiment are asymmetric and visibly different from those computed numerically. We do not consider this a concern for accuracy of the numerical method and note that the sim-

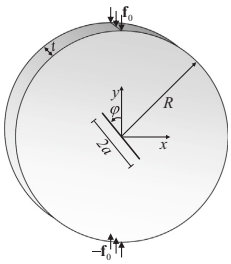

Fig. 13. Geometry of the specimen with a single pre-existing fracture.

Table 2
Comparison of K_I and K_{II} for different crack inclination angles (a = 5 mm, R = 42 mm).

φ (deg)	$K_I\sqrt{\pi R}/(f_0\sqrt{a})$			$K_{II}\sqrt{\pi R}/(f_0\sqrt{a})$		
	Present model	Analytical (Atkinson et al., 1982)	Experimental (Haeri et al., 2014b)	Present model	Analytical (Atkinson et al., 1982)	Experimental (Haeri et al., 2014b)
0	1.0269	1.0	1.0	0.0	0.0	0.0
15	0.7420	0.7323	0.715	1.0069	1.0175	1.017
30	−0.0272	0.0035	−0.016	1.7251	1.7443	1.778
45	−1.0417	−0.9858	−1.014	1.9601	1.9858	2.040
60	−2.0252	−1.9681	−2.054	1.6787	1.6952	1.712
75	−2.7469	−2.6827	−2.701	0.9580	0.9684	0.947
90	−3.0132	−2.9433	−2.948	0.0	0.0	0.0

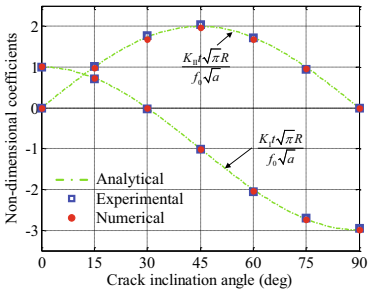

Fig. 14. Variation of nondimensional SIFs with crack inclination angles: Analytical by Atkinson et al., (1982); Experimental by Haeri et al., (2014b).

ulations consistently predict propagation towards the locations of the point loads, independent of the fracture rotation angle.

The agreement with the experimental observations in the above examples shows that the mathematical model and the simulation approach proposed in this work are valid for fracture propagation of wing cracks.

4.3. Wing crack propagation due to shearing along a pre-existing fracture

The third example investigates the formation and propagation of wing cracks in a domain with multiple pre-existing fractures, with fracture propagation driven by shearing along one of the fractures. The setup is designed so that the existing fractures will first be linked by newly formed wing cracks, followed by further wing crack formation from the extremities of the newly formed network. The objectives of the example are to analyse the propagation, connection, and final geometry of the generated fracture network. The material parameters are chosen to resemble those of a granite rock mass, with a Young's modulus E = 70 GPa, Poisson's ratio ν = 0.21, mass density $\rho = 2700$ Kg/m^3 and fracture toughness K_{IC} = 1.5 MPa m$^{1/2}$. The gravity is g = 9.8 m/s^2.

The initial configuration consists of three horizontal parallel natural fractures shown in Fig. 16. The geometrical parameters are W = 7 m, D = 6 m, thickness t = 1 m, a = 1 m, b = 0.5 m, and h_0 = 1 m. There is no opening of the pre-existing fractures. To mimic the subsurface conditions, we assume that this granite rock mass is located at a depth of H = 1000 m and subjected to in situ stresses resulting from the weight of the overlying strata (assumed to be granite) approximated by

$$\sigma_x = \frac{\nu}{1-\nu}\rho g H t, \quad \sigma_y = \rho g H t \tag{41}$$

A measurable slip, $\mathbf{u}_0 = \{u_0, 0\}$, is imposed on the middle fracture (fracture (2)), mimicking the slip due to the increase in the fluid pressure in the hydraulic shear stimulation of the fractures.

The growth of the wing cracks, the increment of slip and the number of DOFs during the fracture propagation are shown in Figs. 17 and 18. The number of DOFs is approximately doubled at the end of the simulation. When the pre-existing fracture (2) experiences slip u_0 = 0.012 mm in the tangential displacements, wing cracks emerge at its tips. They form an angle of approximately 70 degrees to the main fracture. By increasing the slip until u_0 = 0.147 mm, wing cracks from fracture (2) gradually turn in the direction perpendicular to the minimum principle stress and

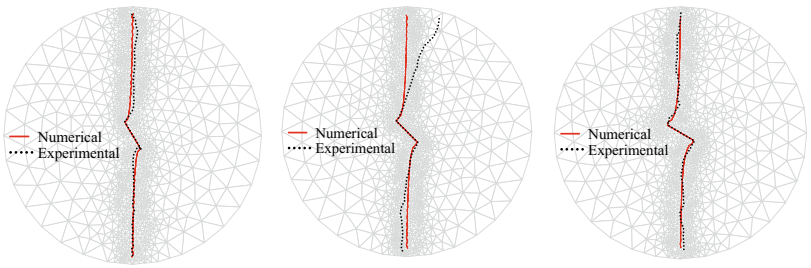

$\varphi = 30^o$ $f_0 = 1.55\text{x}10^6$ N/m 32 steps, DOF = 2352 – 8848

$\varphi = 45^o$ $f_0 = 1.40\text{x}10^6$ N/m 33 steps, DOF = 2264 – 9378

$\varphi = 60^o$ $f_0 = 2.03\text{x}10^6$ N/m 32 steps, DOF = 2440 – 9488

Fig. 15. Comparison of fracture propagation paths between the present model and experiment (Haeri et al., 2014b).

connect to fractures (1) and (3). By increasing the slip until u_0 = 0.3105 mm, two wing cracks newly emerge from fracture (1) and (3) and propagate away. As shown in Fig. 17, before the wing cracks from fracture (2) reach fractures (1) and (3), the surfaces of pre-existing fractures (1) and (3) are completely in contact. After that, the parts near the connected wing cracks open while the rests are still in contact. The change in the open/closed state of the fractures is caused by the influence of the in situ stresses and the interaction between multiple fractures.

4.4. Propagation of multiple fractures driven by the shearing boundary conditions

Finally, we consider a more complex case with multiple closed pre-existing fractures arbitrarily appearing in a specimen, as illustrated in Fig. 19. The proposed FEM-AMR-QPE technique is ideally suited to address the complexity of this problem in an efficient and accurate manner.

The size of the specimen is W = 7 m, D = 5 m, and thickness t = 1 m, while the rock parameters are set equal to those in Section 4.3. The fracture propagation is driven by a gradual increase in the tangential traction, τ, on the top and bottom boundaries of the domain, while the left and right boundaries are assigned traction free conditions.

The propagation trajectory is shown in Fig. 20. The increments of tangential traction and the number of DOFs are shown in Fig. 21. The DOFs increased by approximately 30% at the end of simulation. A wing crack first emerges at fracture (3) when the assigned tangential traction reached $\tau = 0.0746$ MPa. By increasing the tangential traction until $\tau = 0.4735$ MPa, a new wing crack emerges at the end of fracture (2). At $\tau = 0.4847$ MPa, wing cracks emerge at both tips of fracture (2) and propagate in opposite directions; one connects to fracture (3), and the other connects to fracture (1). After that, wing cracks appear at all tips of fractures (1) and (3) and propagate further at different lengths. During shear slip, fractures (4) and (5) do not propagate while the wing cracks propagate in the direction almost 45 degrees with that of tangential traction. Fracture (4) is completely closed during the simula-

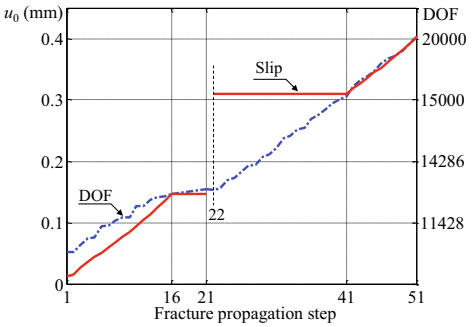

Fig. 18. Increment of slip and DOF during fracture propagation for example 4.3.

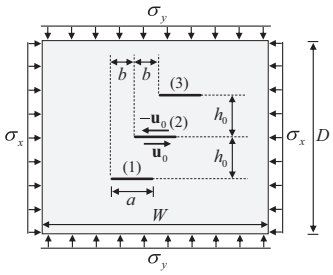

Fig. 16. Geometry of specimens with three pre-existing fractures.

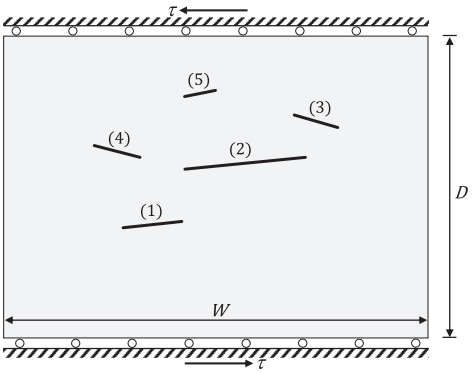

Fig. 19. Geometry of specimens with multiple pre-existing fractures.

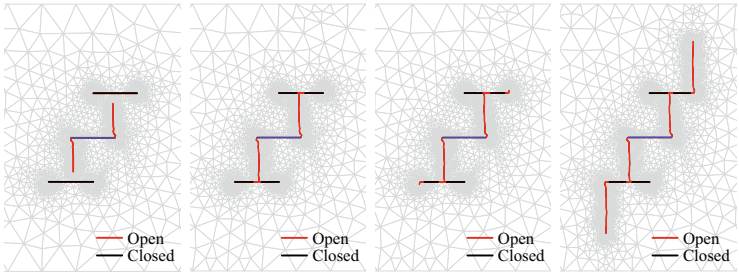

Fig. 17. The trajectories of the wing cracks caused by shear slip increasing until u_0 = 0.3105 mm at the interfaces of a pre-existing crack.

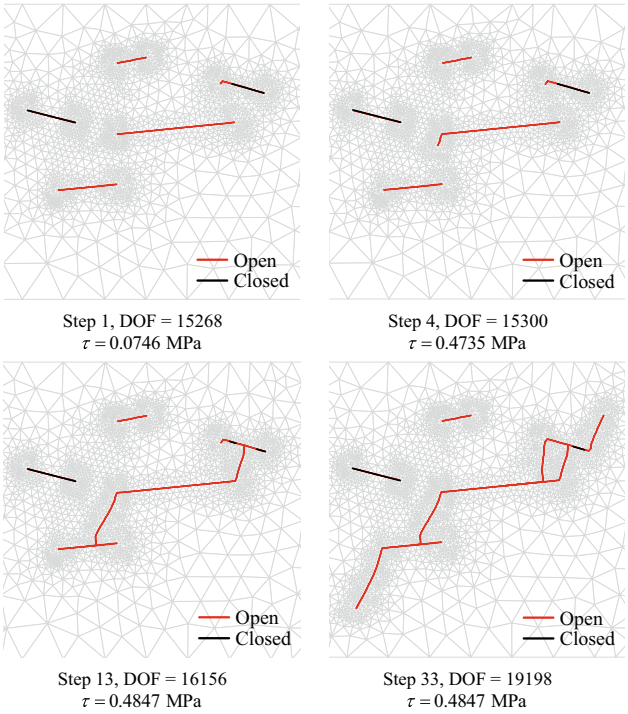

Fig. 20. The trajectories of wing cracks caused by shear slip at the top and bottom sides.

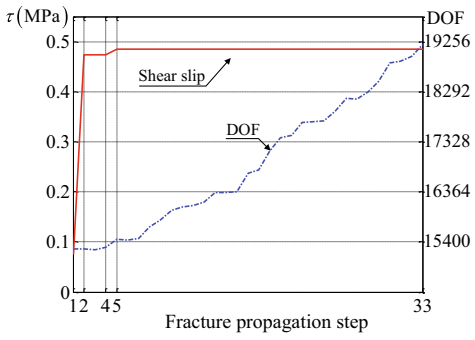

Fig. 21. Increment of slip and DOF during fracture propagation for example 4.4.

tion. Fracture (3) is completely closed before wing cracks emerge and is partly closed after that. The remaining fractures are tensile cracks during propagation. The results clearly show the further propagation of wing cracks under tangential traction and how the propagation of wing cracks and deformation of the larger fractures prevents wing crack propagation of the smaller fractures

The obtained results in example 4.3 and 4.4 show the interaction of different fractures, in which, a growing crack tip is weaker and more deformed when approaching other fractures. Similar observations on the fracture interaction has also been made by other authors, e.g. Thomas et al. (2017), Legrand and Lazarus (2015), and Laures and Kachanov (1991). For the simple symmetric geometry where an analytical solution exists, SIFs for interacting fracture tips computed by our developed methodology were also verified by the analytical solution by Kachanov (1987).

In the case of modeling multiple fractures propagation presented in examples 4.3 and 4.4 by FEM without ARM, a fine mesh is required to accurately capture propagated paths. A regular mesh in the same quality as the ones in the above examples consists almost 40.000 elements with approximated 200.000 DOFs. The number of DOFs by the regular mesh is approximately ten times more than one by the ARM mesh at the end of the simulation. Although ARM is costly for the element refinement in regions of high error, the adjustments of the mesh are local, and the cost of remeshing and discretization is negligible compared to a full discretization and solution of the corresponding algebraic equations. So, using the proposed ARM for the fracture propagation simulation is a great advantage when compared to approaches based on a regular mesh.

5. Conclusions

This work presented a numerical model for wing crack initiation and propagation due to shear slip. The governing mathematical model is based on linear elastic fracture mechanics and contact mechanics, along with failure and propagation criteria for multiple mixed-mode fracture propagation. The numerical solution approach is based on a combination of the finite element method combined with quarter point elements to handle the singularity at the fracture tips. The fracture contact mechanics are solved by

using the active set strategy. In addition, an adaptive remeshing based on an error estimator and Laplacian smoothing for implementation is utilized for computational efficiency.

Verification and validation studies of the methodology are presented, showing appropriate agreement between the analytical solutions and experimental observations for single fracture computation. More complex numerical test cases demonstrated the method's capabilities in investigating the development of wing cracks for situations where multiple fractures interact. The results show how the development of wing cracks interacts with the deformation and propagation of other existing fractures accounting for different fracture contact conditions as well as the overall stress regime.

Declaration of Competing Interest

The authors declare that they have no known competing financial interests or personal relationships that could have appeared to influence the work reported in this paper.

Acknowledgements

This work was funded by the ERiS project, grant #267909, Research Council of Norway.

Appendix A

- The 6-node triangular shape functions are defined by

$$N_i(\xi,\eta)=(1-\xi-\eta)(1-\xi_i-\eta_i)[16(\xi\xi_i+\eta\eta_i)+(1-2\xi-2\eta)(1-2\xi_i-2\eta_i)] +\xi\xi_i(2\xi-1)(2\xi_i-1)+16\xi\eta\xi_i\eta_i+\eta\eta_i(2\eta-1)(2\eta_i-1) \quad \text{A(1)}$$

- The 8-node quadrilateral shape functions are defined by

$$N_i(\xi,\eta)=\begin{matrix}\frac{\xi_i^2\eta_i^2}{4}[(1+\xi\xi_i)(1+\eta\eta_i)-(1-\xi^2)(1+\eta\eta_i)-(1+\xi\xi_i)(1-\eta^2)] \\ \frac{\eta_i^2}{2}(1-\xi_i)(1-\xi^2)(1+\eta\eta_i)+\frac{\xi_i^2}{2}(1-\eta_i^2)(1+\xi\xi_i)(1-\eta^2)\end{matrix} \quad \text{A(2)}$$

- The details of the QPE formulation.

Substituting specific coordinates of 6 nodes (x_i, y_i) as shown in Fig. 2(a) into Eq. (24) gives

$$x=\frac{h}{4}(1+\xi)^2,\quad y=\frac{l}{4}(1+\xi)^2\eta \quad \text{A(3)}$$

By assuming r is the distance from point (x, y) to the crack tip gives

$$r=\sqrt{x^2+y^2}\Rightarrow(1+\xi)=\sqrt{r}A_0(h,l,\eta) \quad \text{A(4)}$$

The Jacobian of the transformation $[\mathbf{J}]$ is given by

$$[\mathbf{J}]=\begin{bmatrix}\partial x/\partial\xi & \partial y/\partial\xi\\ \partial x/\partial\eta & \partial y/\partial\eta\end{bmatrix}=\frac{1}{4}\begin{bmatrix}2h(1+\xi) & 2l\eta(1+\xi)\\ 0 & l(1+\xi)^2\end{bmatrix} \quad \text{A(5)}$$

Taking the derivatives both sides of Eq. (25) gives

$$\left\{\begin{matrix}\frac{\partial\mathbf{u}^h}{\partial x} & \frac{\partial\mathbf{u}^h}{\partial y}\end{matrix}\right\}^T=[\mathbf{J}]^{-1}\left\{\begin{matrix}\frac{\partial\mathbf{N}}{\partial\xi} & \frac{\partial\mathbf{N}}{\partial\eta}\end{matrix}\right\}^T\mathbf{d}^h \quad \text{A(6)}$$

The derivatives of the displacement can be explicitly written in the form

$$\begin{matrix}\frac{\partial u^h}{\partial x}=\frac{1}{(\xi+1)}A_1(h,u_i,\eta)+A_2(h,u_i),\quad \frac{\partial v^h}{\partial x}=\frac{1}{(\xi+1)}A_1(h,v_i,\eta)+A_2(h,v_i)\\ \frac{\partial u^h}{\partial y}=\frac{1}{(\xi+1)}B_1(l,u_i,\eta)+B_2(l,u_i),\quad \frac{\partial v^h}{\partial y}=\frac{1}{(\xi+1)}B_1(l,v_i,\eta)+B_2(l,v_i)\end{matrix} \quad \text{A(7)}$$

By combining Eq. (1), Eq. A(4) and Eq. A(7), the stress components from the numerical method are defined by

$$\begin{Bmatrix}\sigma_x^h\\ \sigma_y^h\\ \tau_{xy}^h\end{Bmatrix}=\frac{1}{\sqrt{r}A_0(h,l,\eta)}\mathbf{D}\begin{Bmatrix}A_1(h,u_i,\eta)+A_2(h,u_i)\\ B_1(l,v_i,\eta)+B_2(l,v_i)\\ A_1(h,v_i,\eta)+A_2(h,v_i)+B_1(l,u_i,\eta)+B_2(l,u_i)\end{Bmatrix} \quad \text{A(8)}$$

where A_i and B_i are defined by

$$A_0(h,l,\eta)=2\left(h^2+l^2\eta^2\right)^{-\frac{1}{4}} \quad \text{A(9)}$$

$$A_1(h,u_i,\eta)=\frac{1}{h}\begin{bmatrix}3u_1+2(\eta+1)u_2-(3\eta^2+\eta+2)u_3\\ +(3\eta^2+1)u_4-(3\eta^2-\eta+2)u_5-2(\eta-1)u_6\end{bmatrix} \quad \text{A(10)}$$

$$A_2(h,u_i)=\frac{1}{h}(2u_1-2u_2+u_3+u_5-2u_6) \quad \text{A(11)}$$

$$B_1(l,u_i,\eta)=\frac{1}{l}[-4u_2+2(\eta+1)u_3-4\eta u_4+(2\eta-1)u_5+4u_6] \quad \text{A(12)}$$

$$B_2(l,u_i)=\frac{1}{l}(2u_2-u_3+u_5-2u_6) \quad \text{A(13)}$$

It is clear that as $r\to 0$ (which means $\xi\to 0$ and/or $\eta\to 0$), the terms A_i and B_i become constants. Therefore, the numerical stresses in Eq. A(8) tend to $O(1/\sqrt{r})$.

Appendix B

Influence of the interaction on stress intensity factor

The interaction between multiple fractures is an important consideration on the fracture propagation simulation. In this section, the SIFs of interacting fractures were evaluated by the FEM-ARM-QPE in comparison with the exact solution for a geometrically simple test case, which is also extended to investigate the effect of the fracture's location. The setup model for this problem is shown in Fig. B1. Two fractures of the same size (length a) exist in a domain (Fig. B1 (a)). The fracture (1) is inclined at an angle φ to the horizontal direction while the fracture (2) is always parallel to the horizontal direction. The horizontal distance between the fractures is $2b$. Firstly, the SIFs around a interacting tip of fracture (2) (denoted by $K_{I,II}^{int}$) that is interacting with fracture (1) are calculated. Then, fracture (1) is removed (Fig. B1 (b)), and SIFs are calculated around an isolated tip (denoted by $K_{I,II}^{iso}$) for the fracture (2). In this way, the same geometry for fracture (2) is tested twice, and the changes in the SIFs can be examined through the ratio between $K_{I,II}^{int}$ and $K_{I,II}^{iso}$.

The changes in SIFs are investigated due to changes of distance between these existing fractures and the incline of the fracture (1). The values of K_I^{int}/K_I^{iso} and $K_{II}^{int}/K_{II}^{iso}$ are shown in Tables B1 and B2, respectively, for the tension by applying a normal traction and shearing by applying a shear traction. A visual view of the influence of distance on SIFs is shown in Fig. B2. For the tension of two colinear fractures, the present results are compared with the exact solution presented by Kachanov (1987). A good agreement with the exact solution is observed. As expected, the influence of the interaction on SIFs decreases as the fractures move apart.

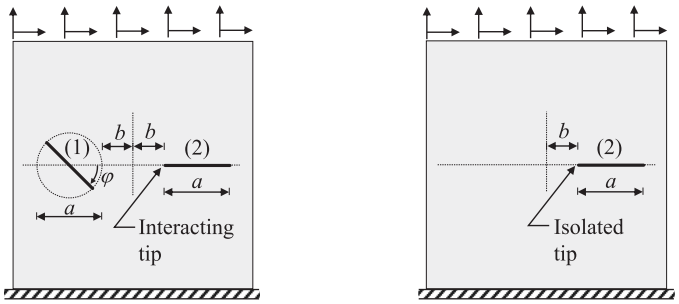

a) Interacting fractures b) Isolated fracture

Fig. B1. Model of interacting fractures.

Table B1
The values of K_I^{int}/K_I^{iso} change due to interaction of two fractures (Poisson's ratio is 0.25).

b/a	$\varphi = 0^o$		$\varphi = 30^o$	$\varphi = 45^o$	$\varphi = 60^o$	$\varphi = 90^o$
	Present model	Exact (Kachanov, 1987)	Present model	Present model	Present model	Present model
0.02	1.9253	1.905	1.3716	1.1980	1.0921	1.0133
0.05	1.4974	1.473	1.3076	1.1683	1.0786	1.0090
0.1	1.2854	1.255	1.2235	1.1321	1.0636	1.0051
0.2	1.1568	1.112	1.1233	1.0835	1.0453	1.0084
0.5	1.0542	-	1.0406	1.0254	1.0081	0.9949
1.0	1.0266	-	1.0201	1.0159	1.0094	1.0058
1.5	1.0153	-	1.0109	1.0094	1.0056	1.0037

Table B2
The values of $K_{II}^{int}/K_{II}^{iso}$ change due to interaction of two fractures (Poisson's ratio is 0.25).

b/a	$\varphi = 0^o$	$\varphi = 30^o$	$\varphi = 45^o$	$\varphi = 60^o$	$\varphi = 90^o$
0.02	1.8777	1.0533	1.0560	1.0913	1.1272
0.05	1.4968	1.0769	1.0684	1.0885	1.1097
0.1	1.2905	1.1156	1.0876	1.0945	1.1016
0.2	1.1571	1.1077	1.0889	1.0895	1.0817
0.5	1.0544	1.0584	1.0528	1.0474	1.0372
1.0	1.0242	1.0308	1.0312	1.0293	1.0225
1.5	1.0190	1.0252	1.0262	1.0248	1.0188

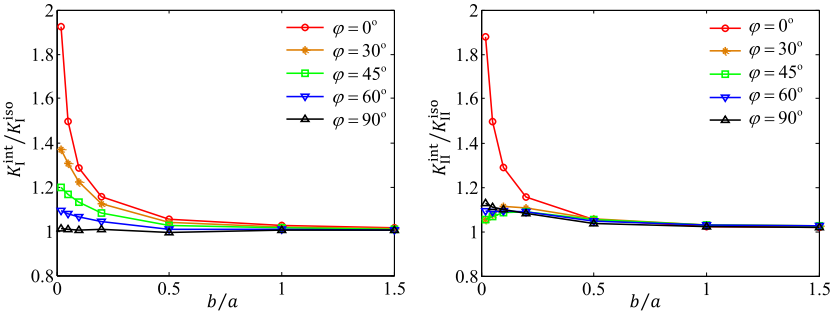

a) Change SIF of mode I under normal loading b) Change SIF of mode II under shear loading

Fig. B2. Change in SIFs with relative distance between two fracture.

References

Anderson, T.L., 2017. Fracture Mechanics: Fundamentals and Applications. CRC Press.

Asgian, M.I., 1988. A numerical study of fluid flow in a deformable, naturally fractured reservoir: the influence of pumping rate on reservoir response. In: The 29th U.S. Symposium on Rock Mechanics (USRMS). American Rock Mechanics Association, Minneapolis, Minnesota, p. 8

Atkinson, C., Smelser, R.E., Sanchez, J., 1982. Combined mode fracture via the cracked Brazilian disk test. Int. J. Fract. 18, 279–291.

Barsoum, R.S., 1977. Triangular quarter-point elements as elastic and perfectly-plastic crack tip elements. Int. J. Numer. Methods Eng. 11, 85–98.

Bobet, A., Einstein, H.H., 1998. Fracture coalescence in rock-type materials under uniaxial and biaxial compression. Int. J. Rock Mech. Min. Sci. 35, 863–888.

Bryant, E.C., Sun, W., 2018. A mixed-mode phase field fracture model in anisotropic rocks with consistent kinematics. Comput. Methods Appl. Mech. Eng. 342, 561–584.

Buell, W.R., Bush, B.A., 1973. Mesh generation-a survey. J. Eng. Ind. 95, 332–338.

Chen, L.S., Kuang, J.H., 1992. A modified linear extrapolation formula for determination of stress intensity factors. Int. J. Fract. 54, R3–R8.

Cheng, Q., Wang, X., Ghassemi, A., 2019. Numerical simulation of reservoir stimulation with reference to the Newberry EGS. Geothermics 77, 327–343.

Erdogan, F., Sih, G.C., 1963. On the crack extension in plates under plane loading and transverse shear. J. Basic Eng. 85, 519–525.

Field, D.A., 1988. Laplacian smoothing and Delaunay triangulations. Commun. Appl. Numer. Methods 4, 709–712.

Gonçalves da Silva, B., Einstein, H., 2013. Modeling of crack initiation, propagation and coalescence in rocks. Int. J. Fract. 182, 167–186.

Haeri, H., Shahriar, K., Fatehi Marji, M., Moarefvand, P., 2014a. Experimental and numerical study of crack propagation and coalescence in pre-cracked rock-like disks. Int. J. Rock Mech. Min. Sci. 67, 20–28.

Haeri, H., Shahriar, K., FatehiMarji, M., Moarefvand, P., 2014b. On the crack propagation analysis of rock like Brazilian disc specimens containing cracks under compressive line loading. Lat. Am. J. Solids Struct. 11, 1400–1416.

Henshell, R.D., Shaw, K.G., 1975. Crack tip finite elements are unnecessary. Int. J. Numer. Methods Eng. 9, 495–507.

Hesch, C., Franke, M., Dittmann, M., Temizer, I., 2016. Hierarchical NURBS and a higher-order phase-field approach to fracture for finite-deformation contact problems. Comput. Methods Appl. Mech. Eng. 301, 242–258.

Horii, H., Nemat-Nasser, S., 1985. Compression-induced microcrack growth in brittle solids: axial splitting and shear failure. J. Geophys. Res. Solid Earth 90, 3105–3125.

Hüeber, S., Stadler, G., Wohlmuth, B., 2008. A primal-dual active set algorithm for three-dimensional contact problems with coulomb friction. SIAM J. Sci. Comput. 30, 572–596.

Hüeber, S., Wohlmuth, B., 2005. A primal–dual active set strategy for non-linear multibody contact problems. Comput. Methods Appl. Mech. Eng. 194, 3147–3166.

Ingraffea, A.R., Heuze, F.E., 1980. Finite element models for rock fracture mechanics. Int. J. Numer. Anal. Methods Geomech. 4, 25–43.

Ingraffea, A.R., Manu, C., 1980. Stress-intensity factor computation in three dimensions with quarter-point elements. Int. J. Numer. Methods Eng. 15, 1427–1445.

Jaeger, J.C., Cook, N.G.W., Zimmerman, R., 2007. Fundamentals of Rock Mechanics. Wiley.

Jung, R., 2013. In: EGS — Goodbye or Back to the Future, Effective and Sustainable Hydraulic Fracturing. InTech, pp. 95–121.

Kachanov, M., 1987. Elastic solids with many cracks: a simple method of analysis. Int. J. Solids Struct. 23, 23–43.

Kamali, A., Ghassemi, A., 2018. Analysis of injection-induced shear slip and fracture propagation in geothermal reservoir stimulation. Geothermics 76, 93–105.

Kim, J., Duarte, C.A., 2015. A new generalized finite element method for two-scale simulations of propagating cohesive fractures in 3-D. Int. J. Numer. Methods Eng. 104, 1139–1172.

Khoei, A.R., Azadi, H., Moslemi, H., 2008. Modeling of crack propagation via an automatic adaptive mesh refinement based on modified superconvergent patch recovery technique. Eng. Fract. Mech. 10, 2921–2945.

Kuang, J.H., Chen, L.S., 1993. A displacement extrapolation method for two-dimensional mixed-mode crack problems. Eng. Fract. Mech. 46, 735–741.

Laures, J.-P., Kachanov, M., 1991. Three-dimensional interactions of a crack front with arrays of penny-shaped microcracks. Int. J. Fract. 48, 255–279.

Legrand, L., Lazarus, V., 2015. Front shape and loading evolution during cracks coalescence using an incremental perturbation method. Eng. Fract. Mech. 133, 40–51.

Liu, G.R., Quek, S.S., 2003. In: Finite Element Method: A Practical Course. Butterworth-Heinemann, Oxford, pp. 1–11.

McClure, M.W., Horne, R.N., 2014. An investigation of stimulation mechanisms in Enhanced Geothermal Systems. Int. J. Rock Mech. Min. Sci. 72, 242–260.

Mirza, F.A., Olson, M.D., 1978. Energy convergence and evaluation of stress intensity factor KI for stress singular problems by mixed finite element method. Int. J. Fract. 14, 555–573.

Nejati, M., Paluszny, A., Zimmerman, R.W., 2016. A finite element framework for modeling internal frictional contact in three-dimensional fractured media using unstructured tetrahedral meshes. Comput. Methods Appl. Mech. Eng. 306, 123–150.

Norbeck, J.H., McClure, M.W., Horne, R.N., 2018. Field observations at the Fenton Hill enhanced geothermal system test site support mixed-mechanism stimulation. Geothermics 74, 135–149.

Oden, J.T., Pires, E.B., 1983. Nonlocal and nonlinear friction laws and variational principles for contact problems in elasticity. J. Appl. Mech. 50, 67–76.

Paluszny, A., Matthäi, S.K., 2009. Numerical modeling of discrete multi-crack growth applied to pattern formation in geological brittle media. Int. J. Solids Struct. 46, 3383–3397.

Paris, P., Erdogan, F., 1963. A critical analysis of crack propagation laws. J. Fluids Eng. 85, 528–533.

Parks, D.M., 1974. A stiffness derivative finite element technique for determination of crack tip stress intensity factors. Int. J. Fract. 10, 487–502.

Pin, T., Pian, T.H.H., 1973. On the convergence of the finite element method for problems with singularity. Int. J. Solids Struct. 9, 313–321.

Renshaw, C.E., Pollard, D.D., 1994. Numerical simulation of fracture set formation: a fracture mechanics model consistent with experimental observations. J. Geophys. Res. Solid Earth 99, 9359–9372.

Sharafisafa, M., Nazem, M., 2014. Application of the distinct element method and the extended finite element method in modelling cracks and coalescence in brittle materials. Comput. Mater. Sci. 91, 102–121.

Tada, H., Paris, P.C., Irwin, G.R., 2000. The Stress Analysis of Cracks Handbook. ASME Press, Norwood Mass.

Thomas, R.N., Paluszny, A., Zimmerman, R.W., 2017. Quantification of fracture interaction using stress intensity factor variation maps. J. Geophys. Res. Solid Earth 122, 7698–7717.

Treifi, M., Olutunde Oyadiji, S., Tsang, D.K.L., 2008. Computations of modes I and II stress intensity factors of sharp notched plates under in-plane shear and bending loading by the fractal-like finite element method. Int. J. Solids Struct. 45, 6468–6484.

Wohlmuth, B., 2011. Variationally consistent discretization schemes and numerical algorithms for contact problems. Acta Numer. 20, 569–734.

Wong, L.N.Y., Einstein, H.H., 2009. Systematic evaluation of cracking behavior in specimens containing single flaws under uniaxial compression. Int. J. Rock Mech. Min. Sci. 46, 239–249.

Zhang, X., Sloan, S., Vignes, C., Sheng, D., 2017. A modification of the phase-field model for mixed mode crack propagation in rock-like materials. Comput. Methods Appl. Mech. Eng. 322, 123–136.

Zienkiewicz, O.C., Taylor, R.L., Zhu, J.Z., 2005. The Finite Element Method: Its Basis and Fundamentals. Elsevier Science.

Zienkiewicz, O.C., Zhu, J.Z., 1987. A simple error estimator and adaptive procedure for practical engineerng analysis. Int. J. Numer. Methods Eng. 24, 337–357.

Paper C

Two-level simulation of injection-induced fracture shear deformation and wing-crack propagation in poroelastic media

Hau Trung Dang, Eirik Keilegavlen, Inga Berre

International Journal of Rock Mechanics and Mining Sciences. Vol. 160, 105248. 2022.

DOI: 10.1016/j.ijrmms.2022.105248

https://www.sciencedirect.com/science/article/pii/S1365160922002143

International Journal of Rock Mechanics & Mining Sciences 160 (2022) 105248

Contents lists available at ScienceDirect

International Journal of Rock Mechanics and Mining Sciences

journal homepage: www.elsevier.com/locate/ijrmms

Two-level simulation of injection-induced fracture slip and wing-crack propagation in poroelastic media

Hau Trung Dang *, Inga Berre, Eirik Keilegavlen

Center for Modeling of Coupled Subsurface Dynamics, Department of Mathematics, University of Bergen, Norway

ARTICLE INFO

Keywords:
Hydraulic stimulation
Fracture propagation
Fault slip
Poroelasticity
Two-level simulation
Contact mechanics
Open-source software

ABSTRACT

In fractured poroelastic media under high differential stress, the shearing of pre-existing fractures and faults and propagation of wing cracks can be induced by fluid injection. This paper presents a two-dimensional mathematical model and a numerical solution approach for coupling fluid flow with fracture shearing and propagation under hydraulic stimulation by fluid injection. Numerical challenges are related to the strong coupling between hydraulic and mechanical processes, the material discontinuity the fractures represent in the medium, and the strong effect that fracture deformation and propagation have on the physical processes. The solution approach is based on a two-level strategy that is classified into the coarse and fine levels. In the coarse level, flow in and poroelastic deformation of the matrix are coupled with the flow in the fractures and fracture contact mechanics, allowing fractures to frictionally slide. Fracture propagation is handled at the fine level, where the maximum tangential stress criterion triggers the propagation of fractures, and Paris' law governs the fracture growth processes. Simulations show how the shearing of a fracture due to fluid injection is linked to fracture propagation, including cases with hydraulically and mechanically interacting fractures.

1. Introduction

In the hydraulic stimulation of geothermal reservoirs in igneous rocks, elevated pressures in combination with anisotropic stress conditions result in shear displacement and the dilation of fractures and faults favorably oriented to slip, propagation of wing cracks from sliding or shearing fractures, and/or propagation of hydraulic fractures.[1–4] Sliding, dilation, and the propagation of fractures affect the stress and flow regime in the formation and, thereby, the stress state and deformation of nearby fractures. The coupling between flow in fractured and faulted rocks, fracture slip and propagation, and poromechanical matrix deformation is strong: fracture propagation occurs locally but impacts and interacts with macroscopic reservoir-scale flow and deformation of the fractured rock.

The current work presents a modeling approach for hydraulic stimulation of fractured reservoirs under anisotropic stress. In this case, depending on the elevation of fluid pressure, the stimulation will cause slip of pre-existing fractures as well as fracture propagation. Slips of pre-existing fractures occur when coupled hydromechanical processes induced by fluid injection result in changes to the effective stress regime so that the fracture's frictional resistance to slip is exceeded.[5,6] The stress alterations resulting from fracture slip are coupled with fluid pressurization and drive tensile propagation of wing cracks at the fracture's tips. Hence, in contrast to most of the research literature on fracture propagation resulting from hydraulic stimulation, this work does not only consider the development of tensile hydrofractures. Instead, the reservoir stimulation is caused by a combination of slip of pre-existing fractures with fracture propagation.[1–3] Following McClure and Horne,[2] we refer to this as mixed-mechanism stimulation.

To fully represent how injection operations alter fractured rock characteristics, simulation models must capture both the slip and deformation of existing fractures as well as fracture propagation. In addition, they must be able to account for the heterogeneous characteristics of subsurface formations. Challenges are related to capturing how the hydromechanical processes in the matrix interact with the flow, deformation, and propagation of fractures. This includes accounting for fracture contact mechanics, with the possibility of fractures being closed, sliding, and open.

To model the physics of these phenomena, fractures must be represented explicitly in an otherwise intact porous medium, conceptually leading to a discrete fracture-matrix model. To avoid resolving thin fractures in their normal direction, fractures are represented as co-

* Corresponding author. Department of Mathematics, University of Bergen, Postboks 7803, 5020, Bergen, Norway.
E-mail addresses: Hau.Dang@uib.no, dtrhau@gmail.com (H.T. Dang), Inga.Berre@uib.no (I. Berre), Eirik.Keilegavlen@uib.no (E. Keilegavlen).

https://doi.org/10.1016/j.ijrmms.2022.105248
Received 28 March 2022; Received in revised form 27 September 2022; Accepted 18 October 2022
Available online 11 November 2022

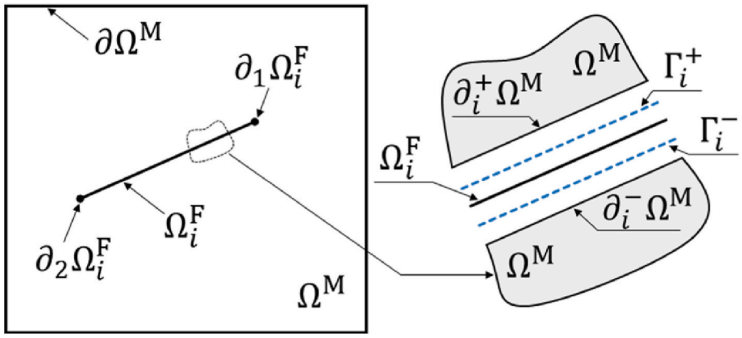

Fig. 1. Illustration of a fracture, Ω_i^F and a host medium, Ω^M.

dimension one objects embedded in the host medium with corresponding dimensionally reduced equations, resulting in a mixed-dimensional model.[7] Discretizations of such models can be both nonconforming and conforming. While conforming methods align the computational grid to the fractures, nonconforming methods utilize enrichment functions to capture the effects of the fractures. Recently, the nonconforming XFEM methodology, which has previously been developed for hydraulic fracture propagation,[8–11] has been extended to couple fracture propagation with fracture contact mechanics in impermeable media.[12,13] A conforming method allows the direct assignment of variables and governing equations to the host medium, the fracture, and the matrix-fracture interface. For fluid flow, this flexibility simplifies the task of correctly capturing fluid exchange within and between fractures and the matrix. Furthermore, a conforming fracture representation allows for the modeling of fracture contact mechanics in poroelastic media,[9,10,14–16] including fracture propagation[17,18] in a manner that directly couples shear and normal displacements along the fracture with alterations in stress and flow regime.[19]

In numerical modeling of fracture mechanics in porous media caused by fluid injection, numerical models have generally focused either (1) on the tensile propagation of hydraulic fractures or (2) the deformation of pre-existing fractures or faults. The first regime ignores the deformation of existing fractures caused by frictional contact and governs the growth of fractures by Mode I fracturing.[8,10,15,20–31] The second regime focuses on the frictional sliding, dilation and/or opening of pre-existing fractures or faults without considering fracture propagation.[11,19,32–37] Some recent models couple both regimes.[2,18,19,38] However, the coupling of hydromechanical processes between fractures and the matrix and the fracture propagation in these models are typically based on strong assumptions. For example, fracture dilation is assumed to not affect the surrounding stress[2,18] and restrictions allow fractures to propagate only along predefined paths[2] or the edges of fixed grid cells.[18,38–41]

This work presents a numerical model, based on conforming discretizations, for injection-induced fracture shear-deformation and wing-crack propagation in poroelastic media without these limitations. Biot's model for poroelasticity governs flow and deformation in the matrix, with the deformation of fractures represented by contact mechanics, which consider the fractures' frictional resistance to sliding.[19] The fracture growth process is governed by the maximum tangential stress criterion and Paris's law.[42,43] A primary motivation for our work is to enable simulations on domains that are too large for the fracture propagation to be resolved in detail. To that end, we separate the poroelastic matrix deformation and fracture shearing from the fracture propagation in a two-level approach. A relatively coarse grid can be accepted for flow, poroelastic matrix deformation, and fracture deformation. In contrast, to capture the stress and correctly evaluate fracture propagation, a refined grid is needed around the fracture tip. As fracture propagation occurs locally from the fracture's tips,[2,44] an efficient solution strategy can be defined based on multilevel methods,[45–47] which in this work is cast in the language of the heterogeneous multiscale approach.[45,48] Flow, poroelastic deformation, and contact mechanics of fractures are evaluated in a coarse-level model, and mechanical fracture propagation is evaluated in a local fine-level model[48] subject to body forces and boundary conditions that also account for the influence of macroscale fluid pressure. The models are coupled via displacement fields close to fracture tips (coarse level to fine level) and updates to the fracture path (fine level to coarse level).

In discretizing the coarse-level model, a finite volume method for fracture and matrix flow and poroelastic matrix deformation is combined with an active set strategy for fracture contact mechanics.[19] For fracture propagation on the fine level, a finite element method is applied in combination with collapsed quarter-point elements at the fracture tips to capture their stress singularity.[17,49] Adaptive remeshing is introduced on both levels to account for fracture propagation based on the implementation by Dang-Trung et al.[17] This work presents numerical examples that focus on the method's ability to balance accuracy and computational cost under variations in grid resolution and the parameters which govern the coupling between the coarse- and fine-level modeling. This work also presents a case with multiple hydromechanically coupled fractures, showcasing the capacity of our methodology to solve complex problems.

The paper is structured as follows. Section 2 presents the governing equations and Section 3 presents the two-level solution strategy. Section 4 presents a numerical approach that employs a novel combination of a finite volume method for the poroelastic deformation of existing fractures with a finite element approach for the fracture propagation process. Section 5 presents several numerical test cases to show the stability and accuracy of the proposed approach and its potential in settings where multiple fractures mutually affect each other.

2. Mathematical model

The mathematical model for injection-induced fracture shear deformation and wing-crack propagation in poroelastic media is based on systems of partial differential equations and KKT conditions governing the physics. We start by introducing notations of geometry and primary variables. Then, we present the mathematical model for fracture contact mechanics, poroelastic deformation of the matrix, and fluid flow. At the end of this section, we present the model for the fracture propagation process.

2.1. Geometry and primary variables

As shown in Fig. 1, we represent a fractured porous media as a two-dimensional domain Ω that is divided into a host medium, termed the matrix and denoted Ω^M, and a set of fractures that are considered to be

one-dimensional objects embedded in Ω^{M}. From here on, we will refer to both fractures and faults simply as fractures and let Ω_i^{F} denote fracture i and $\partial_k\Omega_i^{\mathrm{F}}, k=\{1,2\}$ represent the two tips of Ω_i^{F}. Throughout the paper, we assume that fractures do not intersect. Finally, we denote the interface between Ω^{M} and Ω_i^{F} by Γ_i, where, when needed, we shall represent the two sides of the interface by Γ_i^+ and Γ_i^-. The boundary of Ω^{M} that coincides with $\Gamma_i^{\pm}$ is denoted $\partial_i^{\pm}\Omega^{\mathrm{M}}$.

The primary variables are displacements, fluid pressures, contact forces on the fractures, and fluid fluxes between fractures and the matrix. Specifically, the displacements on Ω^{M} are denoted as $\mathbf{u}$, the pressure is represented by p in Ω^{M} and p_i in Ω_i^{F}, and the contact force $\mathbf{f}_i$ is defined only in Ω_i^{F}. Finally, $\mathbf{u}_i^{\pm}$ and $\lambda_i^{\pm}$ denote the displacement and fluid flux on $\Gamma_i^{\pm}$, respectively. Time derivatives are denoted by a dot, e.g., $\dot{\mathbf{u}}_i$.

2.2. Fracture contact mechanics

Let $\mathbf{n}_i$ be the normal vector to the fracture surface Ω_i^{F}, pointing from Γ_i^+ to Γ_i^-. We define the jump operator acting on $\mathbf{u}_i$ by

$$[\![\mathbf{u}_i]\!] = ([\![\mathbf{u}_i]\!]_{\mathrm{n}}, [\![\mathbf{u}_i]\!]_{\tau}) = \mathbf{u}_i^- - \mathbf{u}_i^+, \tag{1}$$

where $[\![\mathbf{u}_i]\!]_{\mathrm{n}}$ and $[\![\mathbf{u}_i]\!]_{\tau}$ denote the normal and tangential components of the displacement jump, respectively. In the normal direction, we require nonpenetration and define the normal component of the contact traction, $\mathbf{f}_{i,\mathrm{n}}$, to be negative in contact. This assumption gives rise to the KKT condition, i.e.

$$[\![\mathbf{u}_i]\!]_{\mathrm{n}} - g \geq 0, \mathbf{f}_{i,\mathrm{n}} \leq 0, ([\![\mathbf{u}_i]\!]_{\mathrm{n}} - g)\mathbf{f}_{i,\mathrm{n}} = 0. \tag{2}$$

Here, the gap function g allows the fracture to open while the walls are still in mechanical contact. We set $g = [\![\mathbf{u}_i]\!]_{\tau} \tan\psi$, with ψ being the dilation angle to let the fracture open due to tangential slip.

The tangential motion of the fracture is modeled as a frictional contact problem, with the following relation between the tangential contact traction, $\mathbf{f}_{i,\tau}$, and the change of displacement jump in time, $[\![\dot{\mathbf{u}}_i]\!]_{\tau}$:

$$\begin{aligned} &|\mathbf{f}_{i,\tau}| \leq -\mu_s \mathbf{f}_{i,\mathrm{n}}, \\ &|\mathbf{f}_{i,\tau}| < -\mu_s \mathbf{f}_{i,\mathrm{n}} \quad \text{so} \quad [\![\dot{\mathbf{u}}_i]\!]_{\tau} = 0, \\ &|\mathbf{f}_{i,\tau}| = -\mu_s \mathbf{f}_{i,\mathrm{n}} \quad \text{so} \exists \gamma \in \mathbb{R}, \mathbf{f}_{i,\tau} = -\gamma^2 [\![\dot{\mathbf{u}}_i]\!]_{\tau}. \end{aligned} \tag{3}$$

The tangential traction is bounded from above by the normal traction scaled by the friction μ_s, and when the frictional resistance is overcome, the displacement is parallel to the tangential traction.

The force balance on the fracture's surfaces is given by

$$\mathbf{n}_i \cdot \boldsymbol{\sigma}|_{\partial_i^+\Omega^{\mathrm{M}}} = \mathbf{f}_i - \alpha_i p_i(\mathbf{I}\cdot\mathbf{n}_i), -\mathbf{n}_i \cdot \boldsymbol{\sigma}|_{\partial_i^-\Omega^{\mathrm{M}}} = \mathbf{f}_i - \alpha_i p_i(\mathbf{I}\cdot\mathbf{n}_i), \tag{4}$$

where $\boldsymbol{\sigma}$ denotes the hydromechanical stress in the matrix, $\mathbf{f}_i$ is the contact traction acting on the fracture surface, and p_i is the pressure inside the fracture. The Biot coefficient in the fracture is denoted by α_i and $\mathbf{I}$ is the identity matrix. Equality should be enforced on $\Gamma_i^{\pm}$, but for notational convenience, we have suppressed projection operators. See Keilegavlen et al.[50] for more information.

2.3. Flow and poroelastic deformation of matrix

Flow and deformation in Ω^{M} are modeled by Biot theory, with the matrix taken as a linearly elastic medium. By neglecting inertial terms, the conservation of momentum and mass is governed by

$$\nabla \cdot \boldsymbol{\sigma} = \mathbf{b}, \tag{5}$$

$$\alpha \frac{\partial(\nabla\cdot\mathbf{u})}{\partial t} + M\frac{\partial p}{\partial t} - \nabla\cdot\left(\frac{\mathscr{K}}{\mu}\nabla p\right) = q, \tag{6}$$

where $\boldsymbol{\sigma}$ is the hydromechanical stress in Ω^{M}, defined by

$$\boldsymbol{\sigma} = \mathbf{C}\nabla_s\mathbf{u} - \alpha p\mathbf{I}. \tag{7}$$

Here, ∇_s represents the symmetrized gradient, $\mathbf{C}$ is the stiffness matrix, $\mathbf{b}$ denotes body forces, and q is the fluid source term. The Biot coefficient of the matrix is α, the Biot modulus is given by $M = \left(\varphi c_p + \frac{\alpha-\varphi}{K}\right)$, c_p is the fluid compressibility, φ is the matrix porosity, K is the bulk modulus, $\mathscr{K}$ denotes the permeability of the porous matrix, which is assumed to be isotropic, and μ is the fluid viscosity. On $\partial_i^{\pm}\Omega^{\mathrm{M}}$, continuity of the displacements is enforced so that $\mathrm{tr}\,\mathbf{u}|_{\partial_i^{\pm}\Omega^{\mathrm{M}}} = \mathbf{u}_i^{\pm}$, where tr is the trace operator. As seen from Ω^{M}, the interface displacement thus acts as a Dirichlet boundary condition. The interface fluid flux λ_i enters as a Neumann condition to the mass conservation equation.

2.4. Fluid flow in fractures and matrix-fracture interaction

By using the discrete fracture-matrix model, the fracture is represented explicitly in the domain. Following Stefansson et al.,[19] who extended the work of Martin et al.[51] to discrete fracture-matrix models with changing apertures, the conservation of mass in fracture i is given by

$$\frac{\partial a_i}{\partial t} + a_i c_p \frac{\partial p_i}{\partial t} - \nabla\cdot\left(\frac{\mathscr{K}_i}{\mu}\nabla p_i\right) + \left(\lambda_i^+ + \lambda_i^-\right) = q_i. \tag{8}$$

Here, we assume that the fracture can be completely occupied by the fluid, i.e., that the fracture porosity and Biot's coefficient are equal to one. $\mathscr{K}_i$ is the fracture tangential transmissivity. The aperture $a_i = a_i^0 + [\![\mathbf{u}_i]\!]_n$ is computed by a sum of an initial value a_i^0 and an update due to fracture deformation. Therefore, the first term in Eq. (8) represents volume changes due to changes in aperture. The fracture transmissivity is related to aperture by the so-called cubic law, $\mathscr{K}_i = a_i^3/12$ [52]; i.e., a_i equals the hydraulic aperture of the fracture. The term $(\lambda_i^+ + \lambda_i^-)$ represents inflow from the matrix over $\Gamma_i^{\pm}$, where $\lambda_i^{\pm}$ is the interface flux between the matrix and the fracture defined as

$$\lambda_i^{\pm} = -\kappa_i(p_i - \mathrm{tr}\,p^{\pm}), \tag{9}$$

where $\kappa_i = 2\mathscr{K}_i/(\mu a_i^2)$ is an expression of permeability normal to the fracture, $p^{\pm}$ represents pressures from the matrix at the two sides of the fracture, and it is understood that the fracture and matrix pressures should be projected onto $\Gamma_i^{\pm}$.

2.5. Fracture propagation

The propagation criterion is based on a criterion on maximum tangential stress[42] for mixed-mode fracturing. The theory postulates propagation when the maximum tangential stress in the process zone around a fracture tip exceeds a critical value. The direction of propagation is that of the maximum tangential stress. The tangential stress around a fracture tip can be expressed in polar coordinates as

$$\sigma_\theta^{\mathrm{L}}(r,\theta) = \frac{1}{\sqrt{2\pi r}}\left(K_{\mathrm{I}}\cos^3\frac{\theta}{2} - \frac{3}{2}K_{\mathrm{II}}\cos\frac{\theta}{2}\sin\theta\right) \tag{10}$$

and the crack grows in the direction θ_0 if $\sigma_\theta^{\mathrm{L}}(r,\theta_0) = \frac{K_{\mathrm{IC}}}{\sqrt{2\pi r}}$, where K_{IC} is the fracture toughness. The propagation angle is given by

$$\theta_0 = 2\tan^{-1}\left(\frac{K_{\mathrm{I}}}{4K_{\mathrm{II}}} \pm \frac{1}{4}\sqrt{\left(\frac{K_{\mathrm{I}}}{K_{\mathrm{II}}}\right)^2 + 8}\right) \tag{11}$$

subjected to a condition

$$K_{\mathrm{II}}\left(\sin\frac{\theta_0}{2} + 9\sin\frac{3\theta_0}{2}\right) < K_{\mathrm{I}}\left(\cos\frac{\theta_0}{2} + 3\cos\frac{3\theta_0}{2}\right) \tag{12}$$

where r is the distance from the tip. K_{I} and K_{II} are the stress intensity

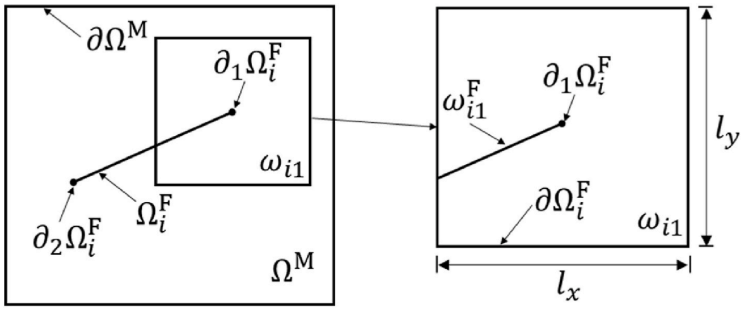

Fig. 2. Illustration of a fracture, Ω_i^{F} and a fine-level domain ω_{ik}.

factors (SIFs). The propagation length can, in general, be computed by a Paris-type law,[43] which, under the assumption that there is a single fracture inside every fine-level domain, simplifies to a propagation length equal to a preset value, $l_{\max}$. If more than one crack grows simultaneously, then the tips with the higher energy in the fracture set advance further than the others. The increment for each tip is defined by

$$l_{\mathrm{adv}}^{i} = l_{\max}\left(\frac{G_i}{\max(G_i)}\right)^{0.35} \tag{13}$$

where G_i is the energy release rate for the ith propagation crack.[53]

3. Two-level solution strategy

Our goal is to define a computational approach for the interaction between, on the one hand, deformation of fractures and domains due to hydromechanical stresses and, on the other hand, the propagation of fractures. While a fully coupled approach to the governing equations presented in the previous section is possible, it is impractical for three reasons. First, compared to the time scale of fluid flow, wing-crack propagation can be considered quasi-static and can therefore be loosely coupled to the fluid flow problem.[20,54] Second, there will be no wing-crack propagation for significant periods, and efficiency can be gained by considering only the coarse-level problem. Third, while it is critical for the propagation problem to accurately capture the stress in the vicinity of the propagating fracture, including the singularity at the tip, the mechanical response of the more expansive reservoir, including other (potentially propagating) fractures, can be given a coarser representation.

Motivated by these observations, our computational model is based on a two-level approach. We define subproblems for, on the one hand, large-scale fluid flow and deformation of fractures and the matrix, and on the other hand, fracture propagation and accompanying deformation locally around fracture tips. Reflecting the small time and length scales involved in propagation, we assign separate, small domains around each fracture tip to be used in the purely mechanical propagation calculation, referred to as the fine-level problem. Conversely, the whole simulation domain is referred to as the coarse-level domain, on which we solve the problem consisting of fluid flow and fracture and matrix deformation.

3.1. Coarse- and fine-level models

The coarse-level problem is defined on the geometry presented in Section 2, with the governing equations given by Eqs. (1)–(9), that is, frictional contact mechanics coupled with hydromechanical deformation in the matrix and on the fracture domains. Fracture propagation is not explicitly accounted for in the coarse-level model but is instead updated from the solution to the fine-level problem, as discussed in Section 3.2.

As shown in Fig. 2, the fine-level models are centered on fracture tips. With each fracture tip $\partial_k\Omega_i^{\mathrm{F}}$ in the coarse-level domain, we associate a (generally) smaller domain, termed a fine-level domain, and denoted as ω_{ik} with size $l_x \times l_y$. The fine-level domain is composed of a part of the matrix, $\omega_{ik}\subset\Omega^{\mathrm{M}}$, and a single fracture domain, ω_{ik}^{F}, which represents a part of the fracture Ω_i^{F} in the coarse-level domain. In general, $\omega_{ik}^{\mathrm{F}} \not\subset \Omega_i^{\mathrm{F}}$ since the resolution of the propagating fracture is different in the fine-level and coarse-level domains that will be discussed in Section 4. We let $\partial_i^{\pm}\omega_{ik}$ represent the two sides of the fine-level fracture while $\partial_{\mathrm{M}}\omega$ is the rest of the boundary of ω_{ik}.

In accordance with the discussion at the beginning of this section, we include the effect of fluid pressure as a body force in the fine-level model. The primary variable in the fine-level problem is, therefore, the displacement in ω_{ik}, which we represent by $\mathbf{u}^{\mathrm{L}}$ for simplicity. As with the full deformation, we assume that the fine-level matrix behaves similarly to a linearly elastic and isotropic medium governed by

$$\nabla\cdot\mathbf{c}\nabla_{\mathrm{s}}\mathbf{u}^{\mathrm{L}} = \mathbf{b} \tag{14}$$

where $\mathbf{b} = \nabla\cdot(\alpha p\mathbf{I})$ is the body force caused by pressure in the coarse-level domain. $\mathbf{c}$ is the stiffness tensor. Boundary conditions for the fine-level problem are set according to the coarse-level state, as discussed next.

3.2. Coupling between coarse-level and fine-level models

For the fine-level problem, the fracture surfaces are not allowed to move freely. Instead, their displacement is set from the coarse-level behavior close to the fracture tip. That is, the fine-level boundary condition on $\partial_i^{\pm}\omega_{ik}$ is given as a displacement jump computed from the coarse-level state,

$$[\![\mathbf{u}^{\mathrm{L}}]\!]\big|_{\partial_i^{\pm}\omega_{ik}} = \mathscr{R}\Big([\![\mathbf{u}_i]\!]\big|_{\partial_i^{\pm}\Omega^{\mathrm{M}}}\Big), \tag{15}$$

where $\mathscr{R}$ is a reconstruction operator, defined for the discrete problem in Section 4.4. On the remainder of the boundary, $\partial\omega_{ik}$, we similarly set

$$\mathbf{u}^{\mathrm{L}}\big|_{\partial\omega_{ik}} = \mathscr{R}(\mathbf{u}). \tag{16}$$

The coupling from the fine-level model to coarse-level model consists of updating the coarse-level fracture geometry based on fine-level fracture propagation. This is linked to the continuous representation of the evolving geometry in the two models. For simplicity, we will represent the fractures as piecewise linear objects with a resolution related to that of the computational grids on the two scales, as detailed in Section 4. However, to cover more advanced features, including merging of fractures and three-dimensional problems, more elaborate geometric representations are needed.[55,56]

4. Numerical approach

This section describes the building blocks of our numerical approach in terms of grids and solution approaches to coarse-level and fine-level problems, together with the two-level coupling concept.

4.1. Numerical grids for fracture propagation

We construct numerical grids to conform to fractures in both the coarse-level and fine-level domains. That is, the grids on both Ω^{M} and ω_{ik} are constructed so that fractures coincide with the paths of grid faces and then split nodes and faces along these paths, as done by Dang-Trung et al.[17] In the coarse-level domain, we further construct one-dimensional grids on Ω_i^{F}, as well as on the interfaces $\Gamma_i^{\pm}$.

Focusing on a single fine-level domain, we represent the mesh size in a fine-level grid by Δh and let ΔH represent the coarse-level mesh size around the same fracture tip. To ensure the stability of the propagation, the resolution of the fine-level domain is set to be finer than that of the coarse-level domain, i.e., $\Delta h = \varepsilon_{\mathrm{m}} \Delta H$ with $\varepsilon_{\mathrm{m}} \leq 1$. On both scales, we consider simplex grids, with the initial grids being constructed by Gmsh.[57] Updates to the fracture geometry will generally not follow existing paths of grid faces at both the fine level and coarse level. Thus, before fracture propagation on either the fine-level domain or coarse-level domain, the grid is adjusted in the vicinity region of radius $5 \times l_{\max}$ around the fracture tip with triangular rosette elements, size Δh or ΔH, to accommodate the extension of the fracture, followed by Laplacian smoothing to preserve the grid quality.[17] This technique is effective in removing degenerate and small elements. The fracture is then prolonged by splitting grid faces and nodes. For the coarse-level grid, it is further necessary to prolong the grid for the fracture domain Ω_i^{F} and the interfaces $\Gamma_i^{\pm}$ and to update the projections between the different grids.

We remark that although the grid adjustment necessitates an update of the discretization in Ω^{M}, the cost of this operation can be limited by confining the adjustment to a region close to the fracture tip.

4.2. Coarse-level discretization

The governing equations (1)–(9) on the coarse level, namely poroelastic deformation in Ω^{M} and both fluid flow and contact mechanics in Ω_i^{F} and over Γ_i are discretized and solved fully coupled by the open-source software tool PorePy.[50] The overall approach has been used before to study poroelastic[32,33] and thermoporoelastic[19] deformation coupled with fracture mechanics and has also been applied to field studies.[58]

The discretization of the frictional contact problem requires handling the discontinuity in the contact conditions Eqs. (2)–(4). These are evaluated cellwise to determine whether fractures are open or closed and, if closed, whether they are sticking or slipping; see Stefansson et al.[19] for details. This classification is employed in an active set method, where the contact conditions and balance of forces expressed are discretized according to the state from the previous iteration.[19,33,59]

The conservation equations for flow in Ω^{M} and Ω_i^{F} as well as momentum in Ω^{M} are discretized by a family of cell-centered multipoint finite volume methods developed for poroelasticity.[60,61] The methods are based on constructing discrete representations of stresses (respective fluxes) over cell faces regarding displacements (respectively pressures) in nearby cell centers. The balance of momentum and mass is enforced on the cells. For fracture domains, the method reduces to the well-known two-point flux method, which can also deal with nonplanar domains resulting from fracture propagation. Finally, the coupling between the matrix and fractures follows the scheme described by Nordbotten et al.[14] for the flow problem.

The coupled set of equations is nonlinear and requests an iteration solver due to the active set approach to the contact conditions. The system is solved by a semismooth Newton method using a direct solver for the linearized system.

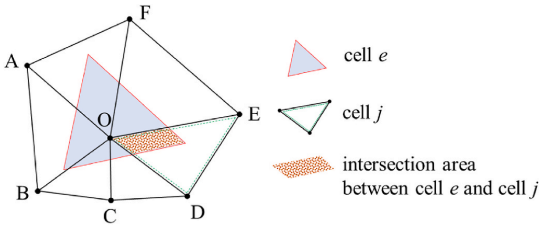

Fig. 3. Interpolation of coarse-level variables after an update of the coarse-level grid. The variables in cell e in the new grid is reconstructed from the old grid, with cells O-ABCDEF, using a nearest neighbor interpolation. The intersection area determines the weight of cell ODE to the variables for the cell e.

4.3. Fine-level discretization

While our coarse-level discretization was chosen to comply with conservation, calculations meant to decide whether a fracture will propagate, and if so, where it will go, pose different requirements on the spatial discretizations. Specifically, it is crucial to represent the stress singularity at the fracture tip. To that end, Eq. (14) is discretized by a finite element method with $\mathscr{P}_2$ basis functions. The stress singularity is captured using the nodal displacement correlation technique[62] based on quarter-point elements.[49] To enhance computational accuracy, the fine-level grid is refined and guided by residual-based a posteriori error estimates.[63] From a computed displacement field, SIFs are estimated to determine whether the fracture should propagate and, if so, in which direction.[17,62] The fine-level grid is updated as described in Section 4.1, and the displacement and pressure variables are mapped to the new grid by a $\mathscr{P}_1$ interpolation. For details of the algorithm and investigations of its performance on SIFs convergence and fracture propagation verification, we refer to Dang-Trung et al.[17]

Depending on the boundary conditions, several propagation steps may be needed to arrive at a stable state. During these iterations, the boundary conditions are fixed, consistent with the assumption that fine-level propagation is instantaneous relative to dynamics on the coarse level.

4.4. Discrete mapping between coarse-level and fine-level models

4.4.1. Mapping of variables

To couple the numerical states on the coarse-level and fine-level domains, it is necessary to project displacements from the coarse-level to fine-level domain boundaries and compress fine-level updates to the fracture geometry onto the coarse-level grid. It should be noted that, the solutions are naturally determined at the cell centers in the coarse-level grid and the nodes in the fine-level grid. Therefore, we use three processes named cell center to cell center (C2C), node to node (N2N), and cell center to node (C2N) for the mapping.

The C2C projects variables between cells in the coarse-level grid. If a fracture propagates in the coarse-level domain, the corresponding grid is locally adjusted to ensure the fracture path coincides with faces and, therefore, the variables at cell centers on the adjusted grid also need to be reconstructed. We use the natural neighbor interpolation as illustrated in Fig. 3 for this projection. We assume that new cell e interacts with old cells O-ABCDEF. The variables at the center of cell e will be reconstructed by the variables at the centers of cells O-ABCDEF, such that.

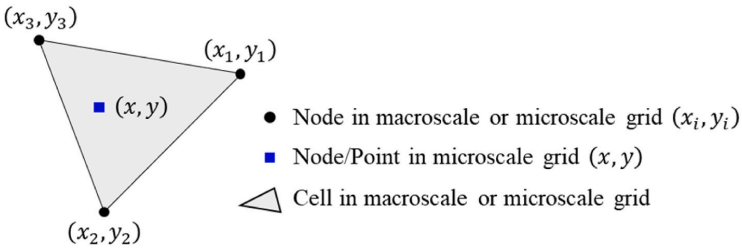

Fig. 4. The $\mathscr{P}_1$ interpolation.

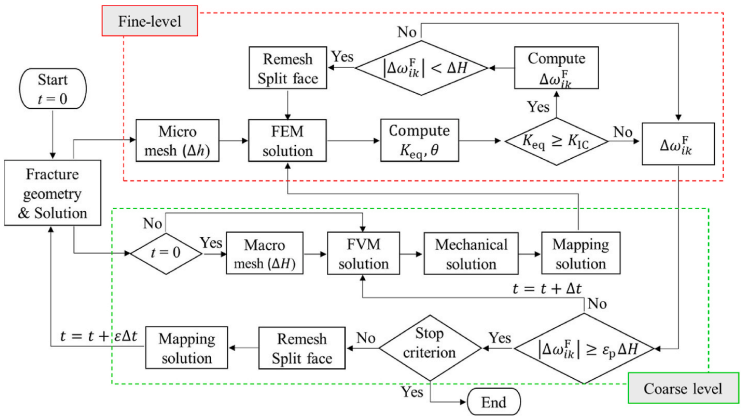

Fig. 5. Illustration of the workflow in the two-level simulation method. The simulation is controlled by the coarse-level grid size ΔH, time step size Δt, fine-level domain size l, relation between fine-level grid and coarse-level grid size ε_m and coarse-level resolution of the fracture ε_p. The details of the "Remesh/Split face" box are given in Section 4.1.

$$\xi_e = \frac{1}{\sum_{j=1}^{n} A_{ej}} \sum_{j=1}^{n} A_{ej}\xi_j, \tag{17}$$

where ξ_j denotes variables at the center of cell j, and A_{ej} is the intersection area.

The N2N projects variables from the coarse-level grid to the fine-level grid or between the fine-level grids. By the $\mathscr{P}_1$ interpolation, as illustrated by Fig. 4, variables at each point in the fine level grid can be determined through the variables at the nodes of the parent cell in either coarse-level grid or fine-level grid.

For a fine-level node with coordinates (x, y) belonging to a parent cell defined by nodes (x_i, y_i) in the coarse-level or fine-level grids, the values at (x, y) is then approximated by

$$\xi(x, y) = \sum_{i=1}^{3} N_i(x, y)\xi(x_i, y_i), \tag{18}$$

where $N_i(x, y)$ are the Lagrange basis polynomials.

The C2N projects variables from the coarse-level grid to the fine-level grid. First, the variables from the cell center are projected to the nodes of the coarse-level grid by using the natural neighbor interpolation. Then we use N2N to interpolate variables at each node of the fine-level grid.

Eq. (18) represents a discrete representation of the reconstruction operator $\mathscr{R}$ shown in Eqs. (15) and (16), i.e.,

$$\xi(x, y) = \widetilde{\mathscr{R}}\xi_j^{\text{cell-center}} \tag{19}$$

where $\widetilde{\mathscr{R}}$ is the discrete reconstruction. By Eq. (19), the values at desired fine-level points are estimated through values at cells centers in the coarse-level grid.

4.4.2. *Updating the coarse-level fracture path*

In our model, the fracture path is represented directly in the computational grid. Hence, the information transfer on the fracture path from the fine-level model to the coarse-level model is dependent on the grid resolution on the two scales. Critical for simulation efficiency, small increases in the fracture length on the fine-level domain are not immediately projected to the coarse-level problem. Instead, for a fracture propagating on the fine level, with added length $|\Delta\omega_{ik}|$, the coarse-level fracture is updated only when $|\Delta\omega_{ik}^{F}| \geq \varepsilon_p \Delta H$, where ε_p is a simulation parameter. When this threshold is overcome, the coarse-level fracture is extended by a linear approximation of $\Delta\omega_{ik}^{F}$ and the coarse-level grid is updated as discussed in Section 4.1. Thus ε_p controls both the resolution of the coarse-level grid in the vicinity of propagating fractures and the numerical coupling strength between the fine-level and coarse-level models.

4.5. *Numerical solution approach*

As a summary of the above presentation, Fig. 5 illustrates the workflow of the two-level simulation approach. The time step size is usually taken as a constant represented by Δt. However, when a fracture propagates on the coarse level, both governing equations and parameters change along the fracture path, and the coarse-level state adjusts accordingly. In particular, the fractured part of the rock experiences

Table 1
Material properties.

Parameter	Definition	Value
E	Young's modulus	40 GPa
ν	Poisson's ratio	0.2
α	Biot's coefficient in the matrix	0.8
φ	Material porosity	0.01
c_p	Fluid compressibility	$4.0 \times 10^{-10}\text{Pa}^{-1}$
$\mathscr{K}$	Matrix permeability	$5.0 \times 10^{-20}\text{m}^2$
μ	Viscosity	1.0×10^{-4} Pa • s
μ_s	Friction coefficient	0.5
ψ	Dilation angle	1°

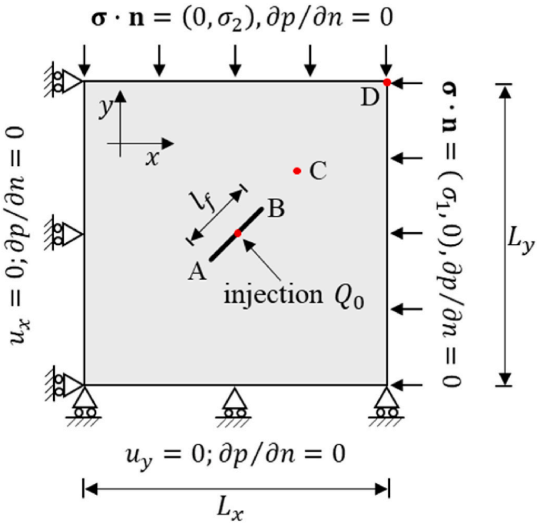

Fig. 6. Model of a porous media with a single fracture subjected to a principal stress regime.

enhanced permeability and volume available for fluids. The pressure field in the vicinity of the tip will adjust to the new parameters on a time scale that is much shorter than that of pressure diffusion related to the injection. We capture this effect by temporarily reducing the time step size with a factor $\varepsilon = 10^{-2}$ until this rapid dynamics is resolved and the pressure field near the crack tip is stabilized, whereupon we continue with the standard step size.

5. Results

The correctness of either the fine-level model or coarse-level model has been verified in previous studies.[5,17,19,33] This section, therefore, is devoted to the presentation of numerical experiments of the fully coupled model. The coarse-level problem alone may strain the available computational resources in application-oriented simulations with large domains and multiple fractures. Therefore, it is paramount to limit the additional computational cost to incorporate fracture propagation in such simulations. We have devised a suite of numerical experiments designed to investigate the stability, accuracy, and computational efficiency of the proposed numerical approach. Specifically, we study how the prediction of the fracture path is altered under variations in the size of the fine-level domain ($l = l_x = l_y$), the mesh size on the fine-level (Δh) and coarse-level (ΔH) domains, the time step size (Δt), and the threshold for updating the coarse-level geometry (ε_p). Together, these simulation parameters determine the balance between solution accuracy and computational cost. As our motivation is to allow simulations on large domains where high-resolution simulations are not feasible, our focus is not on the convergence of the numerical solution but rather its stability as the resolution in time and space are coarsened. Based on observations from these tests, we finally present a complex case of hydromechanical processes interacting with the deformation and propagation of multiple pre-existing fractures in a synthetic subsurface fluid injection scenario. The source code for the following simulations is open access.[64]

5.1. Onset of fracture

We first investigate how the onset of fracturing, determined by SIFs, is influenced by the size of the time step, coarse-level grid, and fine-level domain. To that end, we consider a porous media domain assumed to be homogenous and linearly elastic with the material properties given in Table 1. The geometry and boundary conditions of the model are

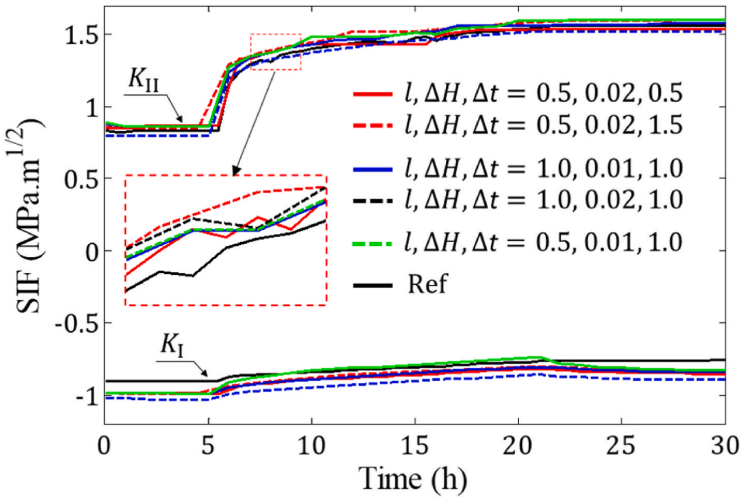

Fig. 7. Stress intensity factors at tip A obtained by different microdomain sizes l (m), mesh sizes ΔH (m), and time steps Δt (h).

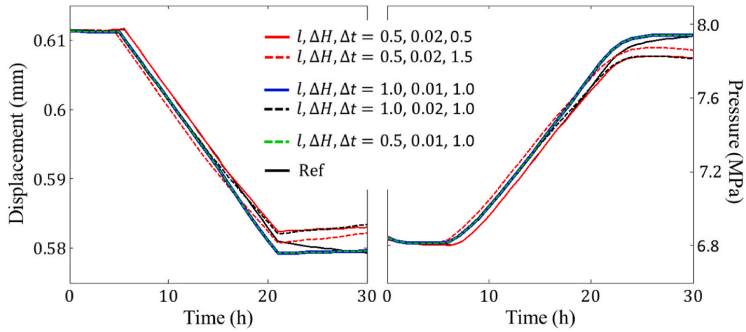

Fig. 8. Displacement at point D and pressure at point C obtained by different microdomain sizes$l$ (m), mesh sizes ΔH (m), and time steps Δt (h).

illustrated in Fig. 6, in which $L_x = L_y = 2$ m. A single fracture of length $l_f = 0.1$ m and initial aperture $a^0 = 1$ mm is located at the center of the computational domain and oriented at 45° to the positive x-direction. The left and bottom boundaries are fixed in the x- and y-directions, respectively, and the top and right boundaries are free. The fluid is not allowed to flow through boundaries. The fractured porous media is subject to a stress state with the maximum horizontal stress $\sigma_1 = 20$ MPa and the minimum vertical stress $\sigma_2 = 10$ MPa, imposed orthogonally to the domain along the x- and y-directions, respectively. Water is injected into the pre-existing fracture after 6 h (h) and continuously for 15 h at a constant rate of $Q_0 = 5 \times 10^{-9}\mathrm{m}^2/\mathrm{s}$.

The effects of the time step (Δt), size of the fine-level domain(l), and mesh size (ΔH) on SIFs, displacement, and pressure are considered. Two levels of the fine-level domain size are considered, i.e., $l = 0.5$ m or 1.0 m. The resolutions of the fine-level and coarse-level domains are the same, i.e., $\varepsilon_{\mathrm{m}} = 1.0$, and we consider two different levels: $\Delta H = \Delta h =$ 0.01 m or 0.02 m. Three levels of time steps are used: $\Delta t =$ 0.5 h, 1.0 h, or 1.5 h. Because of the lack of experimental data and exact solutions, the results from a computational setup are chosen as the reference. In the reference setup, the fine-level domain coincides with the coarse-level domain, i.e., $l = L$, and they are similar in resolution, i.e., $\Delta H =$ $0.01\ \mathrm{m}, \varepsilon_{\mathrm{m}} = 1.0$. We also use a small-time step, i.e., $\Delta t = 0.5$ h, in this setup.

The SIFs at tip A, pressure at point C $= (1.5, 1.5)$, and displacement at point D $= (2, 2)$ obtained by different fine-level domain sizes, mesh sizes, and time steps are shown in Figs. 7 and 8. There are no significant differences in the solutions obtained by using a small fine-level domain compared to using a larger domain for a given mesh size ΔH. In addition, the resolution of meshes and time steps have little effect on the solution. These agreements indicate that the calculation of SIFs is stable for the considered time steps, fine-level domain sizes, and mesh sizes.

The injection at a low rate gradually builds up pressure, causing slip of the pre-existing fracture and shear failure instead of tensile failure at the fracture tip. As shown in Fig. 7, the injection increases K_{II} from 0.79 MPa • $\mathrm{m}^{1/2}$ to 1.47 MPa • $\mathrm{m}^{1/2}$, while there is almost no effect on K_{I}. This is the result of the gradual reduction of the contact traction at the pre-existing fracture during the injection. In addition, the injection also increases pore pressure and resists deformation of the domain caused by compression. As shown in Fig. 8, the pore pressure at point C and displacement at point D are 6.8 MPa and 0.63 mm, respectively, at the beginning of the injection. After 15 h of injection, pressure increases to 8.0 MPa and displacement decreases to 0.60 mm. Termination of injection keeps the pore pressure and displacement stable.

5.2. Wing-crack propagation caused by fluid injection

Next, we consider further aspects of the model and solution strategy by studying the initiation and propagation of wing cracks from the ends of a pre-existing fracture caused by gradual pressure build-up by fluid injection at a low rate. The problem geometry, boundary conditions, and material parameters are the same as in the previous example. The fracture toughness is $K_{\mathrm{IC}} = 0.7$ MPa • $\mathrm{m}^{1/2}$. Water is injected at a constant rate of $Q_0 = 5 \times 10^{-9}\mathrm{m}^2/\mathrm{s}$ into the pre-existing fracture during the simulation. The simulation is stopped when the wing crack propagating from tip A reaches a length of 0.25 m. To facilitate comparison between different sets of simulations, a reference case is computed with the same simulation parameters as used for the reference in Section 5.1, where we additionally use a threshold of $\varepsilon_{\mathrm{p}} = 0.5$ for the coarse-level propagation of the fracture.

5.2.1. Simulation study of coupled physics

We start by illustrating the capacity of the present model to capture

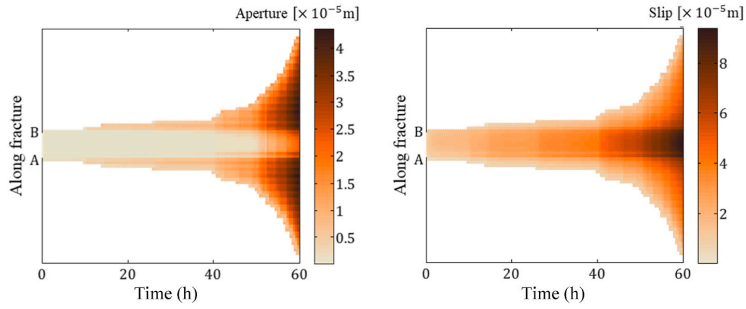

Fig. 9. Aperture expansion and shear slip at the fracture during simulation.

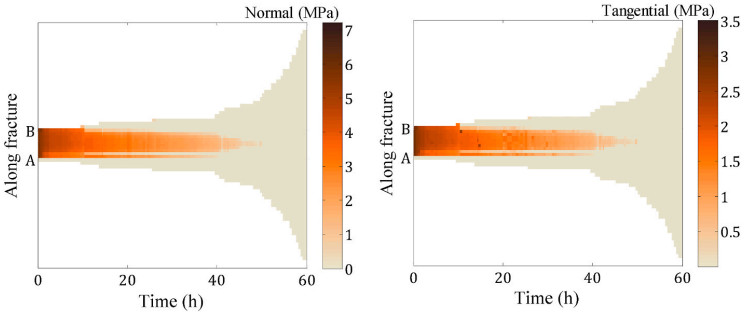

Fig. 10. Normal and tangential tractions at the fracture during simulation.

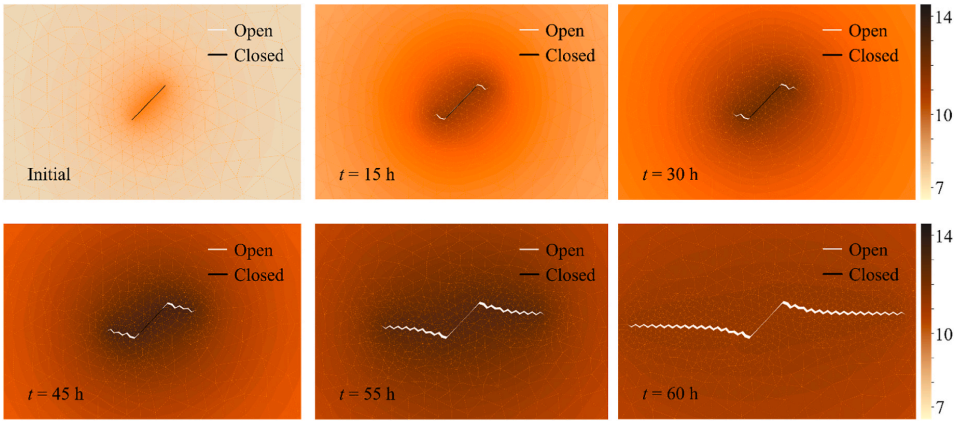

Fig. 11. Fracture propagation and pressure evolution in a 2D porous media during the fluid injection into the pre-existing fracture. Solid white/black lines denote fractures. The color bar represents pore pressure (MPa). (For interpretation of the references to color in this figure legend, the reader is referred to the Web version of this article.)

the complex coupled physics involved in fracture deformation and propagation based on a study of results from the reference case. Figs. 9 and 10 show the aperture expansion, shear slip, and contact traction of the fracture during the simulation. The fracture slowly extends in the first 40 h, but then it suddenly increases more quickly. Due to injection at a relatively low rate and low permeability of the matrix, pressure takes time to build up in the porous media domain. This process gradually reduces the fracture contact traction and causes small slips on the fracture surface, but the fracture is still in contact. The small slip causes slight growth along the pre-existing fracture. After approximately 40 h of injection, the fluid pressure is sufficiently elevated in the domain to decrease the contact traction and induce slip in larger regions of the pre-

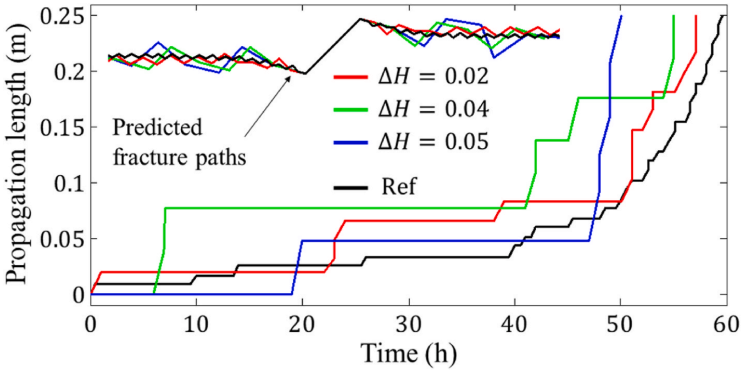

Fig. 12. The propagation length (m) from tip A and predicted fracture paths obtained by different resolutions ΔH (m) for $l = L$, $\varepsilon_p = 1.0$, and $\Delta t = 1.0$ h.

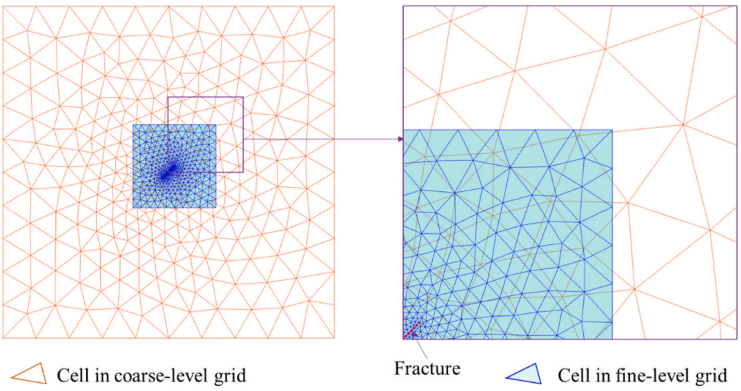

Fig. 13. The overlapping between coarse-level grid and fine-level grid for case $\Delta H = 0.02$, $l = 0.5$, and $\varepsilon_m = 0.25$.

existing fracture, leading to the further propagation of wing cracks. Finally, the contact traction goes to zero along the initial fracture, leading to its complete opening and rapid propagation.

The fracture geometry and surrounding pore pressure for the simulations are shown in Fig. 11. First, the slip of fracture faces triggers wing cracks to initiate from the tips. Then, fractures slowly propagate toward the maximum horizontal stress direction (the x-direction) during the first 40 h. High fluid pressure mainly occurs along the pre-existing fracture due to the low permeability of the surrounding porous medium. After that, the fracture extension makes fluid pressure propagate further in the domain while injection continues to elevate the pressure. This process reduces contact traction and causes the fracture to grow farther.

In the first 10 h, pressure and slip in the injected fracture increase gradually, but not enough to trigger the fracture to propagate. So, the coarse-level computational grid and solution are preserved. After that, wing cracks emerge and require the grid adjustment, followed by the update of the solution.

5.2.2. *Effect of coarse-level grid resolution*

To probe the robustness of the two-level simulation approach, we first investigate the effect of coarse-level grid resolution on predicting the speed of fracture growth and fracture paths. In this example, the fine-level grid coincides with the coarse-level grid, i.e., $l = L$, and $\varepsilon_m =$ 1.0, while the time step is $\Delta t = 1.0$ h. A comparison of predictions obtained by different resolutions is shown in Fig. 12, in which black lines represent a prediction based on the computational reference.

For all grid resolutions, the wing cracks propagate in the direction normal to the least principal stress, although the fracture paths can be seen to meander, particularly for the coarser grids. The propagation speed is initially stable with small increments in fracture size, followed by accelerated propagation starting at 40–50 h for the different grid resolutions. The results are in relatively good agreement in the first period, although the timing of the propagation events varies between the grid resolutions. The results differ more in the acceleration period, with the coarsest resolution ($\Delta H = \Delta h = 0.05$ m) showing almost brutal fracturing compared with the gradual although accelerating speed for the solutions obtained on the more refined grids. This is not unexpected since fast propagation is hard to capture, particularly for coarse grid resolutions. The example thus illustrates the balance between accuracy and computational cost and underlines the need to adapt and refine the coarse-level grid in the vicinity of a propagating fracture tip.

5.2.3. *Effect of fine-level domain size and grid resolution*

Next, we consider the impact of seeking computational savings in the fine-level problem by assigning a smaller fine-level domain size l and different resolutions in the fine-level grids. We fix the time step to $\Delta t =$ 1.0 h and set the resolution of the coarse-level domain and propagation

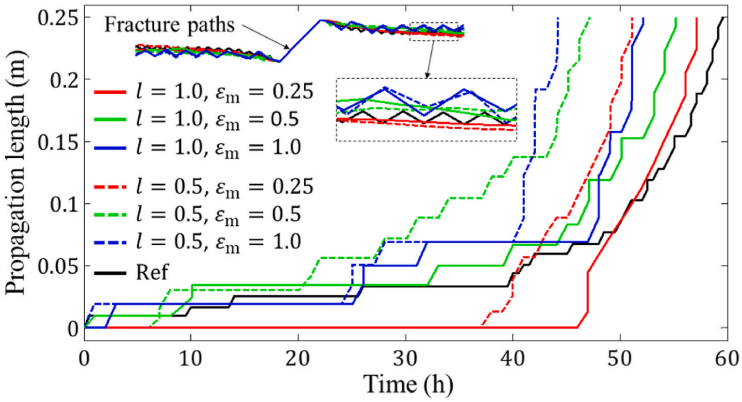

Fig. 14. The propagation length from tip A and fracture paths obtained by different sizes of the fine-level domain, l (m), and resolutions of the fine-level domain, ε_m, for $\Delta H = 0.02\,m, \Delta t = 1.0\,h,$ and $\varepsilon_p = 0.5$.

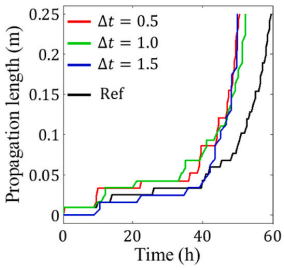

a) Effect of time step Δt (h) for $l = 1.0$ m, $\Delta H = 0.01$ m, $\varepsilon_m = 1.0$, and $\varepsilon_p = 1.0$

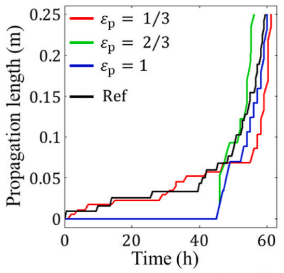

b) Effect of propagation threshold ε_p for $l =$ 1.0 m, $\Delta H = 0.02$ m, $\varepsilon_m = 1/3$, and $\Delta t = 1.0$ h

Fig. 15. The propagation length from tip A obtained by different resolutions, fine-level domain sizes, time steps, and propagation thresholds.

threshold to $\Delta H = 0.02$ m and $\varepsilon_p = 0.5$, respectively. The failure criterion is evaluated from a solution to the fine-level problem on a domain surrounding the fracture tip. The mesh for case $\Delta H = 0.02$, $l = 0.5$, and $\varepsilon_m = 0.25$ is shown in Fig. 13.

The effect of the fine-level domain size, l, and the resolution, $\Delta h = \varepsilon_m \Delta H$, of this fine-level domain on the propagation speed and fracture path is shown in Fig. 14. Again, the calculated fracture paths meander for the coarser grid, but this effect abates with the refinement of the fine-level grid. In terms of propagation speed, the simulations again show a transition from stable to accelerating propagation. Except for ε_m in the period from approximately 8 h–20 h after the start of the injection, the propagation speed is always larger for the smaller fine-level domains. As the boundary conditions for the fine-level problem are fixed by the coarse-level state, the smaller domains must absorb the energy from fracture sliding in a smaller rock volume, increasing the stresses in the vicinity of the tip. The severity of this effect should, to a large degree, be independent of the size of the coarse-level domain, and thus, using only somewhat larger fine-level domains should also be feasible for larger problems.

The impact of varying the fine-level mesh size is less clear. The results obtained on the two coarser fine-level grids, $\varepsilon_m = 0.5$ and $\varepsilon_m = 1.0$, are in broad agreement in the period of stable propagation but exhibit notable differences when transitioning to an accelerating regime. The results from the finest fine-level grid do not show a period of stable propagation on the coarse-level grid but instead enter the period of acceleration directly, at approximately the same time as the other simulations. This disagrees with the other results, notably the observation in Fig. 7 that the critical threshold for K_{II} is crossed approximately 7 h after the start of injection. A possible explanation is that the relatively large difference in mesh size between the fine-level and coarse-level problems for this value of ε_m makes the fracture propagate on the fine level without this effect being captured on the coarse-level domain.

5.2.4. *Effect of discretization coupling parameters: time-step size and coarse-level propagation threshold*

The effects of time step and threshold to extend fracture in the coarse-level domain are investigated in this example. For the time step study, as shown in Fig. 15 (a), we fix the size of the fine-level domain and mesh resolutions, i.e., $l = 1.0$ m and $\Delta H = \Delta h = 0.01$ m, and consider three levels of the time step, i.e., $\Delta t = 0.5$ h, 1.0 h, or 1.5 h. The method can be seen to be stable under this variation with a similar speed of fracture propagation in all three cases. The difference from the reference case can be attributed to the smaller size of the fine-level domain.

Besides, we also consider how the coarse-level propagation threshold, ε_p, affects the propagation speed, as shown in Fig. 15 (b). In this case, we set $l = 1.0$ m, $\Delta H = 0.02$ m, $\Delta t = 1.0$ h, and $\varepsilon_m = 1/3$ and assign three different values for ε_p, namely, $1/3$, $2/3$, or 1. For the two highest values of ε_p, i.e., $2/3$ and 1, there is no period of stable propagation on the coarse level but rather an abrupt transition to the accelerating regime. This is like the results reported in Fig. 14, which also had a small value of $\varepsilon_m = 1/4$. Using a small value for ε_p also compensates for this effect.

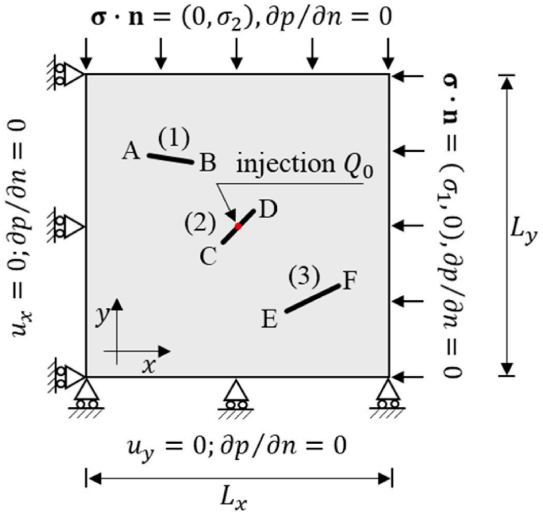

Fig. 16. Model of three fractures in a porous media subject to boundary conditions.

The findings of these experiments are summarized as follows. First, the direction of propagation is mainly controlled by boundary conditions. However, the computed fracture path tends to wiggle unless a relatively fine grid is applied on the fine-level domain. Such refined grids may again lead to delayed propagation on the coarse-level grid unless the fine-level and coarse-level problems are tightly coupled through the parameter ε_p. Second, the size of the fine-level domain can be reduced to lower the computational cost. However, a microdomain that is too small can overestimate the propagation speed. Finally, the time step size had little impact on the results for the cases we considered.

5.3. *Extension: propagation of multiple fractures under fluid injection*

Finally, to show the power of the proposed approach, hydromechanical processes interacting with the deformation and propagation of three pre-existing fractures in porous media are studied. The geometry and boundary conditions are illustrated in Fig. 16, in which $L_x = L_y =$

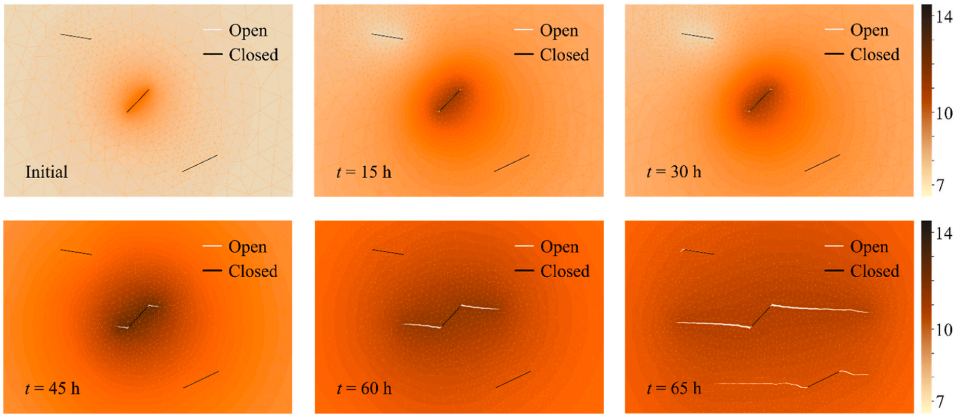

Fig. 17. Propagation of multiple fractures and evolution of pressure in a 2D porous media during fluid injection into one pre-existing fracture. Solid white/black lines denote fractures. The color bar represents pore pressure (MPa). (For interpretation of the references to color in this figure legend, the reader is referred to the Web version of this article.)

2 m. There are three fractures with the same initial aperture, $a_i^0 = 1$ mm, pre-existing in the domain. Fracture 1 is defined by endpoints A = $(0.751, 1.208)$ and B = $(0.849, 1.192)$, fracture 2 by endpoints C = $(0.965, 0.965)$ and D = $(1.035, 1.035)$, and fracture 3 by endpoints E = $(1.144, 0.780)$ and F = $(1.256, 0.831)$. Water is injected at a constant rate of $Q_0 = 5 \times 10^{-9}\text{m}^2/\text{s}$ into fracture 2 during the simulation. The material parameters are the same as for the example in Section 5.2. The simulation is implemented based on the two-level model, in which $l = 0.5$ m, $\Delta H = 0.02$ m, $\varepsilon_\text{m} = 0.5$, $\varepsilon_\text{p} = 0.5$, and $\Delta t = 1$ h.

The evaluation of the fracture geometry and the pore pressure is shown in Fig. 17. As in the above example, wing cracks mainly initiate and propagate from the fracture where fluid is injected. Small wing cracks are also observed from the other pre-existing fractures and are caused mainly by mechanical effects, i.e., the deformation of the domain. The fractures where fluid is injected propagate as a consequence of the hydromechanical stresses induced by the fluid injection, and fluid infiltrates farther into the domain as the fracture grows. These processes take place at the same time, leading the fracture to grow increasingly faster. In addition to the fracture growth, the injection also stimulates the nearby fracture to propagate.

6. Conclusion

This work presented a mathematical model and a numerical solution for coupling fluid flow, matrix deformation, fracture slip, and fracture propagation in porous media due to fluid injection. The governing mathematical model is based on Biot's model, with the deformation of existing fractures represented by contact mechanics. The maximum tangential stress criterion is combined with Paris' law to govern the fracture growth processes. A two-level simulation approach was presented, that employs a novel combination of finite volume methods for the poroelastic deformation of existing fractures with a finite element approach for the fracture propagation process.

The two-level approach allows for balancing between computational cost and simulation accuracy by varying the coupling between the coarse-level and fine-level models; tuning of the coupling strength should be done with respect to the problem to be solved, but also the computational resources available. The verifications in this paper show that the proposed approach is stable with different time steps, coarse-level grid sizes, and fine-level grid sizes. This approach is capable of simulating complex problems, such as the simultaneous propagation of multiple fractures combined with the slip and dilation of fractures in contact and tensile opening. Hydraulically and mechanically interacting fractures are handled naturally. Therefore, the current model has potential in the simulation of mixed-mechanism hydraulic stimulation of fractured reservoirs, in which both fracture shearing and corresponding wing-crack propagation lead to an increase in permeability.

Declaration of competing interest

The authors declare that they have no known competing financial interests or personal relationships that could have appeared to influence the work reported in this paper.

Data availability

The source code for this research can be found at: https://doi.org/10.5281/zenodo.5642548

Acknowledgments

This project has received funding from the European Research Council (ERC) under the European Union's Horizon 2020 research and innovation programme (grant agreement No 101002507).

References

1 Schoenball M, Ajo-Franklin JB, Blankenship D, et al. Creation of a mixed-mode fracture network at mesoscale through hydraulic fracturing and shear stimulation. *J Geophys Res Solid Earth*. 2020;125(12), e2020JB019807. https://doi.org/10.1029/2020JB019807.

2 McClure MW, Horne RN. An investigation of stimulation mechanisms in Enhanced Geothermal Systems. *Int J Rock Mech Min Sci*. 2014;72:242–260. https://doi.org/10.1016/j.ijrmms.2014.07.011.

3 Jung R. Egs — goodbye or back to the future. In: *Effective and Sustainable Hydraulic Fracturing*. InTech; 2013:95–121. https://doi.org/10.5772/56458.

4 Rutqvist J, Stephansson O. The role of hydromechanical coupling in fractured rock engineering. *Hydrogeol J*. 2003;11(1):7–40. https://doi.org/10.1007/S10040-002-0241-5.

5 Berre I, Stefansson I, Keilegavlen E. Fault slip in hydraulic stimulation of geothermal reservoirs: governing mechanisms and process-structure interaction. *Lead Edge*. 2020;39(12):893–900. https://doi.org/10.1190/tle39120893.1.

6 Pine RJ, Batchelor AS. Downward migration of shearing in jointed rock during hydraulic injections. *Int J Rock Mech Min Sci Geomech Abstracts*. 1984;21(5):249–263. https://doi.org/10.1016/0148-9062(84)92681-0.

7 Berre I, Doster F, Keilegavlen E. Flow in fractured porous media: a review of conceptual models and discretization approaches. *Transport Porous Media*. 2019;130(1):215–236. https://doi.org/10.1007/s11242-018-1171-6.

8 Salimzadeh S, Khalili N. A fully coupled XFEM model for flow and deformation in fractured porous media with explicit fracture flow. *Int J GeoMech*. 2015. https://doi.org/10.1061/(ASCE)GM.1943-5622.0000623. Published online December 1.

9 Khoei AR, Vahab M, Haghighat E, Moallemi S. A mesh-independent finite element formulation for modeling crack growth in saturated porous media based on an enriched-FEM technique. *Int J Fract*. 2014;188(1):79–108. https://doi.org/10.1007/s10704-014-9948-2.

10 Mohammadnejad T, Khoei AR. An extended finite element method for hydraulic fracture propagation in deformable porous media with the cohesive crack model. *Finite Elem Anal Des*. 2013;73(Supplement C):77–95. https://doi.org/10.1016/j.finel.2013.05.005.

11 Lecampion B. An extended finite element method for hydraulic fracture problems. *Commun Numer Methods Eng*. 2009;25(2):121–133. https://doi.org/10.1002/cnm.1111.

12 Shi F, Wang X, Liu C, he Liu, Wu H. An XFEM-based method with reduction technique for modeling hydraulic fracture propagation in formations containing frictional natural fractures. *Eng Fract Mech*. 2017;173. https://doi.org/10.1016/j.engfracmech.2017.01.025.

13 Khoei AR, Hirmand M, Vahab M, Bazargan M. An enriched FEM technique for modeling hydraulically driven cohesive fracture propagation in impermeable media with frictional natural faults: numerical and experimental investigations. *Int J Numer Methods Eng*. 2015;104(6):439–468. https://doi.org/10.1002/nme.4944.

14 Nordbotten JM, Boon WM, Fumagalli A, Keilegavlen E. Unified approach to discretization of flow in fractured porous media. *Comput Geosci*. 2019;23(2):225–237. https://doi.org/10.1007/s10596-018-9778-9.

15 Mikelić A, Wheeler M, Wick T. A phase-field method for propagating fluid-filled fractures coupled to a surrounding porous medium. *Multiscale Model Simul*. 2015;13(1):367–398. https://doi.org/10.1137/140967118.

16 Franceschini A, Castelletto N, White JA, Tchelepi HA. Algebraically stabilized Lagrange multiplier method for frictional contact mechanics with hydraulically active fractures. *Comput Methods Appl Mech Eng*. 2020;368, 113161. https://doi.org/10.1016/j.cma.2020.113161.

17 Dang-Trung H, Keilegavlen E, Berre I. Numerical modeling of wing crack propagation accounting for fracture contact mechanics. *Int J Solid Struct*. 2020;204–205:233–247. https://doi.org/10.1016/j.ijsolstr.2020.08.017.

18 Gallyamov E, Garipov T, Voskov D, van den Hoek P. Discrete fracture model for simulating waterflooding processes under fracturing conditions. *Int J Numer Anal Methods GeoMech*. 2018;42(13):1445–1470. https://doi.org/10.1002/nag.2797.

19 Stefansson I, Berre I, Keilegavlen E. A fully coupled numerical model of thermo-hydro-mechanical processes and fracture contact mechanics in porous media. *Comput Methods Appl Mech Eng*. 2021;386, 114122. https://doi.org/10.1016/j.cma.2021.114122.

20 Adachi J, Siebrits E, Peirce A, Desroches J. Computer simulation of hydraulic fractures. *Int J Rock Mech Min Sci*. 2007;44(5):739–757. https://doi.org/10.1016/j.ijrmms.2006.11.006.

21 Weng X, Kresse O, Cohen C, Wu R, Gu H. Modeling of hydraulic fracture network propagation in a naturally fractured formation. *All Days*. 2011;24. https://doi.org/10.2118/140253-MS. Published online January.

22 Miehe C, Mauthe S, Teichtmeister S. Minimization principles for the coupled problem of Darcy–Biot-type fluid transport in porous media linked to phase field modeling of fracture. *J Mech Phys Solid*. 2015;82:186–217. https://doi.org/10.1016/j.jmps.2015.04.006.

23 Detournay E. Mechanics of hydraulic fractures. *Annu Rev Fluid Mech*. 2016;48(1):311–339. https://doi.org/10.1146/annurev-fluid-010814-014736.

24 Salimzadeh S, Usui T, Paluszny A, Zimmerman RW. Finite element simulations of interactions between multiple hydraulic fractures in a poroelastic rock. *Int J Rock Mech Min Sci*. 2017;99:9–20. https://doi.org/10.1016/j.ijrmms.2017.09.001.

25 Settgast RR, Fu P, Walsh SDC, White JA, Annavarapu C, Ryerson FJ. A fully coupled method for massively parallel simulation of hydraulically driven fractures in 3-dimensions. *Int J Numer Anal Methods GeoMech*. 2017;41(5):627–653. https://doi.org/10.1002/nag.2557.

26 Santillán D, Juanes R, Cueto-Felgueroso L. Phase field model of hydraulic fracturing in poroelastic media: fracture propagation, arrest, and branching under fluid injection and extraction. *J Geophys Res Solid Earth*. 2018;123(3):2127–2155. https://doi.org/10.1002/2017JB014740.

27 Gao Y, Detournay E. Hydraulic fracture induced by water injection in weak rock. *J Fluid Mech*. 2021, 927:A19. https://doi.org/10.1017/jfm.2021.770.

28 Carrier B, Granet S. Numerical modeling of hydraulic fracture problem in permeable medium using cohesive zone model. *Eng Fract Mech*. 2012;79:312–328. https://doi.org/10.1016/j.engfracmech.2011.11.012.

29 Boone TJ, Ingraffea AR. A numerical procedure for simulation of hydraulically-driven fracture propagation in poroelastic media. *Int J Numer Anal Methods GeoMech*. 1990;14(1):27–47. https://doi.org/10.1002/nag.1610140103.

30 Detournay E. Propagation regimes of fluid-driven fractures in impermeable rocks. *Int J GeoMech*. 2004;4(1):35–45. https://doi.org/10.1061/(ASCE)1532-3641(2004)4:1(35).

31 Lecampion B, Bunger A, Zhang X. Numerical methods for hydraulic fracture propagation: a review of recent trends. *J Nat Gas Sci Eng*. 2017;49. https://doi.org/10.1016/j.jngse.2017.10.012.

32 Berre I, Stefansson I, Keilegavlen E. Fault slip in hydraulic stimulation of geothermal reservoirs: governing mechanisms and process-structure interaction. *arXiv: Geophysics*. 2020. https://doi.org/10.1190/tle39120893.1. Published online August 25.

33 Berge RL, Berre I, Keilegavlen E, Nordbotten JM, Wohlmuth B. Finite volume discretization for poroelastic media with fractures modeled by contact mechanics. *Int J Numer Methods Eng*. 2020;121(4):644–663. https://doi.org/10.1002/nme.6238.

34 McClure MW, Horne RN. Investigation of injection-induced seismicity using a coupled fluid flow and rate/state friction model. *Geophysics*. 2011;76(6):WC181–WC198. https://doi.org/10.1190/geo2011-0064.1.

35 Ghassemi A, Zhou X. A three-dimensional thermo-poroelastic model for fracture response to injection/extraction in enhanced geothermal systems. *Geothermics*. 2011;40(1):39–49. https://doi.org/10.1016/j.geothermics.2010.12.001.

36 Baisch S, Vörös R, Rothert E, Stang H, Jung R, Schellschmidt R. A numerical model for fluid injection induced seismicity at Soultz-sous-Forêts. *Int J Rock Mech Min Sci*. 2010;47(3):405–413. https://doi.org/10.1016/j.ijrmms.2009.10.001.

37 Nguyen TS, Selvadurai APS. A model for coupled mechanical and hydraulic behaviour of a rock joint. *Int J Numer Anal Methods GeoMech*. 1998;22:29–48.

38 Stefansson I, Keilegavlen E, Halldórsdóttir S, Berre I. *Numerical Modelling of Convection-Driven Cooling, Deformation and Fracturing of Thermo-Poroelastic Media*. Transp Porous Media; 2021. https://doi.org/10.1007/s11242-021-01676-1. Published online December.

39 Yan C, Fan H, Huang D, Wang G. A 2D mixed fracture–pore seepage model and hydromechanical coupling for fractured porous media. *Acta Geotech*. 2021;16(10):3061–3086. https://doi.org/10.1007/s11440-021-01183-z.

40 Yan C, Jiao YY. A 2D fully coupled hydro-mechanical finite-discrete element model with real pore seepage for simulating the deformation and fracture of porous medium driven by fluid. *Comput Struct*. 2018;196:311–326. https://doi.org/10.1016/j.compstruc.2017.10.005.

41 Yan C, Jiao YY, Zheng H. A fully coupled three-dimensional hydro-mechanical finite discrete element approach with real porous seepage for simulating 3D hydraulic fracturing. *Comput Geotech*. 2018;96:73–89. https://doi.org/10.1016/j.compgeo.2017.10.008.

42 Erdogan F, Sih GC. On the crack extension in plates under plane loading and transverse shear. *J Basic Eng*. 1963;85(4):519–525. https://doi.org/10.1115/1.3656897.

43 Paris P, Erdogan F. A critical analysis of crack propagation laws. *J Fluid Eng*. 1963;85(4):528–533. https://doi.org/10.1115/1.3656900.

44 Haeri H, Shahriar K, Fatehi Marji M, Moarefvand P. Experimental and numerical study of crack propagation and coalescence in pre-cracked rock-like disks. *Int J Rock Mech Min Sci*. 2014;67:20–28. https://doi.org/10.1016/j.ijrmms.2014.01.008.

45 E W, Engquist B. The heterogeneous multi scale methods. *Commun Math Sci*. 2003;1:87–132.

46 Dhia H ben. Global-local approaches: the Arlequin framework. *Eur J Comput Mech*. 2006;15(1-3):67–80. https://doi.org/10.3166/remn.15.67-80.

47 Feyel F. A multilevel finite element method (FE2) to describe the response of highly non-linear structures using generalized continua. *Comput Methods Appl Mech Eng*. 2003;192:3233–3244. https://doi.org/10.1016/S0045-7825(03)00348-7.

48 Abdulle A, Weinan E, Engquist B, Vanden-Eijnden E. The heterogeneous multiscale method. *Acta Numer*. 2012;21:1–87. https://doi.org/10.1017/S0962492912000025.

49 Barsoum RS. Triangular quarter-point elements as elastic and perfectly-plastic crack tip elements. *Int J Numer Methods Eng*. 1977;11(1):85–98. https://doi.org/10.1002/nme.1620110109.

50 Keilegavlen E, Berge R, Fumagalli A, et al. PorePy: an open-source software for simulation of multiphysics processes in fractured porous media. *Comput Geosci*. 2021;25(1):243–265. https://doi.org/10.1007/s10596-020-10002-5.

51 Martin V, Jaffré J, Roberts J. Modeling fractures and barriers as interfaces for flow in porous media. *SIAM J Sci Comput*. 2005;26:1667–1691. https://doi.org/10.1137/S1064827503429363.

52 Zimmerman RW, Bodvarsson GS. Hydraulic conductivity of rock fractures. *Transport Porous Media*. 1996;23(1):1–30. https://doi.org/10.1007/BF00145263.

53 Anderson TL. *Fracture Mechanics: Fundamentals and Applications*. fourth ed. CRC Press; 2017.

54 Kim J, Moridis GJ. Development of the T+M coupled flow–geomechanical simulator to describe fracture propagation and coupled flow–thermal–geomechanical processes in tight/shale gas systems. *Comput Geosci*. 2013;60:184–198. https://doi.org/10.1016/j.cageo.2013.04.023.

55 Paluszny A, Matthäi SK. Numerical modeling of discrete multi-crack growth applied to pattern formation in geological brittle media. *Int J Solid Struct*. 2009;46(18):3383–3397. https://doi.org/10.1016/j.ijsolstr.2009.05.007.

56 Paluszny A, Zimmerman RW. Numerical simulation of multiple 3D fracture propagation using arbitrary meshes. *Comput Methods Appl Mech Eng*. 2011;200(9):953–966. https://doi.org/10.1016/j.cma.2010.11.013.

57 Geuzaine C, Remacle JF. Gmsh: a 3-D finite element mesh generator with built-in pre- and post-processing facilities. *Int J Numer Methods Eng*. 2009;79(11):1309–1331. https://doi.org/10.1002/nme.2579.

58 Keilegavlen E, Duboeuf L, Dichiarante AM, et al. Hydro-mechanical simulation and analysis of induced seismicity for a hydraulic stimulation test at the Reykjanes geothermal field, Iceland. *Geothermics*. 2021;97, 102223. https://doi.org/10.1016/j.geothermics.2021.102223.

59 Hüeber S, Wohlmuth B. A primal–dual active set strategy for non-linear multibody contact problems. *Comput Methods Appl Mech Eng*. 2005;194:3147–3166. https://doi.org/10.1016/j.cma.2004.08.006.

60 Nordbotten JM. Stable cell-centered finite volume discretization for Biot equations. *SIAM J Numer Anal*. 2016;54(2):942–968. https://doi.org/10.1137/15M1014280.

61 Nordbotten JM, Keilegavlen E. An introduction to multi-point flux (MPFA) and stress (MPSA) finite volume methods for thermo-poroelasticity BT - polyhedral methods in

geosciences. In: Formaggia L, Masson R, eds. *di Pietro DA*. Springer International Publishing; 2021:119–158. https://doi.org/10.1007/978-3-030-69363-3_4.
62 Parks DM. A stiffness derivative finite element technique for determination of crack tip stress intensity factors. *Int J Fract*. 1974;10(4):487–502. https://doi.org/10.1007/BF00155252.
63 Zienkiewicz OC, Zhu JZ. The superconvergent patch recovery and a posteriori error estimates. Part 1: the recovery technique. *Int J Numer Methods Eng*. 1992;33(7):1331–1364. https://doi.org/10.1002/nme.1620330702.
64 Dang-Trung H. Simulation of injection induced fracture mechanics with runscripts. https://doi.org/10.5281/zenodo.5642548.

Paper D

Modeling of mixed-mechanism stimulation for the enhancement of geothermal reservoirs

Hau Trung Dang, Eirik Keilegavlen, Inga Berre

Submitted manuscript. 2023

Modeling of mixed-mechanism stimulation for the enhancement of geothermal reservoirs

Hau Trung Dang | Eirik Keilegavlen | Inga Berre

Center for Modeling of Coupled Subsurface Dynamics, Department of Mathematics, University of Bergen

Correspondence

Hau Trung Dang, University of Bergen, Postboks 7803, 5020 Bergen, Norway

Email:

Hau.Dang@uib.no

dtrhau@gmail.com

Abstract

Hydraulic stimulation is a critical process for increasing the permeability of fractured geothermal reservoirs. This technique relies on coupled hydromechanical processes induced by reservoir stimulation through pressurized fluid injection into the rock formation. The injection of fluids causes poromechanical stress changes that can lead to the dilation of fractures due to fracture slip and to tensile fracture opening and propagation, so-called mixed-mechanism stimulation. The effective permeability of the rock is particularly enhanced when new fractures connect with pre-existing fractures. Mixed-mechanism stimulation can significantly improve the productivity of geothermal reservoirs, and the technique is especially important in reservoirs where the natural permeability of the rock is insufficient to allow for commercial flow rates.

This paper presents a modeling approach for simulating the deformation and expansion of fracture networks in porous media under the influence of anisotropic stress and fluid injection. It utilizes a coupled hydromechanical model for poroelastic, fractured media. Fractures are governed by contact mechanics and allowed to grow and connect through a fracture propagation model. To conduct numerical simulations, we employ a two-level approach, combining a finite volume method for poroelasticity with a finite element method for fracture propagation. The study investigates the impact of injection rate, matrix permeability, and stress anisotropy on stimulation outcomes. By analyzing these factors, we can better understand the behavior of fractured geothermal reservoirs under mixed-mechanism stimulation.

KEYWORDS

Mixed mechanism stimulation; Fluid injection; Fracture propagation and connection; Fault slip, Poroelasticity; Heterogeneous permeability; Two-level simulation; Contact mechanics; Open-source software.

1. Introduction

Hydraulic stimulation plays a critical role in facilitating the production of geothermal energy in low-permeability igneous rocks. Its main goal is to increase reservoir permeability to achieve flow rates that are economically feasible for commercial

production.[1–3] Hydraulic stimulation can be performed at different fluid pressures. High pressures exceeding the minimum principal stress are used to propagate hydraulic fractures, while elevated but lower pressures can cause hydro-shearing of pre-existing fractures as their frictional resistance to slip is exceeded.

In conventional hydraulic fracturing, mixtures of liquid and small insoluble particles are injected at pressures exceeding the tensile strength of the rock to increase reservoir permeability. A high-pressure injection may cause stress concentration at the fracture tip that can trigger tensile fracture propagation.[4] Propagating fractures may connect with pre-existing fractures[5] and thereby increase the fluid flow. When the hydraulic pressurization is reduced, small insoluble particles are retained in the opening of the fracture and, hence, maintain increased permeability. When applied to geothermal reservoirs, this process risks thermal short-circuiting and corresponding low temperatures of the produced fluid.[6,7]

Injections at pressures below the minimum principal stress have been shown to be an efficient mechanism for stimulating larger volumes of rock if the reservoir is characterized by pre-existing fractures and faults and high-stress anisotropy. In this case, poromechanical stress changes induced by fluid injection can cause fracture slip and corresponding shear dilation due to the sliding of rough fracture surfaces against each other. Shear dilation can strongly enhance fracture permeability.[8,9] For injections at pressures close to and above the minimum principal stress, the deformation of pre-existing fractures combines with the propagation of wing cracks toward the direction of maximum principal stress.[3,10–13] When a propagating fracture reaches another pre-existing fracture, there are no pressure concentration and low tensile stress at the tip; thus, propagation is arrested.[5] The pressure increase due to injection can then extend to the newly connected fracture, potentially causing shear slip or tensile opening and the formation of new wing cracks. As a result, the development of complex fracture networks created by connecting newly formed wing cracks to pre-existing fractures enhances the permeability of the geothermal reservoir. This mechanism of hydraulic stimulation, combining shear-dilation and propagation of fractures, is referred to as mixed-mechanism stimulation.[13–15] However, the complex dynamics of stress redistribution related to mixed-mechanism stimulation and how it interacts with pre-existing fractures are not well understood.

Numerical modeling can be employed to study the interaction between fluid flow through fractured rock and the poromechanical deformation of the rock, including fracture deformation and propagation. The complexity of the coupled processes makes it difficult to include all such effects, and thus it is common to apply simplified models that consider only a subset of the processes. For instance, modeling of tensile fracturing of poroelastic media caused by high injection pressure while neglecting the effects of shear slip, contact, and friction has been widely reported.[16–19] Several studies have further investigated the

extension of pre-existing fracture networks in porous media resulting from fluid injection. However, these studies have either neglected friction and contact mechanics at fracture interfaces[20–22] or forced fractures to propagate along predefined paths.[11,21]

Recently, the authors proposed a new methodology to simulate fluid flow, matrix deformation, fracture slip, and fracture propagation in porous media as a result of fluid injection.[10] Specifically, a mathematical model was developed based on the mixed-dimensional discrete fracture matrix (md-DFM) conceptual model that combined the explicit representation of major fractures with a continuum representation of the surrounding medium. This model utilized a co-dimension-one representation of the fractures. Hence, for a two-dimensional (2D) domain, fractures were represented as one-dimensional (1D) lines, with a longitudinal parameter representing fracture apertures. The model allowed for the application of fracture contact mechanics, including frictional sliding and shear-dilation of fractures and tensile fracture opening. The framework was designed as a two-level method, with local computation of fracture propagation around individual tips split separate from global computations of flow and poromechanical deformation of the fractured rock. The coupling strength between the local and global models was a user-controlled parameter that allowed users to balance simulation accuracy and computational cost.

This study uses the approach proposed by Hau et al.[10] to further investigate the mixed-mechanism stimulation of fractured rock under anisotropic stresses. It explores how fluid injection can change the effective poroelastic stress regime, resulting in fracture slip and dilation as well as tensile fracture propagation. The study examines how stimulation outcomes are affected by the injection rate, matrix permeability, and stress anisotropy. Specifically, the study considers fracture coalescence, which creates new, dominant flow paths.

The paper is organized as follows. Section 2 presents the mathematical model for mixed-mechanism stimulation of a fractured geothermal reservoir. In Section 3, we describe the numerical approach used to simulate the behavior of the reservoir under stimulation. Section 4 presents the results of several numerical test cases, which provide insights into the role of mixed-mechanism stimulation in enhancing reservoir permeability. Finally, in Section 5, we present our conclusions and provide remarks about the implications of our findings.

2. Mathematical model

This section presents the governing equations that model fluid flow and deformation in fractured porous media. Additionally, we introduce a mathematical model for fracture contact mechanics, propagation, and coalescence. These equations are essential for developing a simulation model that accurately captures the behavior of fractured

geothermal reservoirs under mixed-mechanism stimulation. By modeling the coupling of fluid flow, rock deformation, and fracture growth, we can better understand the impact of stimulation on the reservoir. The numerical simulations described in later sections of the paper are based on the mathematical models presented in this section.

2.1. Fluid flow and poroelastic deformation of the matrix and fracture

The md-DFM conceptual model for a 2D fractured porous media domain was employed in this paper. By using the md-DFM model, we divide the domain into three subdomains: a 2D host medium denoted by Ω^{M}, a set of fractures represented as 1D objects and denoted by Ω^{F}, and fracture intersections represented as points and denoted by Ω^{I}. The boundaries of Ω^{M} and Ω^{F} are denoted by $\partial\Omega^{\mathrm{M}}$ and $\partial\Omega^{\mathrm{F}}$, respectively, while Γ represents the interfaces between the host medium and fractures. When necessary, to denote the interfaces at the different sides of a fracture, we use superscripts $\pm$ on Γ. The interfaces between Ω^{F} and Ω^{I} are denoted by Λ, where the superscript i is used on Λ when necessary to denote the interface between Ω^{I} and a specific fracture indexed by i. Figure 1 provides an illustration of the model.

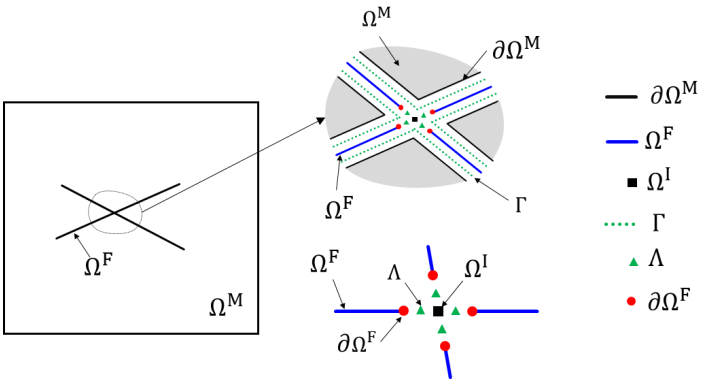

Figure 1. Illustration of a host medium Ω^{M}, fractures Ω^{F}, intersection Ω^{I}, and interfaces between higher- and lower-dimensional domains, denoted by Γ and Λ, respectively. In the detailed images to the right of the general figure on the left, the different domains and interfaces are separated for illustration purposes.

To facilitate coupling between the subdomains, projection operators $\Pi^{[-]}_{[-]}$ are introduced.[23] The illustration of these operators is given in Figure 2, where the subscripts of Π indicate the origin, while the superscripts indicate the destination of the projection.

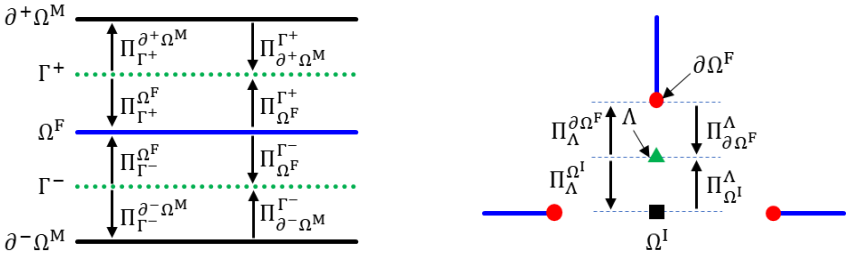

a) Projection operators between Ω^M and Ω^F b) Projection operators between Ω^F and Ω^I

Figure 2. Illustration of projection operators between subdomains.

In our model, we assume that the porous media domain is deformable and that its mechanical properties are elastic, isotropic, and homogeneous. We assume that the fluid is a single phase and slightly compressible. The permeability is allowed to be heterogeneous. The governing equations can be given as follows:

$$\nabla \cdot \boldsymbol{\sigma} = \mathbf{b}, \quad \text{on } \Omega^M \quad (1)$$

$$\boldsymbol{\sigma} = \mathbf{C}\nabla\mathbf{u} - \alpha p\mathbf{I}, \quad \text{on } \Omega^M \quad (2)$$

$$\alpha \frac{\partial(\nabla\cdot\mathbf{u})}{\partial t} + \left(\phi c_p + \frac{\alpha-\phi}{K}\right)\frac{\partial p}{\partial t} + \nabla\cdot\mathbf{q} = q^0, \quad \text{on } \Omega^M \quad (3)$$

$$\mathbf{q} = -\frac{1}{\mu}\begin{bmatrix}\kappa_{xx} & 0\\ 0 & \kappa_{yy}\end{bmatrix}\nabla p, \quad \text{on } \Omega^M \quad (4)$$

$$\frac{\partial a}{\partial t} + a c_p \frac{\partial p_F}{\partial t} + \nabla_\parallel \cdot \mathbf{q}_F - \Pi^{\Omega^F}_{\Gamma^+}\lambda^+ - \Pi^{\Omega^F}_{\Gamma^-}\lambda^- = q^0_F, \quad \text{on } \Omega^F \quad (5)$$

$$\mathbf{q}_F = -\frac{\kappa a}{\mu}\nabla_\parallel p_F, \quad \text{on } \Omega^F \quad (6)$$

$$\frac{\partial(a_I^2)}{\partial t} + a_I{}^2 c_p \frac{\partial p_I}{\partial t} - \sum_{i=1}^{N}\Pi^{\Omega^I}_{\Lambda^i}\eta_i = q^0_I, \quad \text{on } \Omega^I \quad (7)$$

where $\mathbf{u}$, $\boldsymbol{\sigma}$, p, and $\mathbf{q}$ denote displacements, stress, pore pressure, and flux on Ω^M. The source terms for the mass conservation in the subdomains for the matrix, fractures, and fracture intersections are denoted by q^0, q^0_F, and q^0_I, respectively. The flux and pressure in the fracture subdomains are denoted by $\mathbf{q}_F$ and p_F, respectively. The terms $\lambda^\pm$ are variables that represent the flux from the matrix to the fracture at each side of the fracture. The aperture of the fracture is a, and for the fracture intersection, Ω^I, the aperture, a_I, is taken to be the average of the apertures of the intersecting fractures. The term η_i is a variable that represents the flux from fracture i to Ω^I, and N is the number of intersecting fractures around

Ω^{I}. The fracture aperture is a function determined based on the residual aperture and normal displacement jump, such that:

$$a = a_0 + [\![\mathbf{u}]\!]_{\mathrm{n}}, \quad \text{on } \Omega^{\mathrm{F}} \qquad (8)$$

where a_0 denotes the residual aperture in the undeformed state, and $[\![\mathbf{u}]\!]_{\mathrm{n}}$ represents the displacement jump in the normal direction over Ω^{F}, in which the displacement jump is defined by:

$$[\![\mathbf{u}]\!] = \mathbf{u}|_{\Gamma^-} - \mathbf{u}|_{\Gamma^+}, \quad \text{on } \Omega^{\mathrm{F}} \qquad (9)$$

where Γ is the interface between Ω^{M} and Ω^{F}. The other parameters in the above equations are given in Table 1.

Table 1. The parameters used in the governing equations.

Notation	Description	Notation	Description
$\mathbf{C}$	stiffness matrix	c_p	fluid compressibility
ϕ	matrix porosity	μ	fluid viscosity
κ_{xx}, κ_{yy}	permeability of the porous matrix	N	number of intersecting fractures
ζ	inflow from the matrix to the fracture	K	bulk modulus
κ	fracture permeability	$\mathbf{b}$	body forces around Ω^{I}
$\nabla, \nabla_{\parallel}$	gradient operators	tr	trace operator

To fully represent the physical system, it is necessary to incorporate the coupling between subdomains into the mathematical model. First, the coupling between Ω^M and Ω^F is defined by:

$$\mathbf{q} \cdot \mathbf{n}|_{\partial^{\pm}\Omega^{\mathrm{M}}} = \Pi_{\Gamma^{\pm}}^{\partial^{\pm}\Omega^{\mathrm{M}}} \lambda^{\pm}, \quad \text{on } \partial\Omega^{\mathrm{M}} \qquad (10)$$

$$\lambda^{\pm} = -\frac{\kappa}{\mu}\left(\frac{\Pi_{\Omega^{\mathrm{F}}}^{\Gamma^{\pm}} p_F - \Pi_{\partial^{\pm}\Omega^{\mathrm{M}}}^{\Gamma^{\pm}} \mathrm{tr}^{\pm}\, p}{a/2}\right), \quad \text{on } \Gamma^{\pm} \qquad (11)$$

where Eq. (10) indicates the balance of flux between the matrix and fracture.
The coupling between Ω^{F} and Ω^{I} is given by:

$$\mathbf{q}_f \cdot \mathbf{n}|_{\partial\Omega_i^{\mathrm{F}}} = \Pi_{\Lambda^{\mathrm{i}}}^{\Omega^{\mathrm{F}}} \eta_i, \quad \text{on } \partial\Omega_i^{\mathrm{F}} \qquad (12)$$

$$\eta_i = -\frac{\kappa a_I}{\mu}\left(\frac{\Pi_{\Omega^{\mathrm{I}}}^{\Lambda^{\mathrm{i}}} p_I - \Pi_{\Omega^{\mathrm{F}}}^{\Lambda^{\mathrm{i}}} p_F}{a_I/2}\right). \quad \text{on } \Lambda_i \qquad (13)$$

The governing equations presented here are comprehensive, as they describe the mechanisms operating in each subdomain and consider their interactions.

2.2. Fracture contact mechanics

In the context of hydromechanical coupled processes, fractures are assumed to be in one of three states: closed and sticking (with no shear displacement), closed and slipping, or open. The interactions between the fracture surfaces are governed by fracture contact mechanics. In the following, the fracture contact mechanics model is considered independently in the normal and tangential directions. First, the normal opening of the fracture is governed by a non-penetration condition written in Karush-Kuhn-Tucker (KKT) form[24] as:

$$[\![\mathbf{u}]\!]_{\mathrm{n}} - g \geq 0, \quad f_{\mathrm{n}} \leq 0, \quad ([\![\mathbf{u}]\!]_{\mathrm{n}} - g) f_{\mathrm{n}} = 0. \qquad \text{on } \Omega^{\mathrm{F}} \qquad (14)$$

Here, f_{n} represents the contact traction in the normal direction, and g is a gap function defined by:

$$g = -\tan(\psi) \|[\![\mathbf{u}]\!]_{\tau}\|, \qquad \text{on } \Omega^{\mathrm{F}} \qquad (15)$$

where ψ is the dilation angle and $[\![\mathbf{u}]\!]_{\tau}$ is the displacement jump in the tangential direction. The gap function in Eq. (15) accounts for the dilation of the fracture resulting from tangential slip while maintaining contact between the fracture surfaces. This feature enables the enhancement of permeability in the fracture due to shear dilation.

The tangential motion of the fracture is modeled as a frictional contact problem given by:

$$\begin{aligned} &|f_{\tau}| \leq -\mu_s f_{\mathrm{n}}, \\ &|f_{\tau}| < -\mu_s f_{\mathrm{n}} \rightarrow [\![\dot{\mathbf{u}}]\!]_{\tau} = 0, \\ &|f_{\tau}| = -\mu_s f_{\mathrm{n}} \rightarrow \exists \varepsilon \in \mathbb{R},\ f_{\tau} = -\varepsilon [\![\dot{\mathbf{u}}]\!]_{\tau}, \end{aligned} \qquad \text{on } \Omega^{\mathrm{F}} \qquad (16)$$

where μ_s represents the friction coefficient and $\dot{\mathbf{u}}$ is the derivative of $\mathbf{u}$ with respect to time. The contact traction in the tangential direction, f_{τ}, contains directional information, and is therefore a vector despite the fracture being 1D.

Traction on the fracture surfaces balances the pressure in the fracture by Newton's third law and can be expressed as

$$\mathbf{f}_{+} = \left(\Pi^{\Gamma^{+}}_{\partial^{+}\Omega^{\mathrm{M}}} \boldsymbol{\sigma} + \mathbf{I}\, \alpha_f\, \Pi^{\Gamma^{+}}_{\Omega^{\mathrm{F}}} p_F\right), \qquad \text{on } \Gamma^{+} \qquad (17)$$

$$\mathbf{f}_{-} = -\left(\Pi^{\Gamma^{-}}_{\partial^{-}\Omega^{\mathrm{M}}} \boldsymbol{\sigma} + \mathbf{I}\, \alpha_f\, \Pi^{\Gamma^{-}}_{\Omega^{\mathrm{F}}} p_F\right). \qquad \text{on } \Gamma^{-} \qquad (18)$$

The tractions on $\Gamma^{\pm}$ are related to the contact traction vector $\mathbf{f} = (\boldsymbol{f}_{\tau}, \boldsymbol{f}_{n})$ by $\mathbf{f}_{\pm} = \pm\, \Pi^{\Gamma^{\pm}}_{\Omega^{\mathrm{F}}}(\mathbf{R}\mathbf{f})$, where $\mathbf{R}$ is a rotation matrix from the local (τ, n) to the global (x, y) coordinate system. Eqs. (17) and (18) indicate that the traction on the fracture surfaces is caused not only by the matrix deformation and pressure but also by pressure in the fracture.

2.3. Fracture propagation

We combine the maximum tangential stress criterion[25] and Paris's law[26] to determine the onset of fracture propagation as well as the propagation direction and length. The maximum tangential stress criterion assumes that a fracture propagates when the maximum tangential stress in the process zone around a fracture tip exceeds a critical value defined as:

$$K_{\mathrm{I}} \cos^3 \frac{\theta}{2} - \frac{3}{2} K_{\mathrm{II}} \cos \frac{\theta}{2} \sin \theta \geq K_{\mathrm{IC}}, \tag{19}$$

The direction of propagation is that of the maximum tangential stress given by:

$$\theta = 2 \tan^{-1} \left(\frac{K_{\mathrm{I}}}{4K_{\mathrm{II}}} \pm \frac{1}{4} \sqrt{\left(\frac{K_{\mathrm{I}}}{K_{\mathrm{II}}} \right)^2 + 8} \right), \tag{20}$$

$$K_{\mathrm{II}} \left(\sin \frac{\theta}{2} + 9 \sin \frac{3\theta}{2} \right) < K_{\mathrm{I}} \left(\cos \frac{\theta}{2} + 3 \cos \frac{3\theta}{2} \right), \tag{21}$$

where K_{I} and K_{II} are the stress intensity factors (SIFs). If more than one crack grows simultaneously, then the tips in the fracture with higher energy advance farther than the others, with a distribution given by the Paris-type law,[26]

$$l_{\mathrm{adv}}^{i} = l_{\max} \left(\frac{G_i}{\max(G_i)} \right)^{0.35}, \tag{22}$$

where l_{adv}^{i} and G_i are the propagation length and energy release for tip i, respectively.[27] By Eq. (22), the increment for each tip is limited by a preset value, $l_{\max}$.

A propagating fracture may reach and coalesce with another fracture in a T-type connection. This leads to the formation of a new intersection point that is added to Ω_{I} and new connections between the merged fractures and the intersection.

3. Discretization method

In this section, we describe a numerical approach for discretizing the mathematical model presented in Section 2. As the model depends on both space and time variables, both variables must be discretized. Since the mathematical model contains only the first derivative with respect to time, time discretization can be achieved using the backward Euler method. However, the model is more complex regarding spatial variations, which can be dealt with by the two-level simulation recently proposed by Hau et al.[10]

The motivation for using the two-level simulation approach is to balance computational cost and simulation accuracy. Specifically, poroelastic deformations with fracture contact mechanics, but without fracture propagation, are assumed to be quasi-static and are treated using a relatively coarse grid. In contrast, a locally refined grid around the fracture tip is needed to accurately capture the interaction between fracture propagation and local stress variations. If a fracture propagates and exceeds a certain threshold length, then the geometry

of the fracture network and the solution are updated in the coarse-level domain for the next time step. A brief description of this approach is provided below; for more information, we refer to Hau et al.[10]

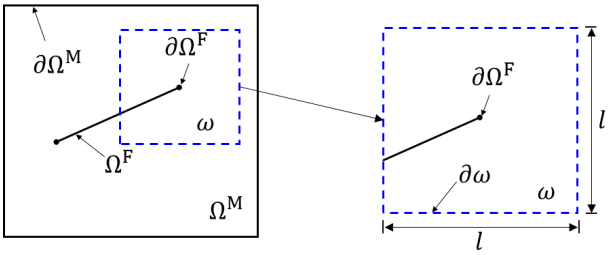

Figure 3. Illustration of a fracture, Ω^{F}, and a fine-level domain ω, adapted from Hau et al. (2022).[10]

The computational domain is divided into a coarse-level domain that matches the entire domain and smaller fine-level domains with size l that surround the fracture tips. The coarse-level and fine-level domains are denoted by Ω^{M} and ω, respectively, as illustrated in Figure 3. These domains are discretized using triangular cells with grid sizes ΔH and Δh for Ω^{M} and ω, respectively. The grids conform to the fractures so that fractures coincide with grid faces, and nodes and faces are split along the fractures. To best represent fracture paths in the grids and avoid excessive computational cost while ensuring an accurate numerical solution at the relevant scale of the model, an adaptive remeshing technique is employed.[27] This technique uses finer cells around fracture tips in both coarse-level and fine-level grids to sufficiently capture the details of fracture propagation. Additionally, to ensure the stability of the simulation, the resolution of the fine-level grid is set to be finer than that of the coarse-level grid, i.e., $\Delta h = \varepsilon_m \Delta H$ with $\varepsilon_m \leq 1$.

When none of the fine-level domains intersect with neighboring fractures, the coarse-level and fine-level domains are defined differently. However, for technical reasons, our implementation cannot handle fine-scale domains that contain multiple fractures. Therefore, when there is an intersection between a fine-level domain and neighboring fractures, the fine-level domain is defined to be identical to the coarse-level domain. Nonetheless, we emphasize that the proposed approach is still applicable for much larger domains than those demonstrated in this paper.

3.1. Two-level discretization

The poroelastic deformation model presented in subsections 2.1 and 2.2 is discretized based on the coarse-level grid. Specifically, the governing equations in subsection 2.1 are discretized using a finite volume approach with a multi-point flux approximation and a multi-point stress approximation,[28,29] while the fracture contact mechanics presented in subsection 2.2 are discretized by an active set method.[24,30,31] The solution at this level provides the deformation and fluid pressure in the poroelastic domain and determines

fracture mechanical behavior, whether the fracture is open, closed and sticking or closed and slipping.

The fine-level domain is responsible for evaluating fracture propagation at each time step. To do this, we combine Eqs. (1) and (2) and assume that the fine-level domain behaves similarly to a linearly elastic medium governed by:

$$\nabla \cdot (\mathbf{c}\nabla_s \mathbf{u}_l) + \mathbf{b} = 0, \tag{23}$$

where $\mathbf{u}_l$ is the deformation in the fine-level domain, $\mathbf{b} = -\nabla \cdot (\alpha p \mathbf{I})$ is the body force caused by pressure from the coarse-level domain, and $\mathbf{c}$ is the stiffness tensor. The boundary conditions for the fine-level problem, i.e., defined at $\partial\omega$, are set according to the coarse-level state. To solve Eq. (23), we use a combination of the $\mathcal{P}_2$ finite element method and quarter point elements to accommodate the stress singularity at the fracture tip.[32,33] The solution obtained is then used to compute stress intensity factors (SIFs) and determine whether a fracture will propagate and, if so, where and how far it will go, as described in subsection 2.3. The maximum increment of fracture is set to the fine-level grid size, i.e., $l_{\max} = \Delta h$.

3.2. Coupling between coarse-level and fine-level solutions

To establish the numerical coupling between the coarse-level and fine-level domains, it is necessary to project the displacements from the coarse-level to the fine-level domain boundaries and compress the fine-level updates to the fracture geometry in the coarse-level grid. These projections can be achieved using three mapping processes: cell center to cell center (C2C), node to node (N2N), and cell center to node (C2N).[10] Additionally, updating the coarse-level fracture path is necessary if the propagation in the fine-level domain is sufficiently significant to cause a considerable change in the coarse-level grid. To accomplish this, we denote $|\Delta\omega^{\mathrm{F}}|$ as the total propagation length in a fine-level domain. If $|\Delta\omega^{\mathrm{F}}|$ exceeds $\varepsilon_p \Delta H$, with ε_p being a propagation factor, the coarse-level fracture is extended using a linear approximation of $\Delta\omega^{\mathrm{F}}$, and the coarse-level grid is updated.

3.3. Fracture coalescence

This paper models the fracture intersection by a T-type connection. As illustrated in Figure 4 (a), when the distance between a propagating crack tip and a boundary or another fracture is less than the grid size around the tip, the two fractures are assumed to be connected. A connection point is identified by projecting the fracture tip onto the boundary, resulting in point A. Point B is then defined as the projection of point A to the opposite side of the connected fracture boundary. Finally, the tip of the propagating fracture is split at point A to create a T-type connection, as depicted in Figure 4 (b).

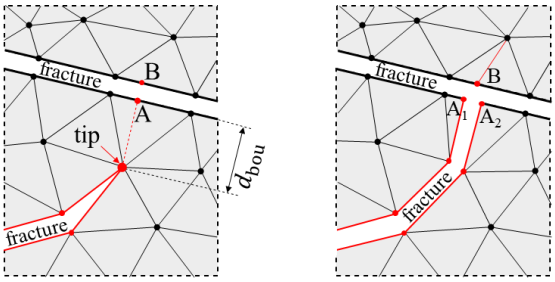

a) Determination of intersection point (A)

b) Fractures joined by a T-type connection

Figure 4. The T-type intersection between fractures or a fracture and boundary. The fracture is widened for illustration purposes.

4. Results

The accuracy of simulations of fracture propagation and fluid flow in the fractured porous media domain were verified in previous studies.[10,23,27] The numerical examples in this section aim to show the ability of the proposed model to simulate complex problems, such as multiple fractures deforming, propagating, and connecting in a medium with heterogeneous permeability.

This section presents four numerical examples to investigate the effects of the fluid injection rate, principal stress, permeability, and fracture network on mixed-mechanism stimulation for a fractured low-permeability porous medium representative of an idealized configuration in a geothermal reservoir. Given the limitation of our resources, a relatively small domain with several pre-existing fractures is considered. For all cases, the coordinates of the tips, the material, and the simulation parameters are given in Table 2, Table 3, and Table 4, respectively.

Table 2. Tips coordinates (units: m)

Tip	x	y	Tip	x	y
A	1.00	1.15	B	1.00	0.85
C	0.85	0.97	D	1.15	1.03
E	0.65	1.10	F	0.65	0.90
G	1.40	1.06	H	1.28	0.94

Table 3. Material properties

Parameter	Definition	Value
E	Young's modulus	40.0 GPa
ν	Poisson's ratio	0.2
K_{IC}	fracture toughness	$1.0\ \mathrm{MPa}\cdot\mathrm{m}^{1/2}$
α	Biot's coefficient in the matrix	0.8

ϕ	material porosity	0.01
c_p	fluid compressibility	$4.4 \times 10^{-10}\text{Pa}^{-1}$
μ	viscosity	1.0×10^{-4} Pa · s
μ_s	friction coefficient	0.5
ψ	dilation angle	1.0^{o}
a^0	initial aperture	1.0 mm

Table 4. Simulation parameters

Parameter	Definition	Value
$L_x = L_y$	coarse-level domain size	2.0 m
l	fine-level domain size	0.1 m
ΔH	coarse-level grid size	0.02 m
Δh	fine-level grid size	0.01 m
ε_{m}	ratio between coarse-grid and fine-grid sizes	0.5
ε_p	propagation factor	0.5
Δt	time step	0.5 minutes

4.1. Effect of principal stress direction

First, the effect of the principal stress on fracture propagation is investigated. As illustrated in Figure 5, we consider a 2D domain containing two intersecting fractures and the boundary conditions prescribed in this figure. We assume that the matrix permeability of the domain is isotropic and homogeneous, given by $\kappa_{xx} = \kappa_{yy} = 5.0 \times 10^{-20}$ m^2. The fractured porous medium is subject to a stress state imposed orthogonally to the domain. Fluid is injected into the vertical fracture continuously at a constant rate of $Q_0 = 1 \times 10^{-7}$ m^2/s. Two stress scenarios are considered. For case 1, $\sigma_1 = 2\sigma_2 = 20$ MPa, and for case 2, $2\sigma_1 = \sigma_2 = 20$ MPa. The propagation of the fractures, presented by solid lines, and the fluid flow, described by color, are shown in Figure 6.

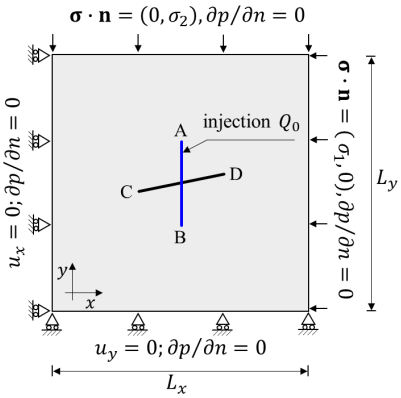

Figure 5. The geometry of model 1.

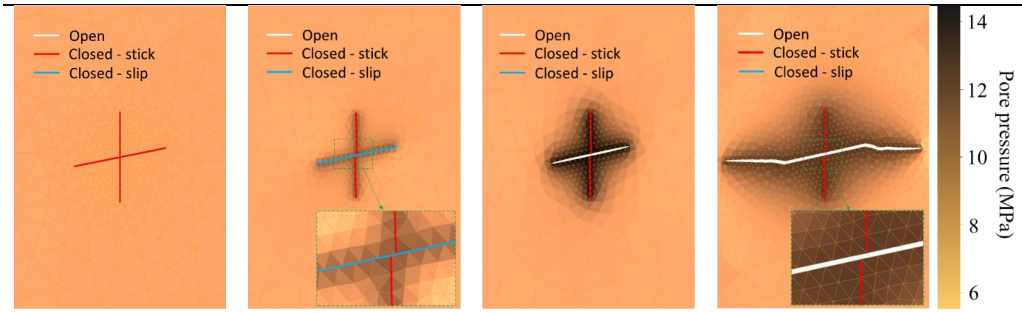

Case 1: Before injection | Case 1: After injection for 0.5 minutes | Case 1: After injection for 4.5 minutes | Case 1: After injection for 10 minutes

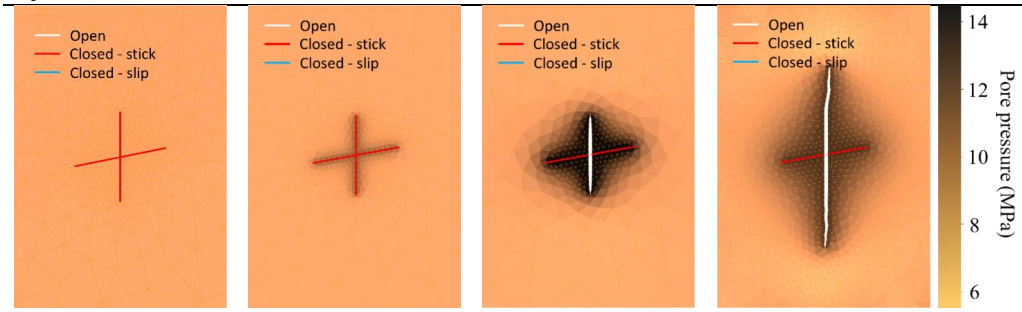

Case 2: Before injection | Case 2: After injection for 0.5 minutes | Case 2: After injection for 4.5 minutes | Case 2: After injection for 10 minutes

Figure 6. Fracture propagation and pressure evolution in a 2D porous media during fluid injection at rate $Q_0 = 1 \times 10^{-7}\, m^2/s$ into a pre-existing fracture. The solid white lines indicate opening fractures, while the solid red lines indicate closed fractures. The color bar represents pore pressure in MPa.

In both scenarios, pre-existing fractures are closed before fluid is injected due to compressive stress and friction at the fracture interfaces. Depending on the stress regime, the injection can lead to slip in pre-existing fractures. After 0.5 minutes of injection, in case 1, the fracture, which is nearly parallel to the direction of maximum stress, slips. At the same time, for case 2, both fractures remain undeformed, i.e., in the stick mode. In both cases, the vertical fracture is closed and remains in stick mode under compressive stress.
It is well known that fractures propagate toward the direction of maximum principal stress. In case 1, the low injection rate of the fluid does not provide sufficient pressure to induce tensile propagation of the vertical fracture where fluid is injected. However, it does cause shear slip and dilation of the nearly horizontal crossing fracture early in the stimulation process. Continued injection results in wing cracks that appear after 4.5 minutes and propagate in the direction of the maximum principal stress. Thus, this test case demonstrates an example of mixed-mechanism stimulation, where both shear-slip and tensile fracture propagation occur during the stimulation. In case 2, continued fluid injection combined with the shifted stress anisotropy causes the vertical fracture in which the fluid is injected to open. Shear slip does not occur in this case, and tensile propagation of the vertical fracture initiates after 7 minutes of injection once the fluid pressure has built up sufficiently. The simulation also displays the state of fractures, whether they are closed in stick mode, closed in slip mode, or open. A red line indicates a section of a fracture in stick mode, while a light-blue line indicates a section in slip mode. A section of a fracture in open mode is indicated by a solid white line.

4.2. Effect of matrix permeability

This study examines the influence of matrix permeability on fracture propagation within a 2D domain. Two distinct permeability regions are investigated, as illustrated in Figure 7. Region 1 is bounded by the curves $c_1: x - (y-1)^2 - 1.2 = 0$, $c_2: x - (y-1)^2 - 1.4 = 0$, and the right boundary, while region 2 is the remainder. The permeability in region 2 is homogeneous and isotropic with values of $\kappa_{xx} = \kappa_{yy} = 5 \times 10^{-20}\ \mathrm{m}^2$. Two simulation cases are conducted, depending on the permeability of region 1. For case 1, $\kappa_{xx} = 5 \times 10^{-20}\ \mathrm{m}^2$ and $\kappa_{yy} = 5 \times 10^{-18}\ \mathrm{m}^2$, while for case 2, $\kappa_{xx} = 5 \times 10^{-20}\ \mathrm{m}^2$ and $\kappa_{yy} = 5 \times 10^{-19}\ \mathrm{m}^2$. Additional parameters used for the simulations are $\sigma_1 = 2\sigma_2 = 20$ MPa and $Q_0 = 1 \times 10^{-7}\ \mathrm{m}^2/\mathrm{s}$. The propagation of the fractures and the fluid flow are shown in Figure 8.

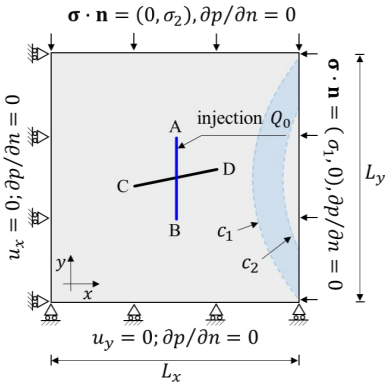

Figure 7. The geometry of model 2.

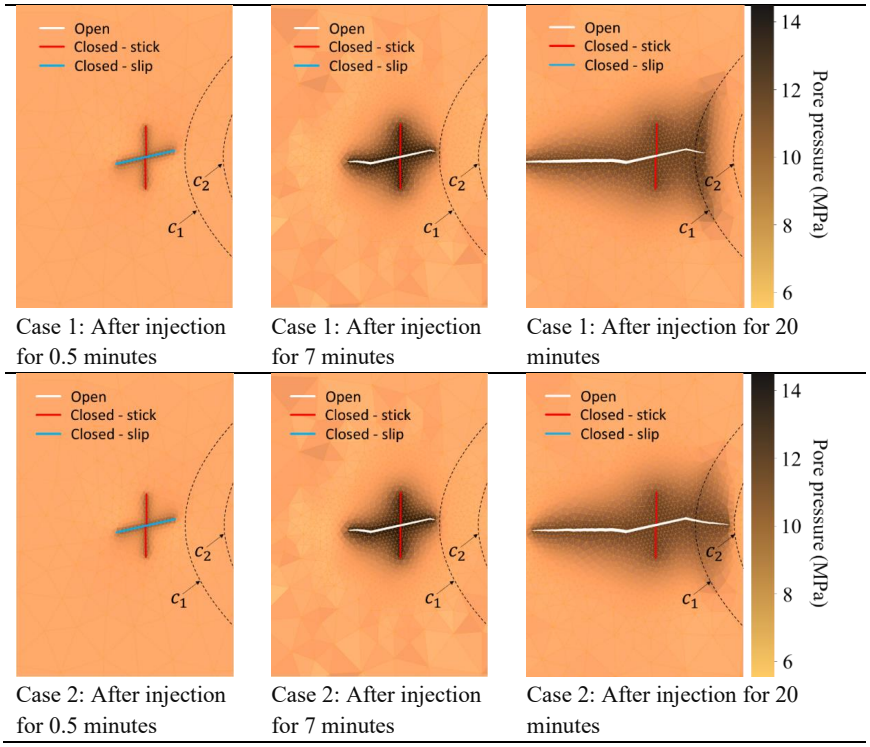

Case 1: After injection for 0.5 minutes | Case 1: After injection for 7 minutes | Case 1: After injection for 20 minutes

Case 2: After injection for 0.5 minutes | Case 2: After injection for 7 minutes | Case 2: After injection for 20 minutes

Figure 8. Fracture propagation and pressure evolution in a 2D porous medium during fluid injection, $Q_0 = 1 \times 10^{-7}\, m^2/s$, into a pre-existing fracture. The solid white lines indicate open fractures, while the solid red lines indicate closed fractures. The color bar represents pore pressure in MPa.

The presence of a highly permeable area inhibits fracture growth by preventing fluid pressure from building sufficiently due to fluid leakage into the matrix. Similar to case 1 in example 4.1, the principal stress scenario and fluid injection induce horizontal fracture slip and trigger the appearance of wing cracks after 5.5 minutes of injection. The wing cracks then propagate to opposite sides, where one makes contact with the area of higher permeability after 7 minutes. This contact causes fluid leakage and slows the fracture growth rate. Additionally, the tip in contact with the higher permeability region propagates much more slowly, while the remaining tip propagates in the direction of the maximum principal stress. In both cases studied, the fractures could not propagate through the higher permeability region. This example clearly illustrates the sensitivity of matrix permeability and demonstrates that simulation tools that do not capture this effect or represent flow in the matrix at all cannot accurately represent the propagation process.

4.3. Effect of injection rate

This example investigates the effect of the injection rate on the expansion of the stimulation area. Figure 9 illustrates a 2D fractured domain containing three fractures with boundary conditions described in the figure. We assume that the permeability is isotropic and homogeneous, given by $\kappa_{xx} = \kappa_{yy} = 5.0 \times 10^{-20}$ m^2. The principal stress is given by $\sigma_1 = 2\sigma_2 = 20$ MPa. Various injection rates are studied, and the effect on fracture growth and pressure in the fracture is shown in Figure 10.

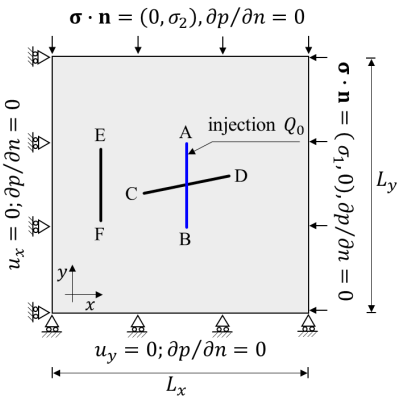

Figure 9. The geometry of model 3.

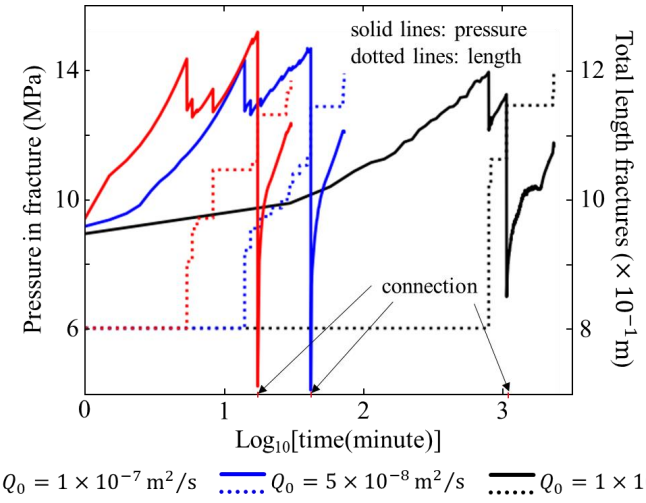

Figure 10. Effect of fluid injection rate on pressure at the injection point and total fracture growth.

The results shown in this example indicate that an increase in the injection rate leads to faster fracture propagation, and the propagation speed is nonlinearly dependent on the injection rate. As illustrated in Figure 10, wing cracks initiate after 4.5 minutes for an injection rate of $Q_0 = 1 \times 10^{-7}\ \mathrm{m}^2/\mathrm{s}$, whereas it takes up to 870 minutes for an injection rate of $Q_0 = 1 \times 10^{-8}\ \mathrm{m}^2/\mathrm{s}$. This indicates that increasing the injection rate by a factor of ten can accelerate the expansion of the fracture network by up to 200 times. However, if the injection rate is too low, then no fracture deformation may occur during our implementation.

4.4. Interaction with pre-existing fractures

Finally, we investigate the influence of the location and shape of pre-existing fractures on the expansion of the fracture network. The model geometry is shown in Figure 11. The matrix permeability in this example is assumed to be isotropic and homogeneous, i.e., $\kappa_{xx} = \kappa_{yy} = 5.0 \times 10^{-20}\ \mathrm{m}^2$. The principal stress is given by $\sigma_1 = 2\sigma_2 = 20$ MPa. The injection rate is $Q_0 = 2 \times 10^{-7}\ \mathrm{m}^2/\mathrm{s}$. The evolutions of the fracture geometry and the pore pressure are shown in Figure 13.

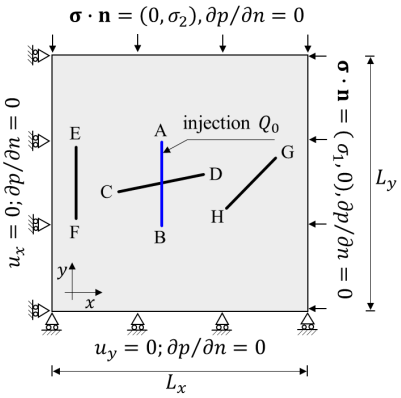

Figure 11. The geometry of model 4.

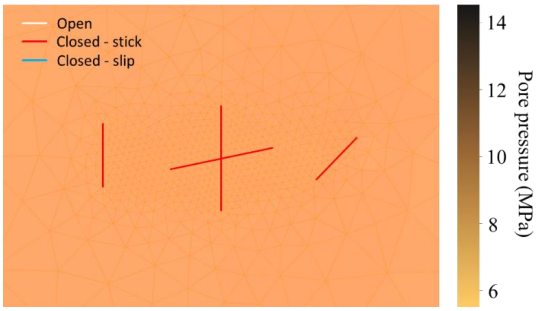

Figure 12. Fracture state and pressure in a 2D porous medium before fluid is injected.

Prior to fluid injection, the fracture mode and pore pressure are evaluated. As illustrated in Figure 12, pre-existing fractures are closed and remain in stick mode due to compressive stress and friction at the fracture interfaces. Additionally, the pressure throughout the domain is uniform at 6.8 MPa. The result in this simulation indicates a stable condition with no fracture slip or propagation.

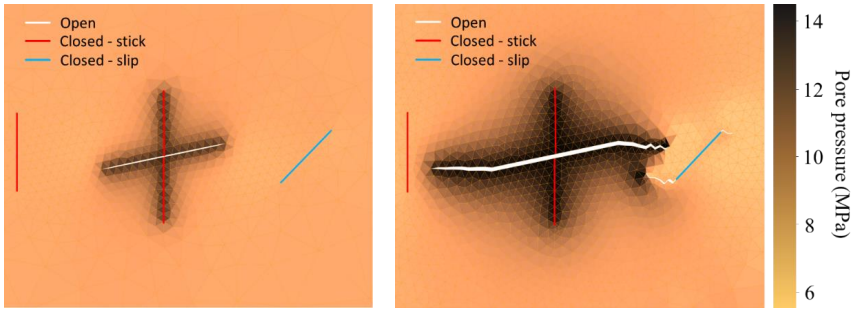

After injection for 0.5 minutes

After injection for 5 minutes

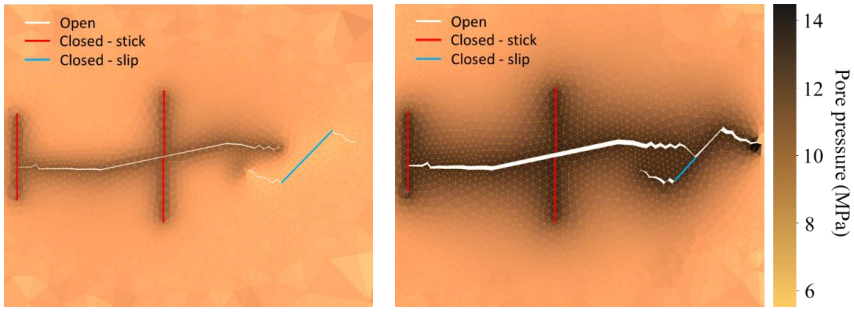

After injection for 8 minutes After injection for 20 minutes

Figure 13. Fracture propagation and pressure evolution in a 2D porous medium during fluid injection, $Q_0 = 2 \times 10^{-7}\, m^2/s$, into a pre-existing fracture. The solid white lines indicate open fractures, while the solid red lines indicate closed fractures. The color bar represents pore pressure in MPa.

Subsequently, fluid is injected into a vertical fracture, resulting in several interesting phenomena, as shown in Figure 13. First, the injection has an insignificant effect on the state of the fracture where fluid is injected, as it remains under compression under the influence of the stress regime. However, the injection facilitates the opening of the horizontal fracture connected to it and leads to the propagation of this fracture. Second, due to deformation and hydromechanical stress changes caused by fluid injection, the pre-existing fracture to the right of the domain starts to slip at an early stage of fluid injection. Eventually, small wing cracks are observed to form at the tips of this fracture. Third, there is a strong link between fracture propagation and pressure drop in the fracture. After a period of fluid injection, the pressure in the central, nearly horizontal, fracture increases sufficiently to cause tensile propagation of the fracture, which ultimately connects to the pre-existing fractures at the left and right. Each connection results in an instantaneous decrease in pore pressure, which takes time to recover through fluid injection before the fracture can resume growing. Furthermore, the expansion of the fractured network is influenced by the pre-existing fractures. During the simulation, the fracture on the right-hand side where the slip occurs continues to grow, while the fracture on the left side where compression occurs (closed in stick mode) prevents further network expansion.

5. Conclusions

This paper presents a mathematical model and numerical approach to investigate the use of mixed-mechanism stimulation to improve permeability in geothermal reservoirs. The mathematical model combines Biot poroelasticity and fracture mechanics and accounts for frictional contact mechanics and fracture propagation and connection. A two-level model that combines finite volume and finite element methods is proposed for numerical

simulations. Several numerical examples are performed, and the results indicate the following:

1) Fluid injection at elevated pressure can induce shear slip and dilation, opening, and propagation of fractures. Newly formed fractures tend to propagate in the direction of maximum principal stress. In the case of multiple connected fractures in an anisotropic stress field, the propagation of fractures depends on fracture network characteristics such as fracture orientation relative to the stress field and whether fractures are hydraulically connected to the well through other fractures.
2) A more permeable bulk domain slows fracture growth by causing fluid leakage into the matrix, making hydraulic stimulations less effective for areas with higher permeability.
3) The relationship between the injection rate and fracture growth speed is nonlinear, and injection at a low rate may not result in fracture expansion. In most cases, when the injection rate is slower, the injection time required for a fracture to propagate is significantly longer.
4) The locations of pre-existing fractures influence the expansion of a fracture network. Fractures tend to propagate in the direction of the maximum principal stress, and pre-existing fractures can facilitate or impede the development of propagating fractures.

In conclusion, this study demonstrates that mixed-mechanism stimulation can significantly improve permeability by expanding the fracture network. However, this expansion is complex and influenced by various factors, including the stress state, material permeability, injection rate, and fracture location. The simulation model proposed in this study represents an approach that is appropriate for utilization in future studies to further investigate these phenomena.

Declaration of Competing Interest

The authors declare that they have no known competing financial interests or personal relationships that could have appeared to influence the work reported in this paper.

Acknowledgments

This project received funding from the European Research Council (ERC) under the European Union's Horizon 2020 research and innovation program (grant agreement No 101002507).

References

1. Breede K, Dzebisashvili K, Liu X, Falcone G. A systematic review of enhanced (or engineered) geothermal systems: past, present and future. *Geothermal Energy*. 2013;1(1):4. doi:10.1186/2195-9706-1-4
2. Huenges E. 25 - Enhanced geothermal systems: Review and status of research and development. In: DiPippo R, ed. *Geothermal Power Generation*. Woodhead Publishing; 2016:743-761. doi:10.1016/B978-0-08-100337-4.00025-5
3. Jung R. EGS — Goodbye or Back to the Future. In: *Effective and Sustainable Hydraulic Fracturing*. InTech; 2013:95-121. doi:10.5772/56458
4. Detournay E. Mechanics of Hydraulic Fractures. *Annu Rev Fluid Mech*. 2016;48(1):311-339. doi:10.1146/annurev-fluid-010814-014736
5. Weng X. Modeling of complex hydraulic fractures in naturally fractured formation. *Journal of Unconventional Oil and Gas Resources*. 2015;9:114-135. doi:10.1016/j.juogr.2014.07.001
6. Parker Penryn Cornwall. The Rosemanowes HDR project 1983-1991. Published online 1999. doi:10.1016/S0375-6505(99)00031-0
7. Tenma N, Tsutomu Y, Zyvoloski G. The Hijiori Hot Dry Rock test site, Japan: Evaluation and optimization of heat extraction from a two-layered reservoir. *Geothermics*. 2008;37:19–52. doi:10.1016/j.geothermics.2007.11.002
8. Lee HS, Cho TF. Hydraulic Characteristics of Rough Fractures in Linear Flow under Normal and Shear Load. *Rock Mech Rock Eng*. 2002;35(4):299-318. doi:10.1007/s00603-002-0028-y
9. Guglielmi Y, Cappa F, Avouac JP, Henry P, Elsworth D. Seismicity triggered by fluid injection–induced aseismic slip. *Science (1979)*. 2015;348(6240):1224-1226. doi:10.1126/science.aab0476
10. Dang-Trung H, Berre I, Keilegavlen E. Two-level simulation of injection-induced fracture slip and wing-crack propagation in poroelastic media. *International Journal of Rock Mechanics and Mining Sciences*. 2022;160. doi:10.1016/j.ijrmms.2022.105248
11. McClure MW, Horne RN. An investigation of stimulation mechanisms in Enhanced Geothermal Systems. *International Journal of Rock Mechanics and Mining Sciences*. 2014;72:242-260. doi:10.1016/j.ijrmms.2014.07.011
12. Norbeck JH, McClure MW, Horne RN. Field observations at the Fenton Hill enhanced geothermal system test site support mixed-mechanism stimulation. *Geothermics*. 2018;74:135-149. doi:10.1016/j.geothermics.2018.03.003

13. Gischig V, Preisig G. *Hydro-Fracturing versus Hydro-Shearing: A Critical Assessment of Two Distinct Reservoir Stimulation Mechanisms*.; 2015. doi:10.13140/RG.2.1.4924.3041
14. Stefansson I, Berre I, Keilegavlen E. A fully coupled numerical model of thermo-hydro-mechanical processes and fracture contact mechanics in porous media. *Comput Methods Appl Mech Eng*. 2021;386:114122. doi:10.1016/j.cma.2021.114122
15. Jia Y, Tsang CF, Hammar A, Niemi A. Hydraulic stimulation strategies in enhanced geothermal systems (EGS): a review. *Geomechanics and Geophysics for Geo-Energy and Geo-Resources*. 2022;8(6):211. doi:10.1007/s40948-022-00516-w
16. Lecampion B, Bunger A, Zhang X. Numerical methods for hydraulic fracture propagation: A review of recent trends. *J Nat Gas Sci Eng*. 2017;49. doi:10.1016/j.jngse.2017.10.012
17. Salimzadeh S, Usui T, Paluszny A, Zimmerman RW. Finite element simulations of interactions between multiple hydraulic fractures in a poroelastic rock. *International Journal of Rock Mechanics and Mining Sciences*. 2017;99:9-20. doi:10.1016/j.ijrmms.2017.09.001
18. Santillán D, Juanes R, Cueto-Felgueroso L. Phase Field Model of Hydraulic Fracturing in Poroelastic Media: Fracture Propagation, Arrest, and Branching Under Fluid Injection and Extraction. *J Geophys Res Solid Earth*. 2018;123(3):2127-2155. doi:10.1002/2017JB014740
19. Settgast RR, Fu P, Walsh SDC, White JA, Annavarapu C, Ryerson FJ. A fully coupled method for massively parallel simulation of hydraulically driven fractures in 3-dimensions. *Int J Numer Anal Methods Geomech*. 2017;41(5):627-653. doi:10.1002/nag.2557
20. Lei Q, Gholizadeh Doonechaly N, Tsang CF. Modelling fluid injection-induced fracture activation, damage growth, seismicity occurrence and connectivity change in naturally fractured rocks. *International Journal of Rock Mechanics and Mining Sciences*. 2021;138:104598. doi:10.1016/j.ijrmms.2020.104598
21. Weng X., Kresse O., Cohen C., Wu R., Gu H. Modeling of Hydraulic-Fracture-Network Propagation in a Naturally Fractured Formation. *SPE Production & Operations*. 2011;26(04):368-380. doi:10.2118/140253-PA
22. Wang Y, Javadi AA, Fidelibus C. A hydro-mechanically-coupled XFEM model for the injection-induced evolution of multiple fractures. *Int J Numer Anal Methods Geomech*. Published online April 5, 2023:1–20. doi:10.1002/nag.3527

23. Keilegavlen E, Berge R, Fumagalli A, et al. PorePy: an open-source software for simulation of multiphysics processes in fractured porous media. *Comput Geosci*. 2021;25(1):243-265. doi:10.1007/s10596-020-10002-5
24. Hüeber S, Wohlmuth B. A primal–dual active set strategy for non-linear multibody contact problems. *Comput Methods Appl Mech Eng*. 2005;194:3147-3166. doi:10.1016/j.cma.2004.08.006
25. Erdogan F, Sih GC. On the Crack Extension in Plates Under Plane Loading and Transverse Shear. *Journal of Basic Engineering*. 1963;85(4):519-525. doi:10.1115/1.3656897
26. Paris P, Erdogan F. A Critical Analysis of Crack Propagation Laws. *J Fluids Eng*. 1963;85(4):528-533. doi:10.1115/1.3656900
27. Dang-Trung H, Keilegavlen E, Berre I. Numerical modeling of wing crack propagation accounting for fracture contact mechanics. *Int J Solids Struct*. 2020;204-205:233-247. doi:10.1016/j.ijsolstr.2020.08.017
28. Nordbotten JM. Stable Cell-Centered Finite Volume Discretization for Biot Equations. *SIAM J Numer Anal*. 2016;54(2):942-968. doi:10.1137/15M1014280
29. Nordbotten JM, Boon WM, Fumagalli A, Keilegavlen E. Unified approach to discretization of flow in fractured porous media. *Comput Geosci*. 2019;23(2):225-237. doi:10.1007/s10596-018-9778-9
30. Hintermüller M, Ito K, Kunisch K. The Primal-Dual Active Set Strategy as a Semismooth Newton Method. *SIAM Journal on Optimization*. 2002;13:865-888. doi:10.1137/S1052623401383558
31. Wohlmuth B. Variationally consistent discretization schemes and numerical algorithms for contact problems. *Acta Numerica*. Published online 2011. doi:10.1017/S0962492911000079
32. Parks DM. A stiffness derivative finite element technique for determination of crack tip stress intensity factors. *Int J Fract*. 1974;10(4):487-502. doi:10.1007/BF00155252
33. Barsoum RS. Triangular quarter-point elements as elastic and perfectly-plastic crack tip elements. *Int J Numer Methods Eng*. 1977;11(1):85-98. doi:10.1002/nme.1620110109

Graphic design: Communication Division, UiB / Print: Skipnes Kommunikasjon AS

uib.no

ISBN: 9788230856147 (print)
9788230850947 (PDF)